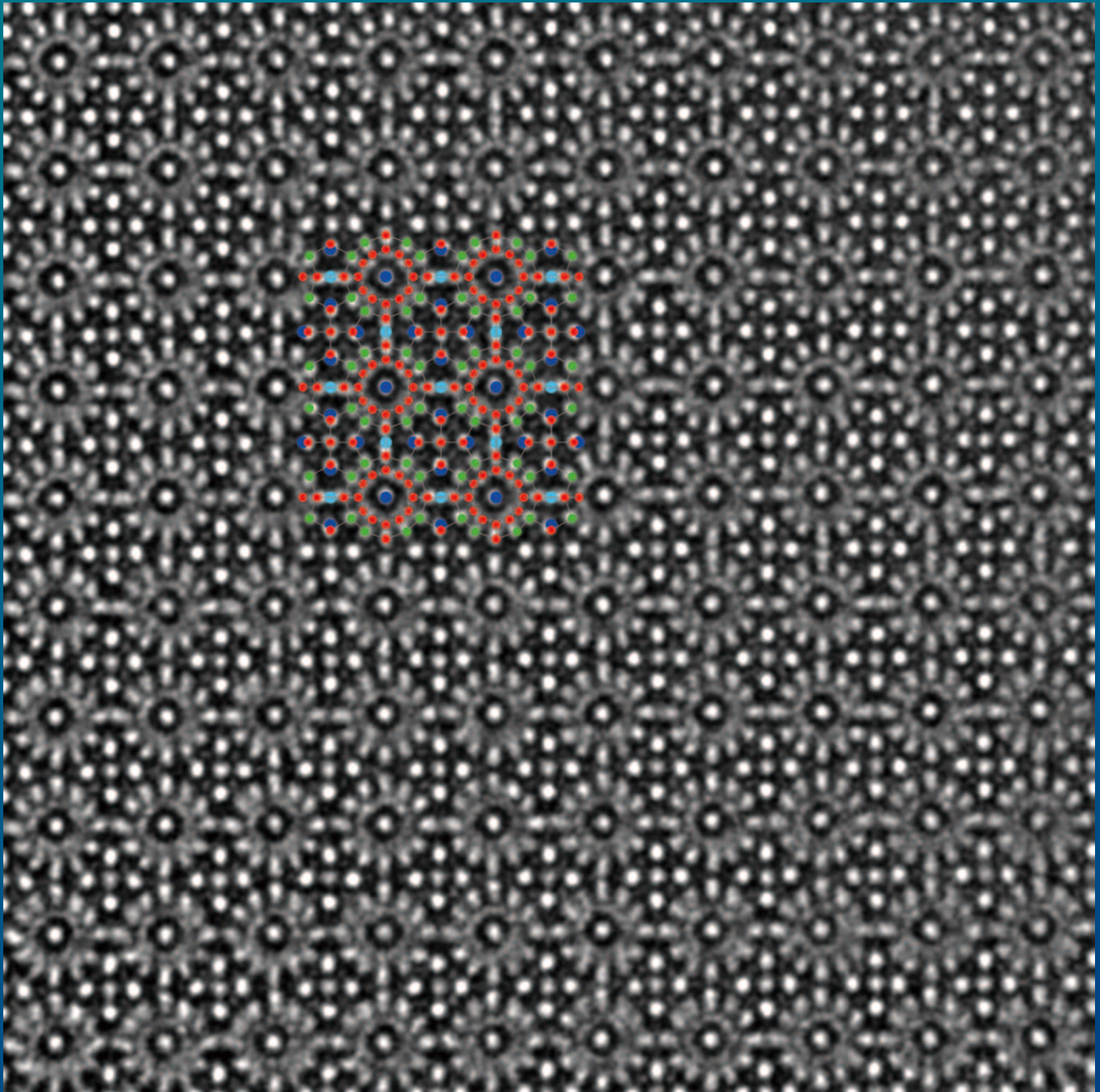
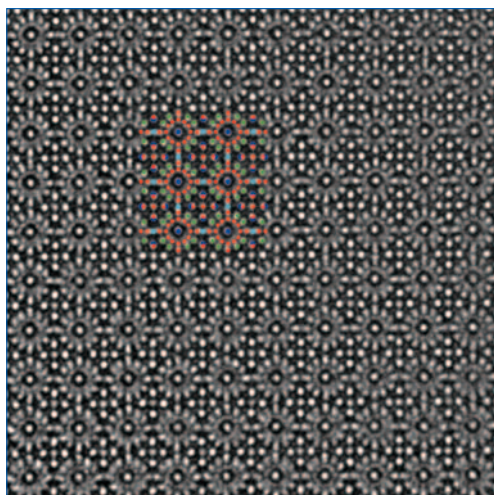


JEOL NEWS

July 2016
Vol.51
No.1



- Atomic Resolution Microscopy of Intermetallic Clathrates2
Reiner Ramlau, Juri Grin and Hidetaka Sawada
- Probing the Atomic-Scale Structure of Electrode Materials for Rechargeable Batteries
by Aberration-Corrected Scanning Transmission Electron Microscopy7
Qinghua Zhang, Lin Gu
- Microscopic Analyses of Deformation Structures around Fatigue Crack Tips16
Yoshimasa Takahashi
- Rapid Screening and Quantification of Synthetic Cannabinoids with DART-MS
and NMR Spectroscopy23
Michael A. Marino, Robert B. Cody, A. John Dane, Ling Huang
- Nanostructured Surface Phonon Polariton Systems for Mid-Infrared Nanophotonics31
Alexander J. Giles, Richard Kasica, Joshua D. Caldwell
- Visualization of Invisible Defects in Semiconductor Devices35
Kyoichiro Asayama
- Development of Cryo-Coil MAS Probe for Multinuclear Measurement42
Takashi Mizuno
- Development of JEM-F200(F2) Multi-Purpose Electron Microscope49
Kazuya Yamazaki
- Three-Dimensional Reconstruction of Biological Tissues by Serial Block Face-SEM57
Yuuki Yamaguchi, Tomohiro Haruta, Akira Mizoguchi, Hideo Nishioka
- Depth Profile Measurement with JPS-903063
Masahide Shima



Cover micrograph

Aberration-corrected TEM image of $K_7B_7Si_{39}$ in [100] orientation taken with a JEM-ARM300F and its atomic structure model overlaid on the image. (See Fig. 3 in page 4 and Fig. 6(a) in page 5)

Atomic Resolution Microscopy of Intermetallic Clathrates

Reiner Ramlau¹, Juri Grin¹ and Hidetaka Sawada²

¹ Max-Planck Institute for Chemical Physics of Solids

² JEOL (U.K.) LTD.

Aberration-corrected STEM and TEM with the recently installed double-corrected Grand ARM opens new horizons for the Department Chemical Metal Science at the MPI CPfS. A great number of intermetallic compounds, which exhibit both highest structural complexity and beauty, are waiting to be investigated. Long lasting problems should be finally solved. The intermetallic clathrates are prime examples for the need of the highest possible resolution. First results are presented for a potassium borosilicide with clathrate-I structure.

The instrument

The JEM-ARM300F by JEOL – nick-named the “Grand ARM” – was inaugurated at the Max-Planck Institute for Chemical Physics of Solids (CPfS) in November 2014. It was the second of a new series, the first outside Japan, and the first with double-correction. The spherical aberration C_s of both the condenser and the objective lens are annihilated by insertion of sophisticated electron-optical dodecapole correctors into the beam and image forming systems, respectively. This results in the highest lateral resolution possible in both Scanning Transmission Electron Microscopy (STEM) and Transmission Electron Microscopy (TEM). Operated at 300 kV, the STEM resolution is around 50 pm, the TEM resolution is between 50 and 70 pm (depending on the resolution criterion applied). The values at 80 kV are similarly impressive: 90 pm in (DF-)STEM; between 80 and 100 pm in TEM. Fortunately, the large majority of compounds synthesized in the Department Chemical Metal Science are less prone to beam damage at high acceleration voltage (300 kV) and their investigation can benefit of the highest achievable resolution. There is, however, a minority of substances, like compounds of light-weight elements (B, C), for which the higher stability at 80 kV must – under circumstances – be traded off by a partial loss of resolution.

The research concept of the Department Chemical Metal Science at the MPI CPfS comprises preparation of new classes of intermetallic compounds, elaboration of an enhanced understanding of the relationship between the atomic interactions, the organization of crystal structures, and their influence on the chemical and physical behaviors of these substances, as well as the development of experimental and theoretical techniques necessary for such investigations. In accordance with this concept the Grand ARM is also a veritable

chemical lab confined to one single instrument. Energy Dispersive X-ray Spectroscopy (EDXS) and Electron Energy-Loss Spectroscopy (EELS) allow the chemical analysis of nanovolumes, or even to determine the chemical nature of single atoms.

Facing the necessity to operate the Grand ARM in an urban environment, on the institute campus and in the surroundings of a vivid university, a new lab building had to be created. It fulfills the highest installation requirements with comparable low costs and, therefore, has become a reference lab on the national scale. In close cooperation with leading German and Suisse engineering companies solutions were found for extreme stabilization of the lab temperature, for isolation of the Grand ARM against all vibrations as well as for shielding and compensation of external magnetic AC and DC fields (**Fig. 1**).

The clathrates

The versatile family of clathrate structures has been meticulously classified by various authors applying different schemes (*e.g.* [1, 2]). One of their important sub-branches is the clathrate-I structure type (*cP*54). Like other clathrate types it is referred to as a “host-guest” structure. A framework of 46 tetrahedrally coordinated host atoms per unit cell forms two kinds of cage, 20-membered (dodecahedral) and 24-membered (tetrakaidecahedral) ones (*cf.* **Fig. 2**). These closely packed host cages are occupied by the guest atoms. Guest atoms may be chemically excavated *à posteriori* and a metastable clathrate remains. Under fortunate circumstances a new elemental polymorph can thus be prepared – as it was demonstrated for clathrate-II germanium (Ge *cF*136) and clathrate-I germanium (Ge *cP*46) [3, 4].

Many of the clathrates-I – often with silicon or germanium

being the main constituent of the host framework – are candidates for thermoelectric applications [5-7]. Others like $\text{Na}_{5.5}(\text{H}_2)_{2.15}\text{Si}_{46}$ and $\text{K}_{8-x}(\text{H}_2)_y\text{Si}_{46}$ are reported to encapsulate H_2 molecules as a guest species and are, therefore, discussed as materials for hydrogen storage [8, 9].

$\text{K}_7\text{B}_7\text{Si}_{39}$ was the first borosilicide to be synthesized [10]. It follows the Zintl-Klemm concept with its electronic balance being $[\text{K}^+]_7[\text{B}^-]_7[\text{Si}^0]_{39}$. Together with the related quaternary borosilicide $\text{K}_3\text{Rb}_4\text{B}_7\text{Si}_{39}$ [11], they are the only clathrates known with boron as host atoms. Substituting silicon by boron results in a considerable contraction of the lattice parameter compared with the corresponding binary silicide $\text{K}_{8-x}\text{Si}_{46}$ ($x < 1$) [12]. This contraction might favor smaller guest ions to be embedded into the cages which are formed by the host framework. Therefore, silicon clathrates with boron in the host framework provide opportunities for the synthesis of narrow band gap semiconductors and are promising materials for thermoelectric applications. According to X-ray investigations [10], the compound crystallizes in space group $Pm\bar{3}n$ (No. 223) with $a = 0.9952$ nm. All of the large cages are occupied by potassium ($6d$ site) but only half of the smaller cages ($2a$ site). On the other hand, silicon and boron share the $16i$ site of the host lattice statistically in a 9:7 ratio. Ordering of potassium at $2a$ and of boron at $16i$ could be neither proven nor excluded by X-ray investigation. They are, therefore, still in the focus of scientific interest.

Of course, the two substructures (guest and host atoms) do not exist independently of each other. The occupation of host sites by boron changes the size of the cages involved and leads to consequences for the occupation of guest sites. Furthermore, a guest atom may be displaced from the cage center. All this holds for both ordered and disordered arrangements. The term “ordered” is used here to denote long-range order, whereas “disordered” effectively still includes some short-range order between the host and guest substructures. For the quaternary $\text{K}_3\text{Rb}_4\text{B}_7\text{Si}_{39}$ [11], the situation becomes even more complicated.

Two differently sized guest species, Rb and K, are distributed to two kinds of cage, larger and smaller ones. It is assumed, that the Rb occupies exclusively the large (tetrakaidecahedral) cage, whereas the K may occupy both the small (dodecahedral) and the large cage. The borosilicides descriptively illustrate one of the burning issues in Chemical Metal Science: to understand local deviations from the ideal crystal structure, including variations of the local symmetry, and their realization by chemical bonding.

Since the $\text{K}_7\text{B}_7\text{Si}_{39}$ compound exhibits lateral Si–Si and Si–K interspaces down to 47 pm and 43 pm when projected along prominent zone axes [100] and [111], respectively (**Fig. 3**), it is a striking example for the need of aberration-corrected STEM and TEM. Even with the most powerful instruments it remains a challenge to investigate the possible ordering phenomena of the two species, potassium and boron. $\text{K}_7\text{B}_7\text{Si}_{39}$ can also provide very suitable specimens for testing resolution. Compared with other clathrates, it was found to be rather stable against beam damage, although too intense and too long irradiation is suspected to remove the boron and potassium from the crystals.

Experimental

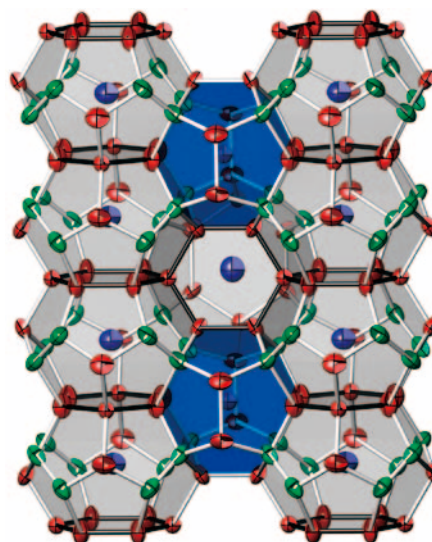
The micro-crystalline samples were further ground in an agate mortar, dispersed in *n*-butanol and spread over a holey carbon film. The Dresden “Grand ARM”, the double-corrected JEM-ARM300F described above was used for aberration-corrected TEM and STEM at 300 kV. TEM images were recorded onto a 4kx4k pixel CCD array (Gatan US4000); STEM images were taken with HAADF detection. Contamination could be completely avoided by scrupulous cleanliness. Image simulations in **Figs. 4** and **8** for the hypothetical structures were performed using the multi-slice formalism of the EMS program-package ($C_s = +20$ μm , focus-spread parameter: 5 nm, semi-angle of convergence: 0.2 mrad). All of the micrographs presented here are raw data slightly band-pass filtered.

Fig. 1



The JEM-ARM300F with double C_s -correction by JEOL – nick-named the “Grand ARM” – in its shielded and air-conditioned booth. This particular booth is placed inside the hall of a new lab building on a non-vibrating fundament.

Fig. 2



Crystal structure of $\text{K}_7\text{B}_7\text{Si}_{39}$ viewed in [100] direction. For the sake of clarity, splitting of positions ($16i$, $24k$) is not shown. Green: (Si + B) at $16i$, red: Si at $24k$ and $6c$, blue: K at $2a$ and $6d$. Pentagon-dodecahedra are shown in blue, tetrakaidecahedra in grey. (From Jung *et al.* [10]. Complete atomic coordinates and displacement factors are given there.) Compare the projected structures in Fig. 3!

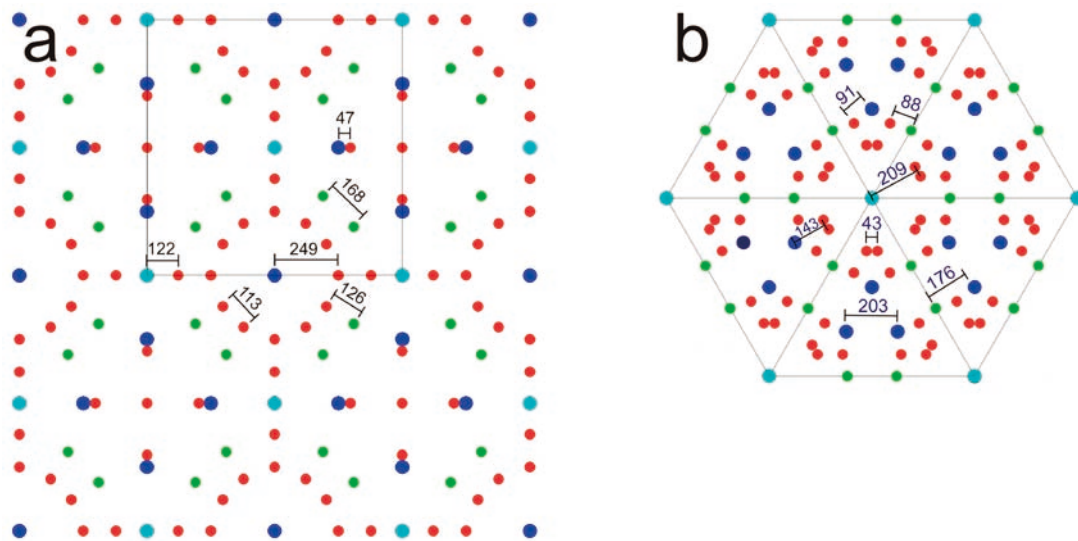
Results and Discussion

To evaluate the possibilities of aberration-corrected TEM, images were simulated (Fig. 4) for the ternary borosilicide $K_7B_7Si_{39}$ and some binary hypothetical structures: For a) K_6Si_{46} the occupancy of the $2a$ site is zero (no potassium in the dodecahedral cages) and for c) K_8Si_{46} the $2a$ is fully occupied. b) K_7Si_{46} represents an intermediate situation; the occupancy of the $2a$ site is 0.5. This approximates the compound $K_7B_7Si_{39}$ best – with respect to the K guest atoms. Half of the dodecahedral cages are occupied statistically. With a corrected TEM (assumed resolution: 0.1 nm) small contrast variations appear at the $2a$ site (red arrows in Fig. 4). By comparison of the under-focus TEM image in Fig. 5 with Fig. 4 the different K occupancies of the $2a$ sites are immediately recognized. Some of the $2a$ sites, which are situated horizontally and vertically between the rosette-like features, are indicated by red arrows. One has to consider that all images are projections. In the $[100]$ viewing direction, there is one $2a$ site per unit cell (1 nm). With an assumed specimen

thickness of 3 nm, three $2a$ sites with different occupancies are projected onto one another, resulting in an effective occupancy of 0, 1, 2, or 3 for the whole column. The perfect projection onto one another may be broken by displacement of the K atom from the $2a$ in dependence on the occupation of its cubic $16i$ environment. (See Fig. 2 and look for the blue (dodecahedral) cages! The blue K atom at $2a$ in the center is surrounded by a cube of green B/Si atoms at $16i$.) The different occupancies of the $2a$ site are even more convincingly displayed by the over-focus TEM image in Fig. 6 and the HAADF-STEM image in Fig. 7a. The experimental TEM and STEM results presented here show a disordered arrangement of K at the $2a$ site. Earlier TEM investigations [13], however, revealed the existence of very small ordered domains connected with a local symmetry descent. These seemingly contradictory findings highlight an inherent difficulty of ultra-high resolution TEM and STEM to prospect in large specimen areas.

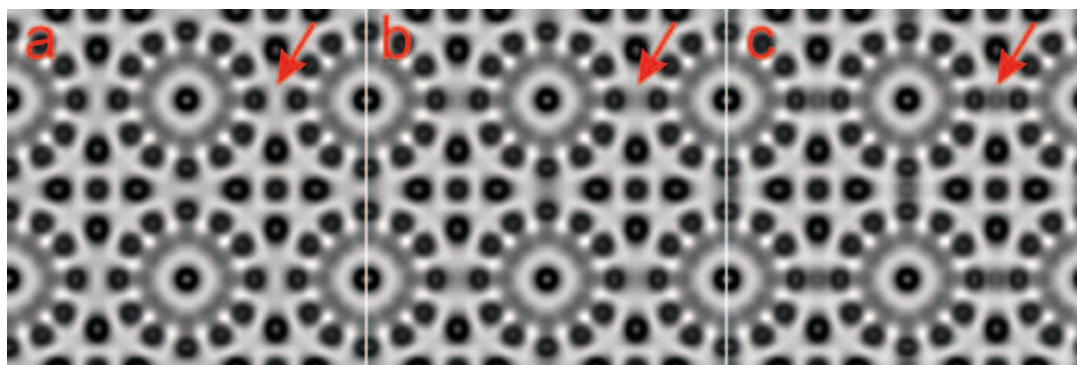
With respect to the ordering of B atoms at the $16i$ site, with 2 atoms per unit cell (1 nm) in the columns, the $[100]$ TEM

Fig. 3



Projected structure of $K_7B_7Si_{39}$ a) in $[100]$ and b) in $[111]$ direction. Unit cell and some Si–Si, Si–Si/B, and Si–K interspaces are indicated in pm. Green: (Si + B) at $16i$; red: Si at $24k$ and $6c$; light-blue: K at $2a$ (center of the small, dodecahedral cage) and dark-blue K at $6d$ (center of the large, tetrakaidekahedral cage).

Fig. 4



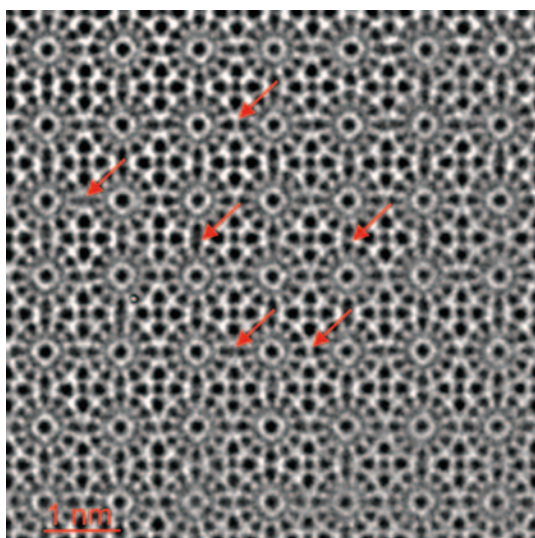
Simulated TEM images for the hypothetical structures a) K_6Si_{46} , b) K_7Si_{46} and c) K_8Si_{46} in $[100]$ orientation for an aberration-corrected TEM at optimum focus and for $t = 5$ nm. ($C_s = 20 \mu\text{m}$, $\Delta = 5$ nm, $\alpha/2 = 0.2$ mrad, $\Delta f = -8$ nm). Note the contrast variations at the $2a$ site (red arrows)!

images provide no evidence of boron atoms at all. Figure 8 compares simulated images for a) $K_7B_7Si_{39}$ and the hypothetical structure b) K_8Si_{46} . The expected contrast differences are very small; they would be enhanced in case of any ordering. On the other hand, by HAADF-STEM (Fig. 7b) the presence of boron, *i.e.* the lack of silicon, at the respective sites could be imaged directly. Distinct contrast variations (marked in Fig. 7b) can be noticed between different 16*i* sites (shared by B and Si) as well as between some of the 16*i* sites and the 24*k* sites (always occupied by Si) along the outer ring of the “rosettes” (green and red, respectively, in Fig. 3a). The simulated HAADF-STEM

image in Fig. 7c is based on statistical occupancies for K at 2*a* and B at 16*i*. Consequently, contrast differences between the 16*i* and 24*k* sites may, once again, hardly be realized.

The HAADF-STEM image (Fig. 7b) is furthermore remarkable because the 12 sites forming the inner ring of the “rosettes” are clearly resolved. This could not always be achieved. Considering the (projected) inter-atomic distance of 113 pm (*cf.* Fig. 3a), which is by far within the resolution power of the microscope, defective tetrakaidecahedra (by nature or by beam damage) have to be taken into account. Figure 7b highlights Si-K “pairs” with the (projected) inter-atomic distance of 47 pm. The respective columns contain one K atom and two Si atoms per unit cell (1 nm). Although the pairs remain generally unresolved, the shape of the spots indicates the presence of two atoms.

Fig. 5



Aberration-corrected TEM image of $K_7B_7Si_{39}$ in [100] orientation. The underfocus regime displays atoms as black. The 2*a* sites, with their statistical 50% potassium occupancy, are situated horizontally and vertically between the rosette-like features. Red arrows indicate some of the many sites where the different occupancies of the sites (more correctly of the respective columns) can be detected immediately. Compare with the simulated images shown in Fig. 4!

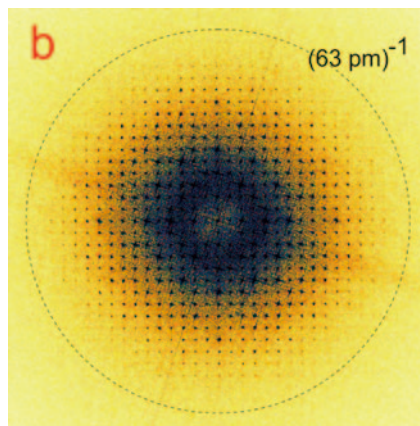
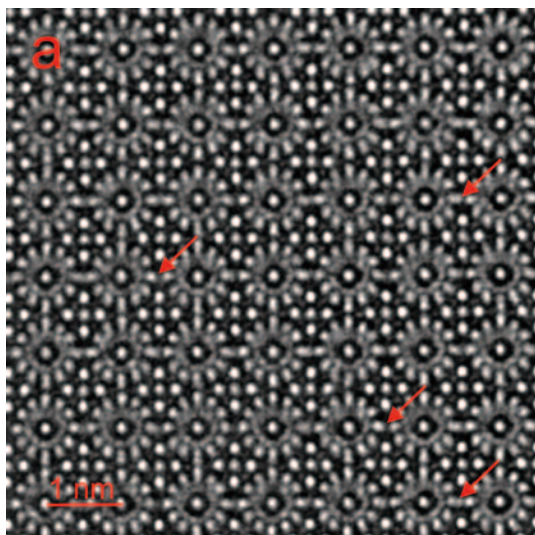
Conclusion and Outlook

Some of problems connected with the order and disorder of host and guest atoms in borosilicides with clathrate-I structure could already be solved. A more deepened understanding of inter-relations between host and guest substructures was achieved. Findings can be applied to other clathrates under investigation, *e.g.* with three different species, including vacancies, occupying the host framework. In addition to STEM and TEM exploiting the full resolution power of the Grand ARM, next experimental steps will include spectrum imaging with atomic resolution.

Acknowledgments

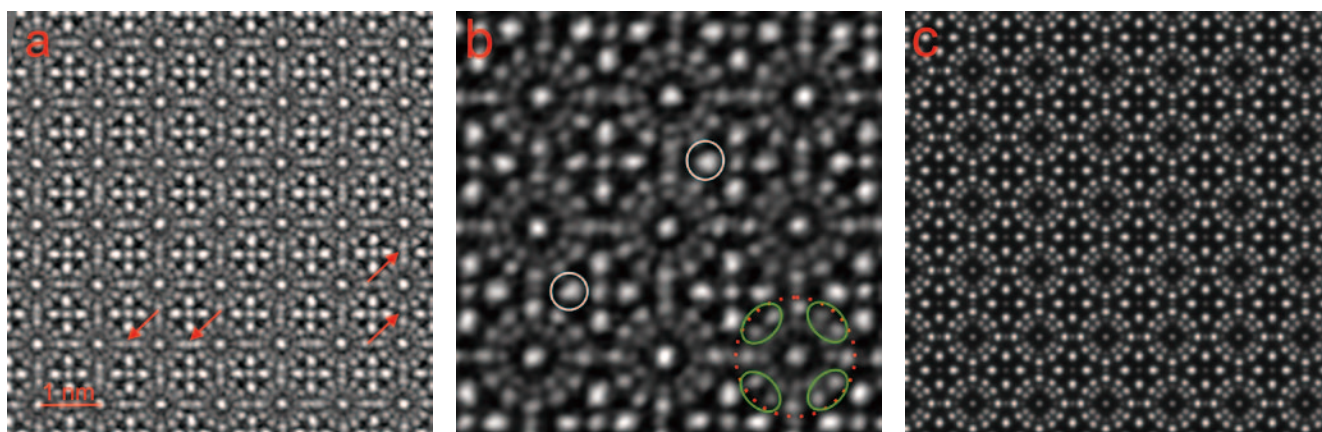
Professor Dr. Walter Jung (University of Cologne and MPI CPfS, Dresden) is gratefully acknowledged for the preparation of the investigated borosilicides, Uta Köhler (MPI CPfS) for technical assistance in operating the lab and microscope, Dr. Michael Baitinger and Dr. Bodo Böhme (both MPI CPfS) for valuable discussions. Thanks to Fumio Hosokawa (BioNet Ltd., and Tokyo Institute of Technology) for simulating the HAADF-STEM image of Fig. 7(c).

Fig. 6



a) Aberration-corrected TEM image of $K_7B_7Si_{39}$ in [100] orientation. Same region as in Fig. 5! The image, now in overfocus, displays atoms as white. Red arrows indicate where the 2*a* sites (columns) are effectively unoccupied or occupied completely.
b) The specimen is very thin and the Fourier transform extends to $(63 \text{ pm})^{-1}$.

Fig. 7

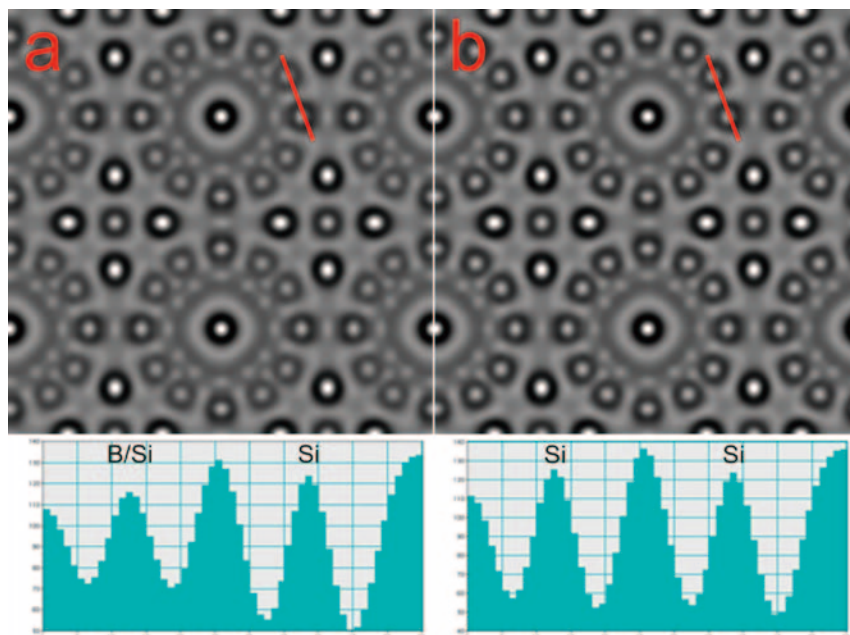


a) Aberration-corrected STEM image (HAADF) of $K_7B_7Si_{39}$ in [100] orientation. The different potassium occupancies of the $2a$ sites (columns) are revealed better than in TEM imaging. Again, red arrows indicate some exemplary situations.

b) Enlarged HAADF-STEM image. White circles highlight Si-K "pairs" with the (projected) inter-atomic distance of 47 pm. Unfortunately, this distance is just beyond the resolution power of the microscope. The elongated triangular shape of the spots is, however, indicative of the presence of two atoms. Along the outer ring of the rosette-like features (marked red dotted) Si at $24k$ and B/Si at $16i$ are alternating. Compare the projected crystal structure in Fig.3a! Pairs of $16i$ sites are marked in green. The different occupancies of the $16i$ by Si, and thus by boron, can be seen clearly. Contrast differences are obviously higher, than expected for TEM imaging. (Compare the simulated images in Fig. 8.)

c) Simulated HAADF-STEM image for $K_7B_7Si_{39}$ in [100] orientation. Specimen thickness $t = 10$ nm, slice thickness $\Delta t = 0.5$ nm, CL aperture of 30 mrad (half angle), scanning pixels: 100×100 .

Fig. 8



Simulated TEM images for a) the compound $K_7B_7Si_{39}$ and b) the hypothetical structure K_7Si_{46} in [100] orientation for an aberration-corrected TEM at optimum focus and for a specimen thickness of $t = 5$ nm ($C_s = 20 \mu\text{m}$, $\Delta = 5$ nm, $\alpha/2 = 0.2$ mrad, $\Delta f = -4$ nm). The lower row shows intensity profiles over the $16i$ site (the positions of B atoms) along the red lines.

References

- [1] K. A. Kovnir and A. V. Shevelkov, *Russ. Chem. Rev.* **73** (2004) 923.
- [2] G. S. Nolas, (Ed.): "The Physics and Chemistry of Inorganic Clathrates", Springer, Dordrecht, 2014.
- [3] A. M. Guloy et al., *Nature* **443** (2006) 320.
- [4] B. Böhme: "Neue Präparationswege für intermetallische Verbindungen", Thesis, Technical University Dresden, 2010 (Logos, Berlin, 2010).
- [5] G. S. Nolas et al., *Appl. Phys. Lett.* **73** (1998), 178.
- [6] J. L. Cohn et al., *Phys. Rev. Lett.* **82** (1999) 779.
- [7] M. Christensen, S. Johnsen, B. B. Iversen, *Dalton Trans.* **39** (2010) 978.
- [8] D. Neiner et al., *J. Am. Chem. Soc.* **129** (2007) 13857.
- [9] D. Neiner et al., *Inorg. Chem.* **49** (2010) 815.
- [10] W. Jung et al., *Angew. Chem. Int. Ed.* **46** (2007) 6725.
- [11] W. Jung, Y. Grin, M. Baitinger, 6th Intern. Conf. Inorg. Materials, Dresden 2008, P2-70.
- [12] B. Böhme et al., *J. Am. Chem. Soc.* **129** (2007) 5348.
- [13] R. Ramlau and E. Yücelen, 17th Intern. Microsc. Congr., Ro de Janeiro 2010, M21.26.

Probing the Atomic-Scale Structure of Electrode Materials for Rechargeable Batteries by Aberration-Corrected Scanning Transmission Electron Microscopy

Qinghua Zhang, Lin Gu

Institute of Physics, Chinese Academy of Sciences/Beijing National Laboratory for Condensed Matter Physics

The performance of electron microscopes has undergone a dramatic improvement both in structural and chemical resolution, benefiting from well-designed aberration correctors combined with the optimized detection geometry, especially the introduction of annular-bright-field (ABF) detectors. It is now possible to simultaneously probe heavy and light atoms (e.g. Li ions) in many energy materials and to determine atomic and electronic structure. Lithium-ion batteries (LIBs) are extremely attractive candidates for application in portable electronics, electric vehicles and smart grid, etc. Since their operation depends on the insertion and de-insertion processes of lithium, direct observation of Li is vital to understand the microscopic reaction mechanism. This paper presents a brief overview of our works on revealing the atomic-scale structure of selected electrode materials with different charge and/or discharge state, e.g., the lattice distortion, phase interface structure, transition metal migration, to extend the current understanding of electrochemical reaction mechanism by aberration-corrected scanning transmission electron microscopy (STEM). These atomic-scale investigations demonstrate the indispensable role of advanced STEM imaging and analytical techniques in exploring the relationship between atomic-level structure evolution and microscopic reaction mechanisms in electrode materials.

Introduction

Batteries have extensive applications in human activities. Especially in recent 20 years, lithium-ion batteries (LIBs) with high-output voltages and high-energy densities have flood our lives in various fields, for example, portable electronics, electronic vehicles and even grid storage applications [1, 2]. There is a recognition that inexpensive battery systems can offer a number of high-value opportunities and facilitate economic development enormously [3]. However, several critical issues, such as low power density, short cycling life, and especially safety hazards, hinder the utility of current LIBs for large-scale applications. Thus, electrochemical reaction mechanism of these rechargeable battery systems urgently needs to be explored in depth.

Each battery is composed of an anode and a cathode (separated by an electrolyte), where the reversible shuttling of lithium ions between anode and cathode across the electrolyte takes place, coupled with injection/removal of electrons. Ideally, we expect

the insertion and deinsertion of lithium would not break the host structure. In practice, however, operations of discharge and charge cycles often cause structural changes of electrode materials [4], for example, lattice expansion or contraction, migration of transition metal (TM) ions, Jahn–Teller distortion, phase transition, and surface reconstruction. Such structural changes often occur locally at atomic scale and impose significant influence on lithium diffusion, electron transport, and structural integrity of electrodes at mesoscopic and macroscopic levels, which to a great extent determine the performance and lifetime of LIBs. Therefore, atomic-scale knowledge of structural changes of electrode materials associated with lithium insertion and extraction is essential to enable in-depth understanding of energy storage mechanism. It would be also very helpful for developing new materials and improving existing battery performances.

To reveal the atomic details about electrochemical reaction mechanism of the LIBs, transmission electron microscope (TEM) may be the most suitable tool due to its structural imaging and

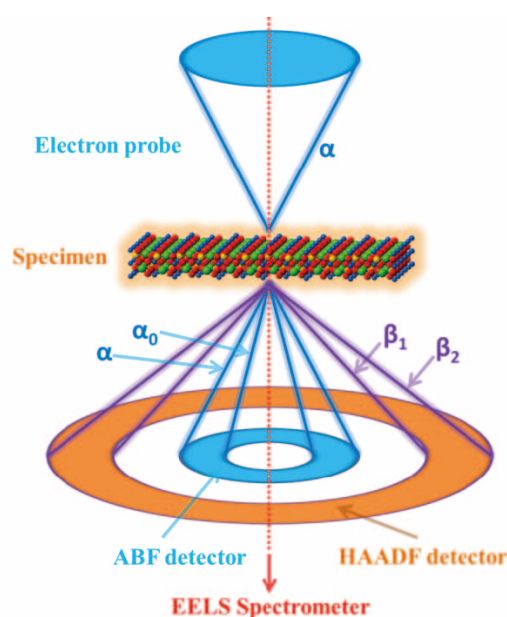
chemically analytical capability with the unprecedented spatial resolution. The intrinsic aberrations of magnetic lens used in TEM had limited its spatial resolution to a level of about 2 angstrom for half a century until the invention of aberration correctors. The successful incorporation of an aberration corrector to a TEM, originally suggested by Scherzer [5], has taken a great step forward for the development of electron microscope resolution [6, 7], which pushed the spatial resolution of TEM into an era of sub-angstrom without involving complex computation [8-10]. More recently, with optimized hollow-cone condition of aberration-corrected TEM, a sub-0.5 angstrom has been achieved under an intermediated accelerated voltage [11].

Since the advent of dedicated STEM, high-angle annular dark-field (HAADF) has been the main imaging mode because of its robust in contrast explanation where the contrast is approximately proportional to the $Z^{1.7}$ (Z is the atomic number of element) [12]. It is powerful to imaging the heavy atoms in the materials due to their strong scattering capability to incoming electrons. However, the imaging of light elements, such as Li or O ions in the lithium electrode materials, is still a challenge due to their small scattering cross sections for the incoming electrons. When the light and heavy elements coexist in an electrode material, the weak signal from lithium and oxygen are mostly submerged by strong signal from heavy elements, making light atoms invisible for observation. This awkward situation has been overcome because of the appearance of annular-bright-field (ABF) imaging mode [13], where the contrast of atomic columns is approximately proportional to the $Z^{1/3}$, which is very approximate to the imaging of light elements. Okunishi *et al.* [14] impressed the world by the imaging O column in SrTiO_3 and N column in Si_3N_4 by an annular bright-field detector, which O and N were clearly visualized but invisible in the HAADF images. Findlay *et al.* further demonstrated the robust capability of ABF imaging in O column in SrTiO_3 and TiO_2 lattice and did lots of meaningful theoretical works for its contrast mechanism [15-19]. Lithium ion in LiV_2O_4 lattice was also directly imaging by Oshima *et al.* [20]. Subsequently, imaging light elements, such as lithium and hydrogen, has been emerged in extensive studies. More details about its origin and principle can be found elsewhere [15, 16].

The detection geometry of ABF and HAADF imaging can be illustrated by the schematics in Fig. 1, where the ABF image is contributed by the scattering electron ranging from an inner angle α_0 (about a half of outer angle α) to the outer angle

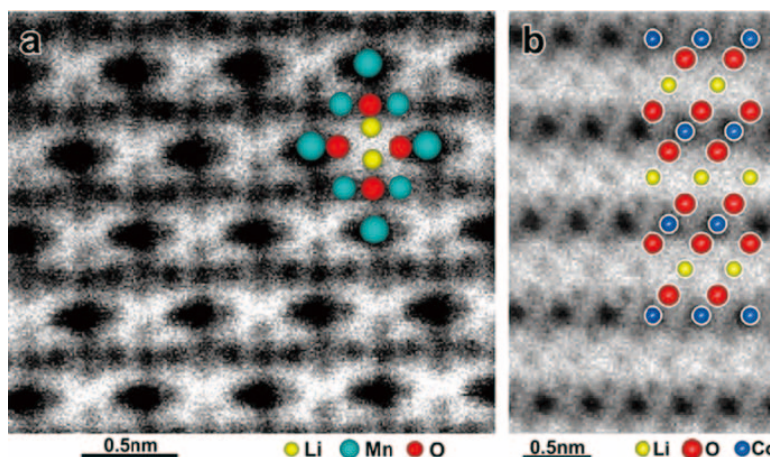
α (coincident with converge angle α), for example, from 11 mrad to 22 mrad; HAADF usually collected signal from a high enough angle to avoid the diffraction effect at low and mediate angle, for example, from ~ 150 mrad to ~ 250 mrad or more. Numerous experimental and theoretical evidences [17, 18, 21] have already confirmed the powerful capability of ABF imaging mode in visualizing both light and heavy atoms, the contrast of which is insensitive to the variation of specimen thickness and defocus values, allowing direct interpretation from the imaging without complex simulations. Figure 2a shows an ABF image of the subsurface region of a LiMn_2O_4 particle viewed along [100] with a detection angle of 6–25 mrad, where the Li ions are clearly visible together with the O and Mn columns. A slightly shift of Li columns away from their original positions

Fig. 1



Schematic illustration of HAADF and ABF imaging geometry and EELS collection. A fine electron probe with convergent semi-angle α is focused to sub-angstrom dimension and scans across the specimen. An HAADF detector at the post column subtends a detecting angle ranging from β_1 to β_2 ; the ABF detector from α_0 to α . The EELS spectrometer is located beneath the STEM column.

Fig. 2



(a) ABF images of tetragonal LiMn_2O_4 spinel nanoparticles along zone axis [100] taken with a JEOL JEM-2100F; (b) A typical ABF image of a LiCoO_2 thin film viewed along the [-1-120] zone axis with the Li columns clearly visible. Both of the crystal structure models are superposed. Reproduced from ref. [22].

due to the presence of O vacancies is also visualized. Figure 2b shows a typical ABF image obtained from the LiCoO_2 thin film viewed along $[-1-120]$. Li sites as well as O and Co sites can be clearly distinguished according to the image contrast, well conformable to the inserted atomic structure model. As a result, the aberration-corrected sub-angstrom electron probe combined with the ABF detection geometry has dramatically enhanced its performance of atomically resolved microscopy and spectroscopy, especially opening up new opportunities to study the atomic structure of battery materials containing light elements.

In this article, we demonstrate the key role of aberration-corrected STEM in revealing critical atomic-scale structure features of electrode materials under different charge and/or discharge state, including the migration of transition metal ions, two- and three-phase interface structures. The powerful capability of ABF imaging technique for visualizing light elements has been exhibited and emphasized. The role of atomic resolved electron energy loss spectroscopy (EELS) in characterizing the electronic structure of electrode materials was also demonstrated, indicating its potential applications in future. Based on these atomic-scale investigations, the relationship between atomic-level structure evolution and microscopic reaction mechanisms in electrode materials has been discussed and envisaged.

Migration of transition metal ions

In LIBs, there is recognition that migration of transition metal ions is responsible for the voltage fading, capacity decay and poor rate capability [23-25]. Here we select Li_2MnO_3 and $\text{LiNi}_{0.5}\text{Mn}_{1.5}\text{O}_4$ as demo cases to illustrate the STEM imaging of ions migration dynamics corresponding to the partially delithiation and re-lithiation state, aiming to provide an atomic scale insight to the degradation mechanism of Mn-based cathode

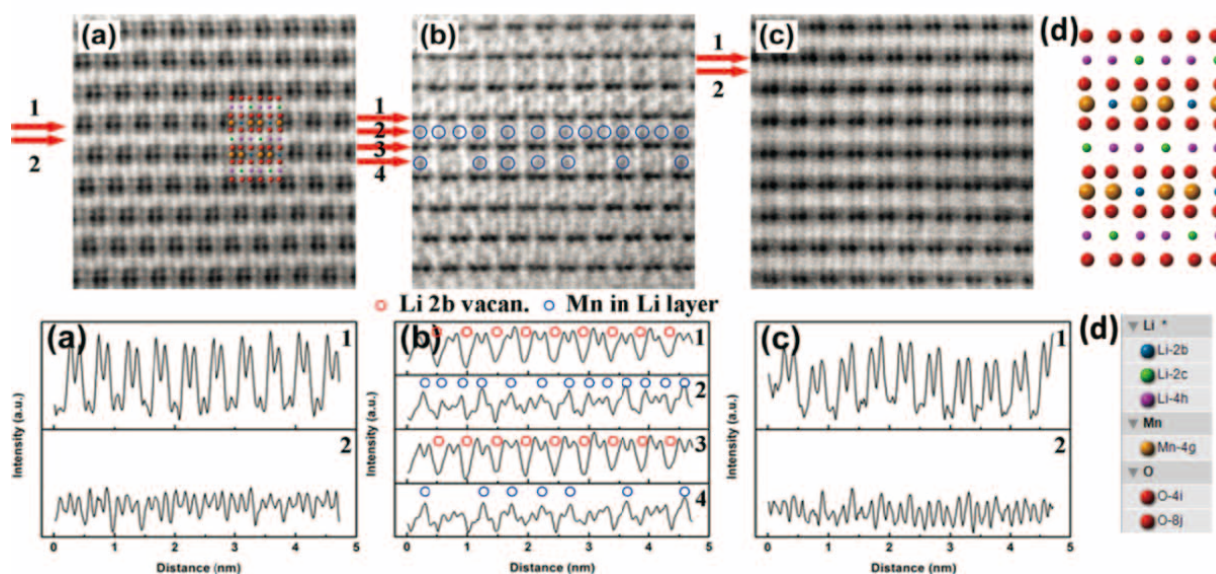
materials.

Li_2MnO_3

Li_2MnO_3 is an important component in the family of lithium- and manganese-rich (LMR) layered composite oxides, which are very promising cathode materials for high energy density LIBs due to their much higher reversible capacity (>250 mAh/g) when cycled to high cut-off voltage ($\geq 4.5\text{V}$) [26-29]. The layered structure of Li_2MnO_3 belongs to space group $C2/m$, the parameters of the cell are $a = 4.937(1)$ Å, $b = 8.532$ Å, $c = 5.030(2)$ Å, and $\beta = 109.46(3)^\circ$. Lithium ions occupy the 2b (0, 1/2, 0), 2c (0, 0, 1/2), and 4h (0, 0.6606(3), 1/2) sites, manganese ions the 4g (0, 0.16708(2), 0) site, and oxygen ions the 4i (0.2189(2), 0, 0.2273(2)) and 8j (0.2540(1), 0.32119(7), 0.2233(1)) sites, in which the subscripts 2c, 4h, 2b, 4g, 4i, and 8j are the lattice sites occupied by the atoms in the round brackets, so that the chemical formula of Li_2MnO_3 can be written as $\{(\text{Li}_{1/2})_{2c}(\text{Li}_1)_{4h}\}_x\{(\text{Li}_{1/2})_{2b}(\text{Mn}_1)_{4g}\}(\text{O}_1)_{4i}(\text{O}_2)_{8j}$ [30-33].

By virtue of ABF imaging, Wang *et al.* [34] studied the atomic structures of Li_2MnO_3 before and after partial delithiation and re-lithiation; all atoms in Li_2MnO_3 have been visualized directly in ABF images. The reversible insertion and desorption process of the lithium on the LiMn_2 planes have been visualized clearly. It has been also found that some manganese atoms can reversibly migrate into and out of the Li layer in the shallow charge and discharge process. **Figure 3** exhibited ABF images and corresponding line profile analysis of contrast changes of Li_2MnO_3 at different electrochemical states. Note that in ABF imaging mode, the atom column manifests itself as dark spots due to absorption-type contrast exhibited by ABF imaging [15]. As shown in Fig. 3d, viewed along the $[110]$ zone axis of the Li_2MnO_3 , the LiMn_2 layer was composed of two adjacent Mn columns alternating with Li column in the form of "... Mn-Mn-Li-Mn-Mn-Li...", which was clearly confirmed in the ABF image and corresponding line profile (Line 1) in Fig. 3a.

Fig.3



ABF images and corresponding line profile of changes of Li planes and LiMn_2 plane of Li_2MnO_3 after electrochemical lithiation and delithiation taken with a JEOL JEM-ARM200F. (a) pristine Li_2MnO_3 ; (b) Li_2MnO_3 charged to 4.8 V; and, (c) Li_2MnO_3 discharged to 2.0 V after being charged to 4.8 V. (d) presents the projected structure model of Li_2MnO_3 along the $[110]$ direction, where the Wyckoff positions of each ions have been labeled with different colors shown in the bottom panel. Note that all ABF images were viewed along the $[110]$ orientation and image contrast of the dark dots is inverted and showed as peaks in the ABF line profile. Reproduced from ref. [34].

Upon initial charging to 4.8V, a "...Mn-Mn-V_{Li}-Mn-Mn-V_{Li}..." characteristic can be visualized in Line 1 and Line 3 in Fig. 3b, indicating that Li has been extracted. The Li re-inserted into the LiMn₂ layer after being discharged to 2.0 V, as demonstrated by Line 1 in Fig. 3c. Thus, it can be concluded that Li insertion into and deinsertion from the LiMn₂ layer are reversible. In addition, the Mn ions in the Li layers had been imaged as some grey spots (marked by the blue circles), and it is unexpected that the Mn can also migrated into and out of the lithium layer reversibly when discharged to 2.0 V by comparing the line profiles from lithium layer in Li₂MnO₃ with different charge/discharge state. This is totally different from irreversible migration of Mn resulting in a structure with spinel-like features in Li₂MnO₃ [35-37].

Afterwards the direct visualization of high mobility of Mn ions, phenomenological model and neutron powder diffraction experiment jointly supported that the migration of Mn has negatively influence on the reaction kinetics of Li₂MnO₃ component in LMR layered cathode materials; the irreversible migration of TM ions (Mn), often accompanied by a structural evolution, lead to the voltage fade in LMR layered oxide [38, 39]. Unfortunately, the cations migration between TM layer and lithium layer seems to be an intrinsic feature of the charge-discharge process in the lithium-rich phase [40], which is an unavoidable challenge to stabilize the host structure and raise the cycling performance of electrode materials. Therefore, minimizing TM ions migration to prevent structural transformation is the key to improve the voltage fade in LMR layered cathodes during operation. To solve this problem, Ni doped $x\text{Li}_2\text{MnO}_3 \cdot (1-x)\text{LiMn}_{0.5}\text{Ni}_{0.5}\text{O}_2$ composite materials has been proposed and verified as a good choice to suppress the migration of Mn by controlling the complex interaction between Mn and Ni [41, 42]. The effect of Ni in stabilizing the LMR layered cathode has been attributed to the decrease of unstable Mn³⁺ by preventing transformation of Mn⁴⁺ upon discharge [43].

Spinel LiNi_{0.5}Mn_{1.5}O₄

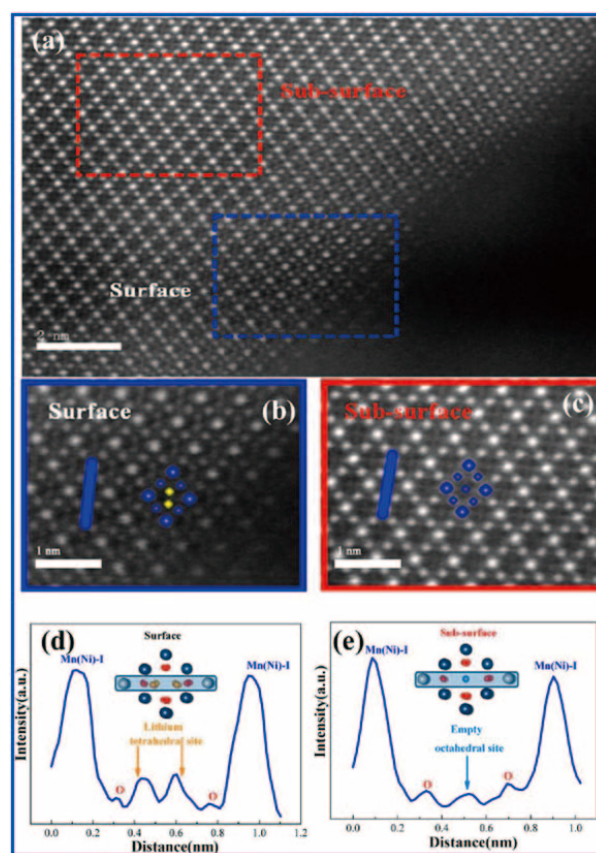
Among numerous cathode materials for LIBs, high-voltage spinel LiNi_{0.5}Mn_{1.5}O₄ has attracted much attention because of its high power capability with an operating voltage of 4.7 V, a practical reversible capacity of ~135 mA h/g, and a high specific energy (~640 W h/kg) [44, 45]. However, LiNi_{0.5}Mn_{1.5}O₄/graphite full-cells display severe capacity degradation hindering its practical application, especially its poor first-cycle Coulombic efficiency. The mechanisms of capacity degradation are not well understood but structure-related Mn dissolution have been commonly considered as a highly possible cause [45-47].

By an aberration-corrected STEM, Lin *et al.* [48] investigated details of locally atomic-level and average structure of Ni_{0.5}Mn_{1.5}O₄ during first cycle (3.5–4.9 V) at room temperature. Two types of local atomic-level migration of TM ions in the cathode of a well-prepared LiNi_{0.5}Mn_{1.5}O₄/Li half-cell during first charge: i) Migration of TM ions into tetrahedral Li sites to form a Mn₃O₄-like structure at surface regions (~2 nm) of the cycled LiNi_{0.5}Mn_{1.5}O₄ particles. ii) Migration of TM ions into empty octahedral sites to form a rocksalt-like structure at subsurface regions of the cycled particles. It was found that the migration of these TM ions are closely related to dissolution of Ni/Mn ions and building-up of charge transfer impedance, which contribute significantly to the capacity degradation and the poor first-cycle Coulombic efficiency of spinel LiNi_{0.5}Mn_{1.5}O₄ cathode material. **Figure 4a** exhibits a typical HAADF image containing surface and subsurface regions of the first-charged (to 4.9 V) LiNi_{0.5}Mn_{1.5}O₄ viewed along the [110] crystallographic

direction. In this projected direction, the positions of Ni and Mn atomic columns can be clearly identified, which form a diamond configuration of contrast. Since the projected density of the Mn(Ni)-I column is twice that of the Mn(Ni)-II column in this crystallographic direction, the strongest contrast is assigned to the Mn(Ni)-I and the slightly weaker one is assigned to the Mn(Ni)-II. O atomic column can also be identified without difficulty in the HAADF image, whereas Li atomic column can hardly be observed due to its weak scattering factor.

At the surface region, as shown in Fig. 4b, a Mn₃O₄-like structure can be identified; the presence of weak contrast in the tetrahedral Li sites suggested the Ni/Mn migration, rather than Li or O due to their weak scattering power. Further, the degree of migration of TM ions into the tetrahedral Li sites had been evaluated by the relative intensity of the image contrast. According to the line profile in Fig. 4d, the contrast caused by migration of TM ions is only ~26% of that Mn(Ni)-I, occupied by TM ions, versus ~50% of fully occupied by TM ions in an ideal Mn₃O₄ phase, indicating that the tetrahedral Li sites are only partially occupied by TM ions. However, at the sub-surface region as shown in Fig. 4c, definite presence of weak contrast can be visualized and identified as migration of TM ions in the center of the diamond configuration. According to

Fig. 4



(a) A typical STEM image showing the surface and subsurface regions of the first-charged sample taken with a JEM-ARM200F; (b and c) enlarged regions of the surface and subsurface corresponding to the blue and red boxes in panel (a), respectively; (d and e) line profiles corresponding to the blue lines in panels (b) and (c), respectively. [Schematic lattice structures are overlaid in (b)–(e).] Reproduced from ref. [48].

the crystal structure of spinel viewed along the [110] direction, the center of the diamond configuration is closely related to the empty octahedral sites. Thus, at the sub-surface region, TM ions migrate to the empty octahedral sites, which is similar to the contrast associated with the formation of a rocksalt structure in layered and lithium-rich layered cathode materials during electrochemical cycling [49], [50]. Similarly, the line profiles plotted in Fig. 4e showed a relative intensity of ~8% of the neighbored Mn(Ni)-I columns, indicating that the migration of TM ions with the formation of the rocksalt-like structure in the subsurface regions is also very limited. In addition, more HAADF images demonstrated that this type of rocksalt-like structure was also found in some isolated bulk regions of the first-charged sample.

As a result, both Ni and Mn migrated to the tetrahedral sites and the empty octahedral sites in the first charged sample. Based on atomic scale experimental evidences and electronic structure characterization, correlations between Mn dissolution and the surface Mn_3O_4 -like structure, electrochemical performance and local structural distortions have been discussed. It was concluded that the surface Mn_3O_4 -like structure could contribute to the dissolution of TM ions. This structure, as well as rocksalt-like structures with heavy TM ions on the lithium pathways, blocks the migration of Li ions, resulting in the accumulation of charge transfer impedance and, consequently, the degradation of capacity, also contributing to the poor first cycle Coulombic efficiency. These finding also suggested a possible way to suppress the migration of TM ions by preoccupying of the tetrahedral Li sites in the surface of spinel $\text{LiNi}_{0.5}\text{Mn}_{1.5}\text{O}_4$ by a small amount of insoluble ions to stabilize its structure and improve its electrochemical performance.

As a summary, atomic-level details of migration of TM ions mentioned above provide us new insights into correlation between the structure destabilization and performance degradation, shedding light on optimizing the composition and tailoring atomic-scale structure of electrode materials to improve its electrochemical performance.

Phase interface

Besides analyzing the degradation mechanism, STEM can also contribute to energy storage and conversion of LIBs involving the motions of lithium ions in the anodes or cathodes. Accompanying the insertion and extraction of lithium ions, variation of Li content in electrodes would introduce the phase transition in some electrodes. Understanding the dynamics of phase transition is indispensable to improve the rate capability of these electrodes. Here we introduce our works on phase interface in partially delithiated LiPF_4 and lithiated $\text{Li}_4\text{Ti}_5\text{O}_{12}$, expecting to give some view on the phase transition reaction mechanism.

Staging Interface in Partially Delithiated LiFePO_4

The olivine LiFePO_4 has attracted tremendous attention since the first report by Padhi *et al* [51]. After intensive studies for about ten years, LiFePO_4 modified with decreased particle sizes [52] and carbon coating [53] becomes a promising cathode material in LIBs and commercially available for hybrid electric vehicles and stationary energy storage at present due to its reversible and high-rate lithium insertion-deinsertion. Despite the great success in practical applications, the microscopic mechanism of the phase transition from LiFePO_4 to FePO_4 is still under debate; a variety of models, such as core-shell [51], shrinking core [54], mosaic [55], domino-cascade [56], and

many particles model [57], have been proposed. Therefore, direct visualization of the Li ions and inspect on the structure evolution of delithiated LiFePO_4 become indispensable to clarify these controversies.

Gu *et al.* [58] applied the ABF imaging on partially delithiated LiFePO_4 nanowires at the beginning of development of ABF detection configuration early in 2011, not only directly imaging the positions of Li ions but also revealed a new “staging” structure, challenging the conventional phase separation models. This firstly imaging of the Li states in Li_xFePO_4 triggers a trend of atomic scale investigations by ABF imaging technique, extending the understanding of this kind of electrochemical reaction mechanism. This finding demonstrated that an intermediated phase $\text{Li}_{0.5}\text{FePO}_4$ with staging feature, instead of phase separation, is responsible for the insertion and extraction of Li ions, providing a new insight into the two-phase reaction mechanism.

However, the origin of the formation mechanism of this lithium staging structure is not clear. What are the decisive factors for the formation of the lithium staging structure, particles size, morphology, doping, or charging rate? To answer this question, the ABF imaging technique had played the crucial role again in revealing this nano-sized structure features. Suo *et al.* [60] investigated partially chemically delithiated Nb-doped LiFePO_4 with particle size of ≈ 200 nm by ABF imaging; a buffer layer of staging structure with a width of ~ 2 nm was identified between LiFePO_4 and FePO_4 . The presence of this intermediate phase acts as a relaxation layer to accommodate the volume mismatch ($\sim 6.8\%$) between LiFePO_4 and FePO_4 and is beneficial to the structure stability during the charge-discharge cycles. Subsequently, Zhu *et al.* [59] systematically investigated the size dependence of the staging phenomena in Li_xFePO_4 particles with 70 nm and 50 nm and found that for the small nanoparticles (50 nm) with a nominal composition $\text{Li}_{0.5}\text{FePO}_4$, a homogeneous staging structure existed all through the particles while for larger particles (70 nm) with an overall composition of $\text{Li}_{0.9}\text{FePO}_4$, the width of the $\text{Li}_{0.5}\text{FePO}_4$ staging structure between LiFePO_4 and FePO_4 extends to ~ 15 nm. More importantly, a distinct three-phase boundary with coexistence of LiFePO_4 /staging phase/ FePO_4 , totally different from the conventional two-phase models, as shown in Fig. 5, was revealed in the ABF images. The staging area is marked by the dashed yellow lines. The structure characteristics of LiFePO_4 phase, FePO_4 phase and interfacial phase with staging structure were verified in enlarged ABF images displayed in Fig. 5b, 5c and 5d. The line profiles from Li-columns layers as indicated by different colors confirmed the staging structure (also be referred as staging II phase) which formed the interfacial regions between LiFePO_4 and FePO_4 . Based on the observations on various staging phenomena and theoretical analysis, it was concluded that the staging phase can form a distinct intermediate between LiFePO_4 and FePO_4 both in spatial (size-dependent interphase) as well as temporal sense (structural attractor on de/lithiation).

Zero-strained interface in $\text{Li}_4\text{Ti}_5\text{O}_{12}$ anode

The spinel-structured $\text{Li}_4\text{Ti}_5\text{O}_{12}$ was proposed as the alternative anode materials to carbon because of its higher lithiation voltage plateau (1.55 V vs Li/Li^+) and excellent zero-strained structural reversibility [61-63]. It has been commonly accepted that the lithium insertion and extraction is accompanied by the displacement of Li ions from the 8a sites to the 16c sites, resulting in the phase transformation from spinel $(\text{Li})_{8a}[\text{Li}_{1/3}\text{Ti}_{5/3}]_{16d}(\text{O}_4)_{32c}$ ($\text{Li}_4\text{Ti}_5\text{O}_{12}$) to $(\text{Li})_{16c}[\text{Li}_{1/3}\text{Ti}_{5/3}]_{16d}(\text{O}_4)_{32c}$ ($\text{Li}_7\text{Ti}_5\text{O}_{12}$) with ordered rock-salt-type structure [64, 65].

However, direct atomic scale observation for this two-phase mechanism is lacking before the development of ABF imaging technique. Lu *et al.* [21] successfully applied the ABF imaging to the lithiated $\text{Li}_4\text{Ti}_5\text{O}_{12}$ and a sharp phase boundary separating $\text{Li}_4\text{Ti}_5\text{O}_{12}$ and $\text{Li}_7\text{Ti}_5\text{O}_{12}$ was clearly found, providing solid experimental evidence for the two-phase reaction mechanism. In addition, the doping by extra-large ion Br into the $\text{Li}_4\text{Ti}_5\text{O}_{12}$ lattice have shown an improved electrical conductivity, which was examined in the aberration-corrected electron microscope and found the occupation of Br ions at the specific O sites by Yang *et al.* [66]. Density function theory calculations suggested that introducing of large Br ions (with a radius of 182 pm) caused a distortion of nearby atoms and a slight lattice extension, improving the electrical conductivity and lithium diffuse rate. This result demonstrated that this lattice has a very large accommodation for foreign ions.

Then, how about the situation where the Na ions with a large radius (102 pm) shuttle among the spinel lattice? Can Na ions insert/de-insert the $\text{Li}_4\text{Ti}_5\text{O}_{12}$ lattice reversibly? The two-phase reaction mechanism can still hold? Is there a different Na storage mechanism? These issues have attracted much concern in the investigations of the sodium ion batteries (SIBs) renewed for its low cost and infinite sodium resource [67-69]. In response, Sun *et al.* [70] predicted and subsequently confirmed a three-phase storage mechanism in $\text{Li}_4\text{Ti}_5\text{O}_{12}$ anodes for room-temperature sodium-ion batteries. The interfacial structure is clearly resolved at an atomic scale in electrochemically sodiated $\text{Li}_4\text{Ti}_5\text{O}_{12}$ for the first time by the ABF imaging. **Figure 6** exhibits a typical three-phase coexistence region, where the Li4 phase ($\text{Li}_4\text{Ti}_5\text{O}_{12}$), Li7 phase ($\text{Li}_7\text{Ti}_5\text{O}_{12}$) and Na6Li phase ($\text{Na}_6\text{LiTi}_5\text{O}_{12}$) can be identified clearly in the ABF images, assisted by the intensity analysis of line profiles across the 8a and 16c sites. Besides the atomic-scale coherent interface between Li4 phase and Li7

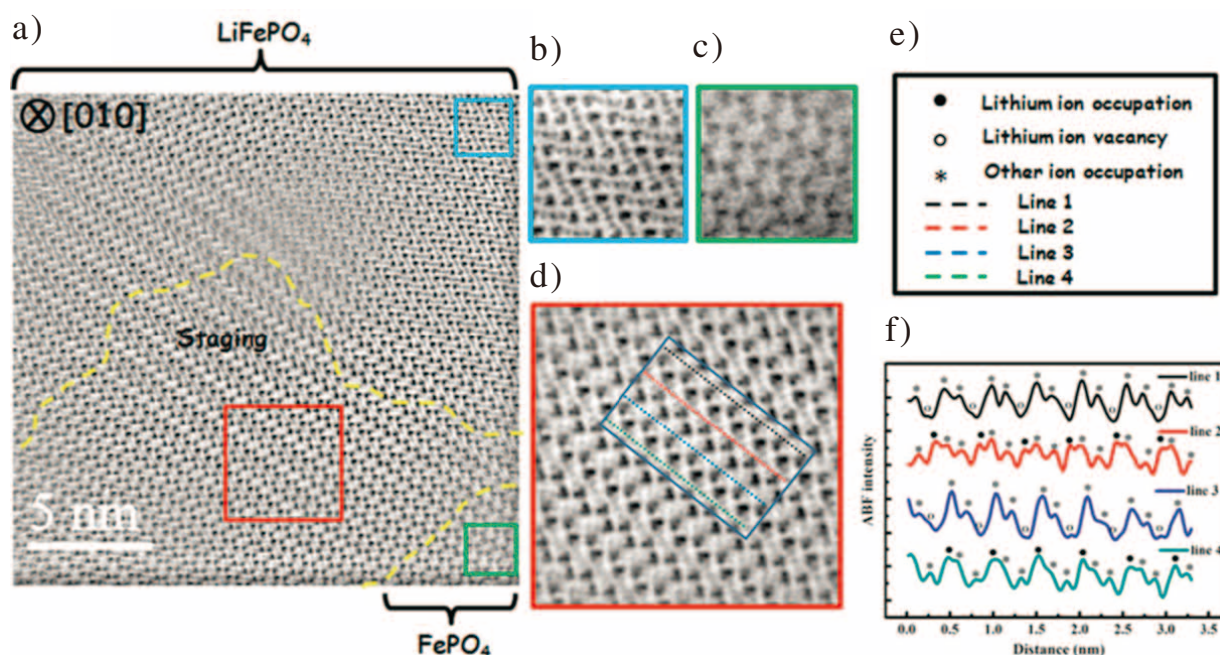
phase as reported by Lu *et al.* [59], it is interesting to note that a sharp interface between Li7 and Na6Li was observed despite of the large volume change (more than 12%), which calls for further illumination. This result has further supported by the refinement of in situ synchrotron X-ray diffraction patterns from chemically sodiated $\text{Li}_4\text{Ti}_5\text{O}_{12}$ [71]. The unique three-phase coexistence phenomenon of three phase coexistence refreshes current understanding of phase transition mechanism, implying new electrochemistry in Na-ion battery systems different from LIBs counterpart.

Electronic structures of SIBs materials

Despite HAADF and ABF imaging techniques have a powerful capability in revealing the atomic structure of electrode materials, the information of electronic structure is sometimes indispensable to analyze the structure-property relationship. The EELS spectrometer equipped beneath the STEM column (as shown in Fig. 1) is suitable for imaging chemical composition and electronic properties in real space. After successfully implementation of aberration correctors in the STEM equipped with a cold-field emission gun in recent years, a sub-angstrom probe with high current makes the atomic resolved EELS with improved signal-to-noise ratio truly feasible in routine practice [72]. Numerous applications can be found in functional oxides [73], providing new and deep insights for atomistic understandings. Here we demonstrate its application in identifying the chemical nature and valence state of Ti and Mn in Na-rich $\text{Na}_{0.66}\text{[Mn}_{0.66}\text{Ti}_{0.34}]\text{O}_2$, which may indicate its potential application of EELS in SIBs.

Tunnel-type structured $\text{Na}_{0.44}\text{[Mn}_{0.66}\text{Ti}_{0.34}]\text{O}_2$ is a positive electrode material for aqueous SIBs with advantages of low

Fig. 5



(a) ABF image of 70 nm LiFePO_4 viewed at the [010] zone axis taken with a JEM-ARM200F. The staging area is marked by the dashed yellow lines. (b-d) Enlarged images of LiFePO_4 , FePO_4 phase and interfacial phase with staging structure, corresponding to tube, green and red squares, respectively in (a). (e, f) the line profiles from the ABF image corresponding to the different colored lines in (d). Note that in the ABF line profile, image contrast of the dark dots is inverted and showed as peaks. Reproduced from ref. [59].

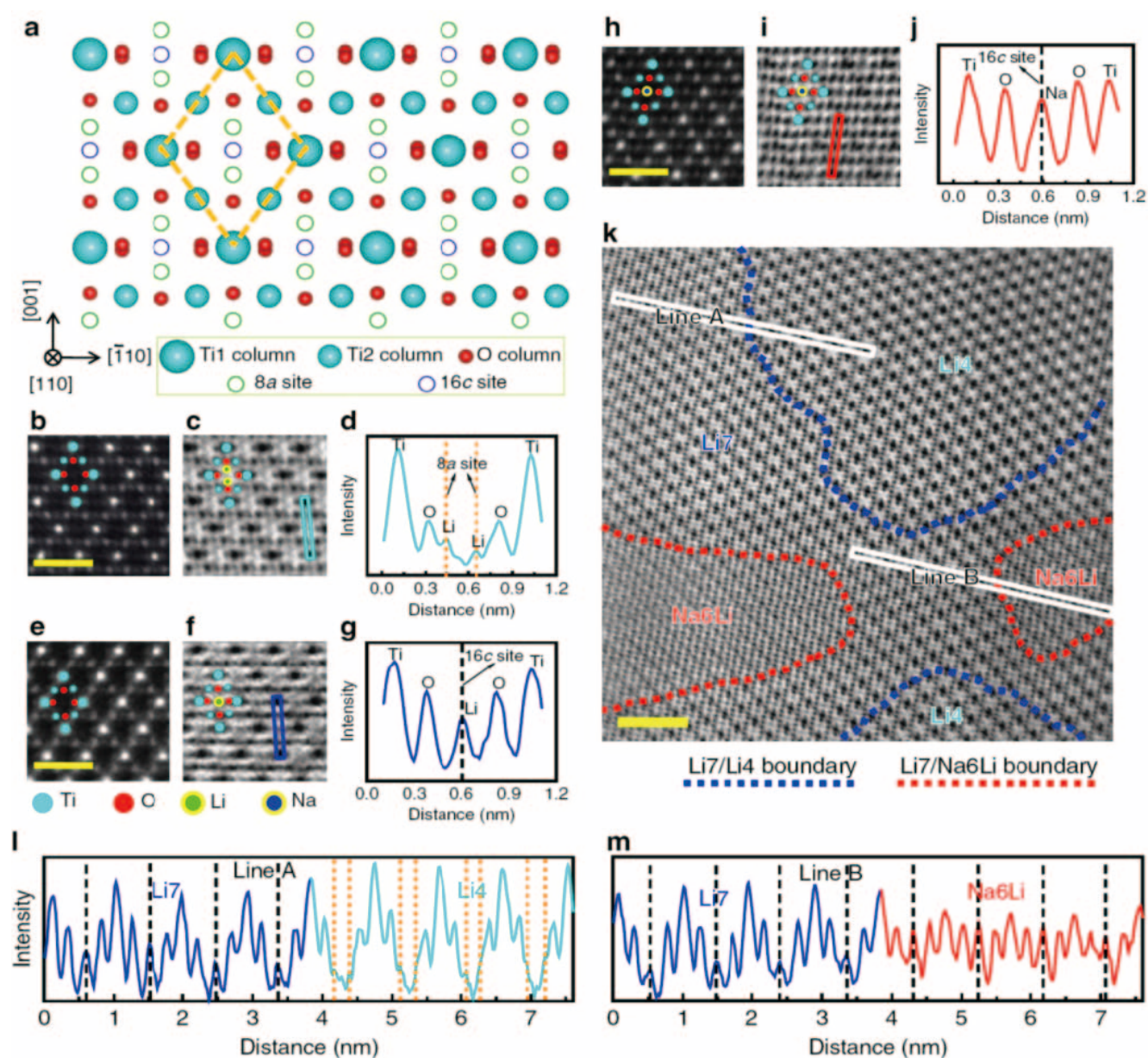
cost and high safety, containing a large S-shape tunnel and a small tunnel filled by Na ions. However, a very low capacity (30~40 mAhg⁻¹) hinder its practical application. Wang *et al.* [74] synthesized a Na-rich Na_{0.66}[Mn_{0.66}Ti_{0.34}]O₂ with a highest capacity of 76 mAhg⁻¹ by a simple solid state reaction method; its structure is highly needed to be clarified for understanding of Na-ions transporting. **Figure 7** exhibited the HAADF and STEM-EELS results of Na_{0.66}[Mn_{0.66}Ti_{0.34}]O₂, where the tunnel structure with large S-shape and small tunnels can be identified directly. The valence states of Mn³⁺ and Ti⁴⁺ were confirmed by their *L* edges displayed in Fig. 7b and 7c. From the line scan of atomic-resolved EELS in Fig. 7d, the element specimen and valence state at five Mn sites had been analyzed. It was found

that Mn(1), Mn(3), Mn(4) are occupied by both Mn and Ti while Mn(2) site is mainly filled with Mn ions. No signal from Ti can be seen at Mn(5) site. These results are in good agreement with the refinement of XRD pattern, indicating the potential of atomic resolved EELS in characterizing chemical and electronic structures of electrode materials.

Summary

In this review, we have demonstrated how the aberration-corrected STEM imaging methods could disclose the atomic-scale structural details in different kinds of electrode materials under early equilibrated electrochemical states. With help of

Fig. 6



STEM imaging of a three-phase coexistence region taken with a JEM-2100F. (a) Crystal structure of spinel $\text{Li}_4\text{Ti}_5\text{O}_{12}$ viewed from the $[110]$ crystallographic direction showing separated Ti and O columns. Ti1 and Ti2 columns with different atom densities are represented by balls of different size. HAADF (b), ABF (c) images and ABF line profile (d) of $\text{Li}_4\text{Ti}_5\text{O}_{12}$ (Li_4) phase. Scale bar, 1 nm. HAADF (e), ABF (f) images and ABF line profile (g) of $\text{Li}_7\text{Ti}_5\text{O}_{12}$ (Li_7) phase. Scale bar, 1 nm. HAADF (h), ABF (i) images and ABF line profile (j) of $\text{Na}_6\text{LiTi}_5\text{O}_{12}$ (Na_6Li) phase. Scale bar, 1 nm. (k) ABF image in the half electrochemically sodiated $\text{Li}_4\text{Ti}_5\text{O}_{12}$ nano-particle. Scale bar, 2 nm. (l, m) Line profiles crossing the Li_7/Li_4 (line A) and $\text{Li}_7/\text{Na}_6\text{Li}$ (B) boundary, respectively. Reproduced from ref. [70].

the atomic-scale ABF imaging, the occupation information about light elements (such as O or Li atoms) becomes routinely available. The migration of TM ions in lithium rich layered oxide Li_2MnO_3 , atomic details of two- and three-phase interfacial structures in LiFePO_4 and $\text{Li}_4\text{Ti}_5\text{O}_{12}$ electrode materials were successfully revealed directly. In addition, the application of atomic resolved EELS in characterizing the electronic structure of electrode materials was also demonstrated. These achievements have bridged the atomic-scale structure evolution and macroscopic electrochemical behaviors, thereby providing critical clues to improve the battery's performances. It is also believed that the ABF imaging technique and atomic resolved EELS will continuously contribute to the structure–property correlation of electrodes for developing new materials, and more surprising atomistic discoveries can be expected.

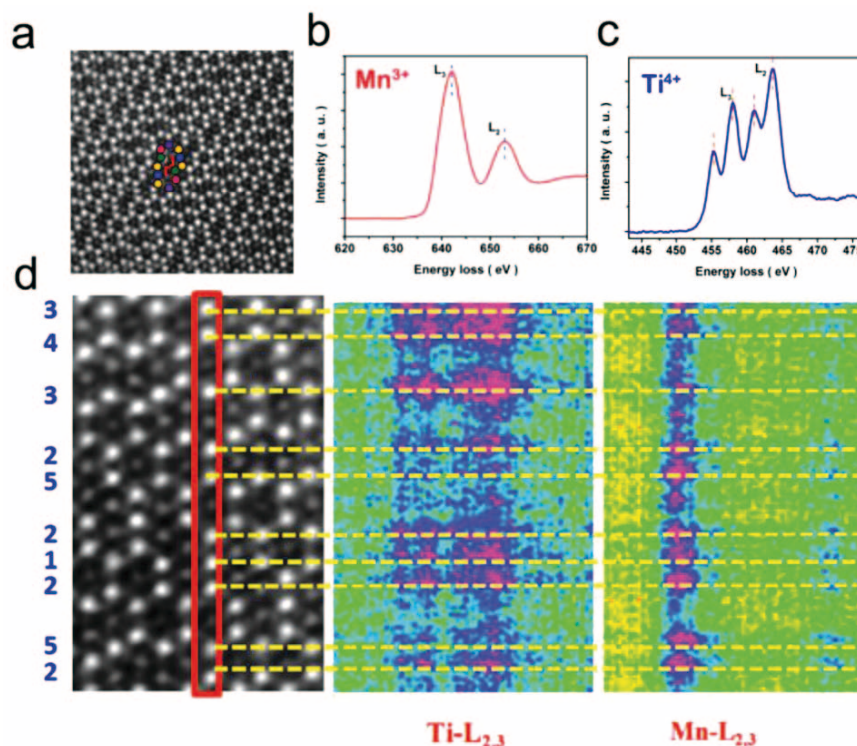
Acknowledgments

The author is grateful for Dr. D. Xiao for meaningful discussions about the lithium storage mechanism.

References

- [1] M. Armand, J.M. Tarascon, *Nature*, **451** (2008) 652-657.
- [2] P.G. Bruce, B. Scrosati, J.-M. Tarascon, *Angew. Chem. Int. Ed.*, **47** (2008) 2930-2946.
- [3] B. Dunn, H. Kamath, J.M. Tarascon, *Science*, **334** (2011) 928-935.
- [4] L. Gu, D. Xiao, Y.-S. Hu, H. Li, Y. Ikuhara, *Adv. Mater.*, **27** (2015) 2134-2149.
- [5] O. Scherzer, *J. Appl. Phys.*, **20** (1949) 20.
- [6] M. Haider, H. Rose, S. Uhlemann, E. Schwan, B. Kabius, K. Urban, *Ultramicroscopy*, **75** (1998) 53-60.
- [7] M. Haider, S. Uhlemann, E. Schwan, H. Rose, B. Kabius, K. Urban, *Nature*, **392** (1998) 768-769.
- [8] R. Erni, M.D. Rossell, C. Kisielowski, U. Dahmen, *Phys. Rev. Lett.*, **102** (2009) 096101.
- [9] P.C. Tiemeijer, M. Bischoff, B. Freitag, C. Kisielowski, *Ultramicroscopy*, **114** (2012) 72-81.
- [10] M.A. O'Keefe, C.J.D. Hetherington, Y.C. Wang, E.C. Nelson, J.H. Turner, C. Kisielowski, J.O. Malm, R. Mueller, J. Ringnalda, M. Pan, A. Thust, *Ultramicroscopy*, **89** (2001) 215-241.
- [11] R. Ishikawa, E. Okunishi, H. Sawada, Y. Kondo, F. Hosokawa, E. Abe, *Nat. Mater.*, **10** (2011) 278-281.
- [12] N.D. Browning, M.F. Chisholm, S.J. Pennycook, *Nature*, **366** (1993) 143-146.
- [13] P.E. Batson, *Nat. Mater.*, **10** (2011) 270-271.
- [14] E. Okunishi, I. Ishikawa, H. Sawada, F. Hosokawa, M. Hori, Y. Kondo, *Microsc. Microanal.*, **15** (2009) 164-165.
- [15] S.D. Findlay, N. Shibata, H. Sawada, E. Okunishi, Y. Kondo, T. Yamamoto, Y. Ikuhara, *Appl. Phys. Lett.*, **95** (2009) 191913.
- [16] S.D. Findlay, N. Shibata, H. Sawada, E. Okunishi, Y. Kondo, Y. Ikuhara, *Ultramicroscopy*, **110** (2010) 903-923.
- [17] S.D. Findlay, S. Azuma, N. Shibata, E. Okunishi, Y. Ikuhara, *Ultramicroscopy*, **111** (2011) 285-289.
- [18] S.D. Findlay, N.R. Lugg, N. Shibata, L.J. Allen, Y. Ikuhara, *Ultramicroscopy*, **111** (2011) 1144-1154.
- [19] S.D. Findlay, Y. Kohno, L.A. Cardamone, Y. Ikuhara, N. Shibata, *Ultramicroscopy*, **136** (2014) 31-41.
- [20] Y. Oshima, H. Sawada, F. Hosokawa, E. Okunishi, T. Kaneyama, Y. Kondo, S. Niitaka, H. Takagi, Y. Tanishiro, K. Takayanagi, *J. Electron Microsc.*, **59** (2010) 457-461.
- [21] E. Okunishi, H. Sawada, Y. Kondo, *Micron*, **43** (2012) 538-544.
- [22] R. Huang, Y. Ikuhara, *Curr. Opin. Solid State Mater. Sci.*, **16** (2012) 31-38.
- [23] M. Balasubramanian, J. McBreen, I.J. Davidson, P.S. Whitfield, I. Kargina, *J. Electrochem. Soc.*, **149** (2002)

Fig. 7



STEM imaging. (a) General view of the crystal structure and view along [001] zone axis taken with a JEM-ARM200F. Electron energy-loss spectra (EELS) for (b) Mn-L_{2,3} and (c) Ti-L_{2,3} edges for the pristine $\text{Na}_{0.66}[\text{Mn}_{0.66}\text{Ti}_{0.34}]\text{O}_2$. (d) The STEM-EELS image of $\text{Na}_{0.66}[\text{Mn}_{0.66}\text{Ti}_{0.34}]\text{O}_2$. Reproduced from ref. [74].

- A176-A184.
- [24] J. Bréger, Y.S. Meng, Y. Hinuma, S. Kumar, K. Kang, Y. Shao-Horn, G. Ceder, C.P. Grey, *Chem. Mater.*, **18** (2006) 4768-4781.
- [25] A.R. Armstrong, M. Holzapfel, P. Novák, C.S. Johnson, S.-H. Kang, M.M. Thackeray, P.G. Bruce, *J. Am. Chem. Soc.*, **128** (2006) 8694-8698.
- [26] C.S. Johnson, J.S. Kim, C. Lefief, N. Li, J.T. Vaughey, M.M. Thackeray, *Electrochem. Commun.*, **6** (2004) 1085-1091.
- [27] M.M. Thackeray, C.S. Johnson, J.T. Vaughey, N. Li, S.A. Hackney, *J. Mater. Chem.*, **15** (2005) 2257-2267.
- [28] M.M. Thackeray, S.-H. Kang, C.S. Johnson, J.T. Vaughey, R. Benedek, S.A. Hackney, *J. Mater. Chem.*, **17** (2007) 3112-3125.
- [29] N. Yabuuchi, K. Yoshii, S.-T. Myung, I. Nakai, S. Komaba, *J. Am. Chem. Soc.*, **133** (2011) 4404-4419.
- [30] J. Bareño, C.H. Lei, J.G. Wen, S.H. Kang, I. Petrov, D.P. Abraham, *Adv. Mater.*, **22** (2010) 1122-1127.
- [31] C.H. Lei, J.G. Wen, M. Sardela, J. Bareño, I. Petrov, S.-H. Kang, D.P. Abraham, *J. Mater. Sci.*, **44** (2009) 5579-5587.
- [32] A. Boulinau, L. Croguennec, C. Delmas, F. Weill, *Chem. Mater.*, **21** (2009) 4216-4222.
- [33] A. Boulinau, L. Croguennec, C. Delmas, F. Weill, *Solid State Ionics*, **180** (2010) 1652-1659.
- [34] R. Wang, X. He, L. He, F. Wang, R. Xiao, L. Gu, H. Li, L. Chen, *Adv. Energy Mater.*, **3** (2013) 1358-1367.
- [35] D.Y.W. Yu, K. Yanagida, *J. Electrochem. Soc.*, **158** (2011) A1015-A1022.
- [36] A.D. Robertson, P.G. Bruce, *Chem. Mater.*, **15** (2003) 1984-1992.
- [37] S.F. Amalraj, L. Burlaka, C.M. Julien, A. Mauger, D. Kovacheva, M. Talianker, B. Markovsky, D. Aurbach, *Electrochim. Acta*, **123** (2014) 395-404.
- [38] K.G. Gallagher, J.R. Croy, M. Balasubramanian, M. Bettge, D.P. Abraham, A.K. Burrell, M.M. Thackeray, *Electrochem. Commun.*, **33** (2013) 96-98.
- [39] D. Mohanty, J. Li, D.P. Abraham, A. Huq, E.A. Payzant, D.L. Wood, C. Daniel, *Chem. Mater.*, **26** (2014) 6272-6280.
- [40] M. Sathiya, A.M. Abakumov, D. Foix, G. Rouse, K. Ramesha, M. Saubanière, M.L. Doublet, H. Vezin, C.P. Laisa, A.S. Prakash, D. Gonbeau, G. VanTendeloo, J.M. Tarascon, *Nat. Mater.*, **14** (2015) 230-238.
- [41] J.R. Croy, D. Kim, M. Balasubramanian, K. Gallagher, S.-H. Kang, M.M. Thackeray, *J. Electrochem. Soc.*, **159** (2012) A781-A790.
- [42] D. Kim, J.R. Croy, M.M. Thackeray, *Electrochem. Commun.*, **36** (2013) 103-106.
- [43] M. Jiang, B. Key, Y.S. Meng, C.P. Grey, *Chem. Mater.*, **21** (2009) 2733-2745.
- [44] A. Manthiram, K. Chemelewski, E.-S. Lee, *Energ. Environ. Sci.*, **7** (2014) 1339.
- [45] N.P.W. Pieczonka, Z. Liu, P. Lu, K.L. Olson, J. Moote, B.R. Powell, J.-H. Kim, *J. Phys. Chem. C*, **117** (2013) 15947-15957.
- [46] W. Choi, A. Manthiram, *J. Electrochem. Soc.*, **153** (2006) A1760-A1764.
- [47] D. Lu, M. Xu, L. Zhou, A. Garsuch, B.L. Lucht, *J. Electrochem. Soc.*, **160** (2013) A3138-A3143.
- [48] M.X. Lin, L.B. Ben, Y. Sun, H. Wang, Z.Z. Yang, L. Gu, X.Q. Yu, X.Q. Yang, H.F. Zhao, R. Yu, M. Armand, X.J. Huang, *Chem. Mater.*, **27** (2015) 292-303.
- [49] S. Hwang, W. Chang, S.M. Kim, D. Su, D.H. Kim, J.Y. Lee, K.Y. Chung, E.A. Stach, *Chem. Mater.*, **26** (2014) 1084-1092.
- [50] S.-K. Jung, H. Gwon, J. Hong, K.-Y. Park, D.-H. Seo, H. Kim, J. Hyun, W. Yang, K. Kang, *Adv. Energy Mater.*, **4** (2014) 1300787.
- [51] A.K. Padhi, K.S. Nanjundaswamy, J.B. Goodenough, *J. Electrochem. Soc.*, **144** (1997) 1188-1194.
- [52] Z. Bakenov, I. Taniguchi, *Electrochem. Commun.*, **12** (2010) 75-78.
- [53] M. Gaberscek, R. Dominko, M. Bele, M. Remskar, D. Hanzel, J. Jamnik, *Solid State Ionics*, **176** (2005) 1801-1805.
- [54] V. Srinivasan, J. Newman, *J. Electrochem. Soc.*, **151** (2004) A1517-A1529.
- [55] A.S. Andersson, B. Kalska, L. Häggström, J.O. Thomas, *Solid State Ionics*, **130** (2000) 41-52.
- [56] C. Delmas, M. Maccario, L. Croguennec, F. Le Cras, F. Weill, *Nat. Mater.*, **7** (2008) 665-671.
- [57] W. Dreyer, J. Jamnik, C. Gulike, R. Huth, J. Moskon, M. Gaberscek, *Nat. Mater.*, **9** (2010) 448-453.
- [58] L.G.L. Gu, C.B. Zhu, H. Li, Y. Yu, C.L. Li, S. Tsukimoto, J. Maier, Y. Ikuhara, *J. Am. Chem. Soc.*, **133** (2011) 4661-4663.
- [59] C.B. Zhu, L. Gu, L.M. Suo, J. Popovic, H. Li, Y. Ikuhara, J. Maier, *Adv. Funct. Mater.*, **24** (2014) 312-318.
- [60] L. Suo, W. Han, X. Lu, L. Gu, Y.-S. Hu, H. Li, D. Chen, L. Chen, S. Tsukimoto, Y. Ikuhara, *Phys. Chem. Chem. Phys.*, **14** (2012) 5363-5367.
- [61] A.S. Arico, P. Bruce, B. Scrosati, J.-M. Tarascon, W. van Schalkwijk, *Nat. Mater.*, **4** (2005) 366-377.
- [62] K. Zaghib, M. Dontigny, A. Guerfi, P. Charest, I. Rodrigues, A. Mauger, C.M. Julien, *J. Power Sources*, **196** (2011) 3949-3954.
- [63] G.-N. Zhu, Y.-G. Wang, Y.-Y. Xia, *Energ. Environ. Sci.*, **5** (2012) 6652-6667.
- [64] L. Aldon, P. Kubiak, M. Womes, J.C. Jumas, J. Olivier-Fourcade, J.L. Tirado, J.I. Corredor, C. Pérez Vicente, *Chem. Mater.*, **16** (2004) 5721-5725.
- [65] C. Kim, N.S. Norberg, C.T. Alexander, R. Kostecki, J. Cabana, *Adv. Funct. Mater.*, **23** (2013) 1214-1222.
- [66] Z. Yang, J. Wang, Q. Zhang, D. Xiao, B. Xu, A. Zhang, Y. Yu, L. Gu, Y. Hu, H. Li, C. Nan, *Mater. Express*, **5** (2015) 457-462.
- [67] S.-W. Kim, D.-H. Seo, X. Ma, G. Ceder, K. Kang, *Advanced Energy Materials*, **2** (2012) 710-721.
- [68] V. Palomares, P. Serras, I. Villaluenga, K.B. Hueso, J. Carretero-Gonzalez, T. Rojo, *Energ. Environ. Sci.*, **5** (2012) 5884-5901.
- [69] M.D. Slater, D. Kim, E. Lee, C.S. Johnson, *Adv. Funct. Mater.*, **23** (2013) 947-958.
- [70] Y. Sun, L. Zhao, H. Pan, X. Lu, L. Gu, Y.-S. Hu, H. Li, M. Armand, Y. Ikuhara, L. Chen, X. Huang, *Nat. Commun.*, **4** (2013) 1870-1870.
- [71] X. Yu, H. Pan, W. Wan, C. Ma, J. Bai, Q. Meng, S.N. Ehrlich, Y.-S. Hu, X.-Q. Yang, *Nano Lett.*, **13** (2013) 4721-4727.
- [72] D.A. Muller, L.F. Kourkoutis, M. Murfitt, J.H. Song, H.Y. Hwang, J. Silcox, N. Dellby, O.L. Krivanek, *Science*, **319** (2008) 1073-1076.
- [73] I. MacLaren, Q.M. Ramasse, *Int. Mater. Rev.*, **59** (2014) 115-131.
- [74] Y. Wang, L. Mu, J. Liu, Z. Yang, X. Yu, L. Gu, Y.-S. Hu, H. Li, X.-Q. Yang, L. Chen, X. Huang, *Adv. Energy Mater.*, **5** (2015) 1501005.

Microscopic Analyses of Deformation Structures around Fatigue Crack Tips

Yoshimasa Takahashi

Department of Mechanical Engineering, Kansai University

The fatigue fracture of a material is caused by the nucleation and subsequent growth of a fatigue crack. These phenomena, whose dominant dimension is typically micron-scale order, proceed irreversibly under a cyclic load. Their micro-mechanisms, however, are not unique depending on various factors. The analysis of local deformation structures around the crack tip region is therefore important. The key issue is the development of a sample fabrication technique that preserves the native structures around the target tip region. The selection of an optimum microscopy compatible with the sample is also critical. In this review, a novel sample fabrication technique that allows the observation of deformation structures in the plane normal to the crack plane is introduced. Example cases that combine the proposed technique and ultra-high-voltage TEM/SEM-EBSD, particularly focusing on the effect of hydrogen atmosphere on crack growth mechanism, are also presented. The various information provided by these analyses, none of which can be obtained from conventional fractography, are shown to play vital roles in elucidating the micro-mechanism of fatigue crack growth.

Introduction

The fracture of a material can be induced not only by its ultimate tensile strength (UTS) but also by a smaller load if it is repetitively applied. Such a mode of fracture is known as *fatigue fracture*. The strength against fatigue fracture is generally expressed in terms of the relation between two parameters: applied stress (or strain) amplitude and fatigue life. The latter one, which is expressed by the number of cycles to failure (N_f), is determined by the summation of crack nucleation life (i.e. incubation period before the crack attains certain dimension) and the subsequent subcritical crack growth life. These phenomena proceed typically in micron-order scale, and their micro-mechanism can be affected by various factors such as material class, environment, loading mode, etc. It is therefore important (i) to analyze these phenomena from a microscopic viewpoint and (ii) to feedback the information for the modification and/or reconstruction of local deformation/fracture models. From an engineering viewpoint, such elaboration would, either directly or indirectly, contribute to the development of fatigue resistant materials, the reliability design of apparatus and the root cause analysis of failure accidents.

The author has focused on the application of novel electron microscopy techniques to the analyses of fatigue crack initiation/

growth mechanisms particularly in metallic materials. In this short review, a couple of case studies regarding fatigue crack growth (FCG) are specifically picked up, and the role of the recent electron microscopy techniques in relation to such cases is briefly presented. Note that the readers are also invited to consult the original research articles [1-5] for finding detailed explanation on the mechanisms not presented herein.

A novel method for crack tip observation by electron microscopy (case 1)

Fatigue crack growth (FCG) is caused by the accumulation of cyclic damage at the crack tip. In the case of ductile metals, it is brought about by the repetitive plastic blunting/resharpening (irreversible slip deformation) at the crack tip during each load cycle [6-8]. The analysis of FCG mechanism is most frequently done with the observation of fracture plane (which is called *fractography*) as the morphological features remained on the plane can provide important information about the local deformation behaviour. Such information alone, however, is not necessarily enough for clarifying the local slip mechanism. Although the slip steps formed around a crack tip on the specimen surface are sometimes analyzed, it may not be

appropriate because the slip mechanism on the surface may be different from that inside the material owing to the difference of constraint. A method that enables one to observe the slip behaviour in the cross section normal to the crack plane is therefore strongly desired.

Figure 1 schematically shows the new fabrication process of a microscopy sample that contains a fatigue crack tip. A rectangular plate containing the crack tip is cut out from a fatigued bulk specimen. The final stage of cutting should be implemented either with a low-speed precision saw or a wire electrical discharge machine (EDM), otherwise the original dislocation structure would be altered by the extra loading applied to the crack tip. The thickness of the plate is then reduced by milling its side faces with a Cross Section Polisher (SM-09010, JEOL). The remaining thickness of the plate should be about 20 to 30 μm , which is suited for the subsequent FIB process. Prior to FIB thinning, a patch layer (ca. $5 \times 5 \times 2 \mu\text{m}^3$) is locally deposited on the side faces to firmly connect the upper and lower foil parts. This effectively eliminates excess stress concentration at the crack tip. The sample would be destroyed by the magnetic force applied by the objective pole piece if the patch layer is not attached.

Figure 2 shows a TEM image of a fatigue crack tip introduced to a single-crystalline Fe–Si alloy under an inert atmosphere (helium, 0.58 MPa). The magnetism of the sample material enhances astigmatism and beam shift. Moreover, the relatively thick FIB-prepared foil yields significant amount of inelastically scattered electrons, leading to the severe degradation of TEM image. The observation was therefore conducted by using an ultra-high-voltage TEM equipped with an energy filter system (JEM-1300NEF, JEOL). A high acceleration voltage of 1250 kV was employed so that the beam shift was reduced and enough signal intensity was obtained. The energy filter was also utilized to obtain a clear image with zero-loss electrons. In Fig. 2, the fatigue crack propagated from left to right along the $\{110\}$ plane. Dense slip bands extending to the $[\bar{1}11]$ direction exist, and they reach as far as about 30 μm away from the crack. The absence of slip bands in the right hand area about the dotted line

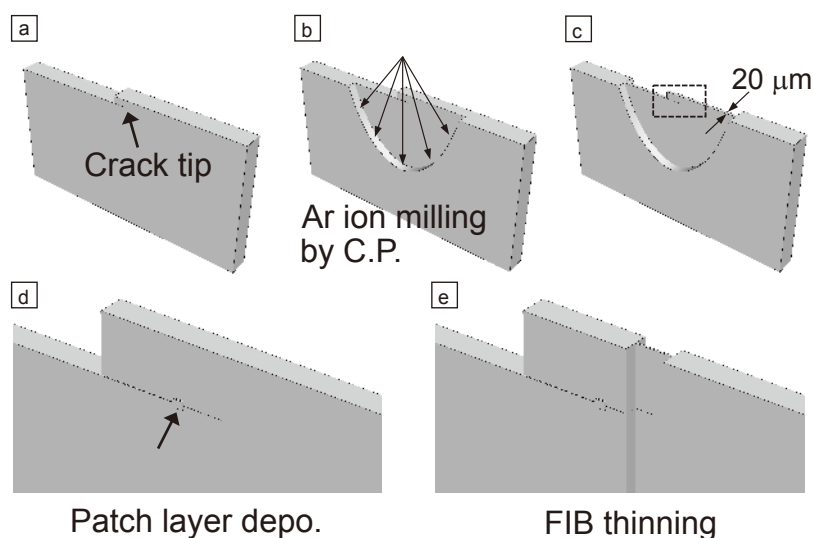
indicates that the slip bands have been emitted from the crack tip during the FCG. Below the densely slipped region, a dislocation wall structure, which is similar to the so-called “labyrinth” [9], is observed. The wall structure between each slip band is seen to keep its original form. This indicates that (i) the intense cyclic stress field ahead of the crack tip firstly induces the gradual formation of wall structure and (ii) the crack tip then rapidly advances by emitting the slip bands. The magnified image further reveals that the crack surface has a wavy outline and the subsurface region (ca. 0.5 μm from the surface) is severely deformed. The wave period is 0.2 to 0.3 μm , which corresponds to that of the striation pattern confirmed by the fractography (Fig. 2(c)). No microvoids or brittle microcracks exist in front of the crack tip. These observations suggest that the crack grows exclusively by stable (continuous) slip.

The combination of the novel sample fabrication method and the use of a high-performance TEM enables one to implement an ideal observation where both crack tip and its wake are well-preserved. It provides a lot of valuable information that cannot be revealed by simple fractography. Such an observation has not been achieved by the conventional method that utilizes an electro-polished foil sample and a normal microscope [10]. It should be noted that the method shown in Fig. 1 can be also applied to other types of observation, e.g. EBSD or scanning ion microscopy (SIM): the sample fabrication process is stopped at the C.P. stage (Fig. 1(b)) and the crack tip on the polished surface is observed. Then the same crack tip area is further thinned (Fig. 1(c) to (e)) and observed by TEM. The integration of these different analyses, each of which provides unique information, has significant advantages over the conventional methodology (see case 3).

Evaluation of hydrogen effect on Mode I crack growth (case 2)

The FCG property of metallic materials in gaseous hydrogen is one of the key strength indices that must be considered for the structural integrity of hydrogen energy apparatus. It has been

Fig. 1



Schematic illustration showing sample preparation procedure of a fatigue crack tip: (a) cutting of a plate containing the crack tip, (b) to (c) preliminary Ar ion milling by Cross Section Polisher, (d) deposition of a patch layer connecting upper-lower wakes of crack, (e) thinning by FIB. Note that mechanical polishing or chemical polishing are unsuited for the crack tip sample preparation.

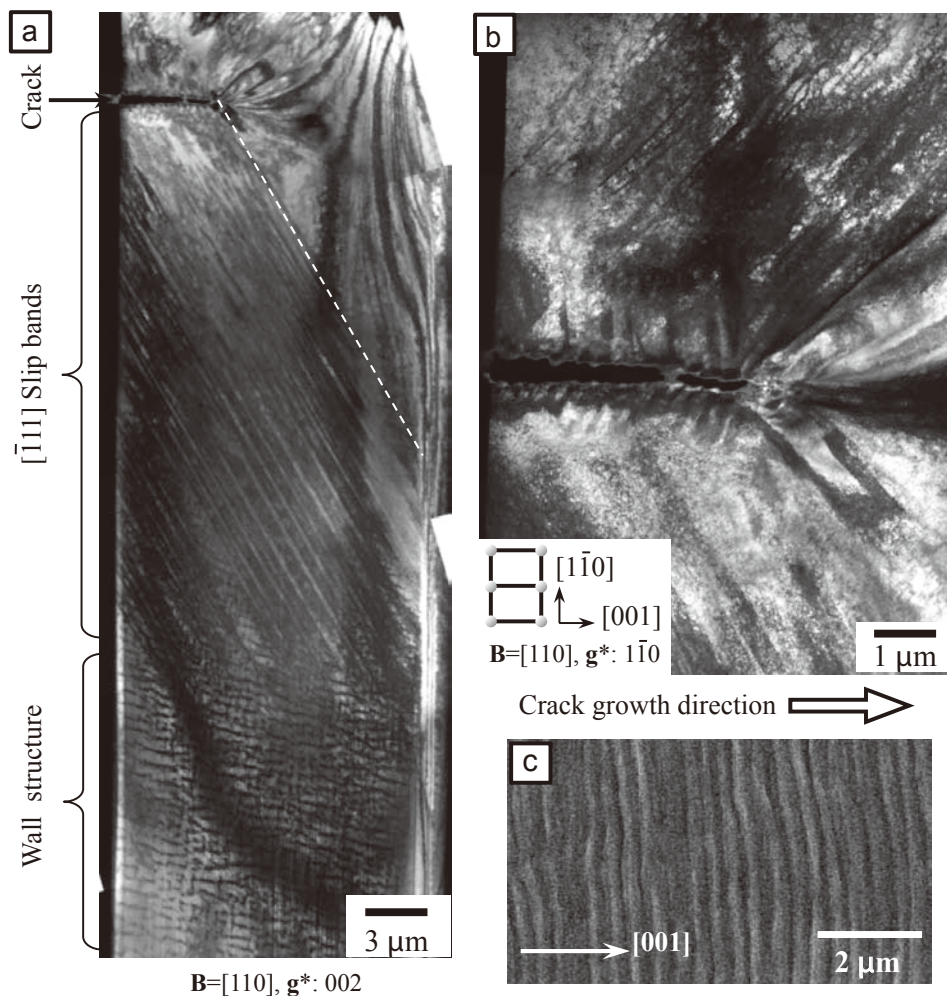
reported that the crack growth rate (i.e. the increment of crack length per load cycle) tends to be increased by the existence of hydrogen [11], which is one aspect of the so-called hydrogen embrittlement. The micro-mechanism of hydrogen-induced FCG acceleration in poly-crystalline metals is inevitably complex because grain boundary (GB) cohesion and/or crack tip slip can be affected by hydrogen. The former, which is known as hydrogen-induced GB decohesion, is considered to be an important mechanism in high-strength engineering alloys [12]. On the other hand, the basic mechanism regarding the effect of hydrogen on crack tip slip remains rather unclear owing partly to the complexities arising from slip-GB interaction [13]. In order to investigate the effect of hydrogen on crack tip slip in detail, a single-crystalline material can be preferably used. Here, a fatigue crack that propagates normal to the load axis (i.e. Mode I crack) is introduced into a Fe-Si single-crystal under a hydrogen atmosphere, and the crack tip slip is compared with that of the case 1.

Figure 3 shows the cross-sectional TEM images of a fatigue crack introduced along the $\{110\}$ plane (hydrogen, 0.58 MPa). The growth rate of this crack is ca. four times faster than that shown in Fig. 2 although the applied ΔK magnitude ($21 \text{ MPam}^{1/2}$) is the same. Slip bands are seen to be emitted from

the crack along the $[\bar{1}11]$ direction. The distribution of the slip bands is rather concentrated within about $5 \mu\text{m}$ from the crack; it is sparse in the remote region. The outline of the upper/lower crack wake coincides well; no hill-hollow pair as seen in Fig. 2 is formed. No microvoids or brittle microcracks exist in front of the crack tip. The labyrinth-like dislocation wall structure is not evident, indicating that the crack tip quickly approached this region before walls were fully developed.

The above result, at first sight, is incomprehensible as the amount of slip deformation directly associated with the FCG appears to be much smaller in hydrogen case despite the growth rate is much faster; the positive correlation between plastic zone size around a crack tip and crack growth rate, in terms of the conventional continuum mechanics, is ineffective. A supplemental experiment further confirmed that hydrogen-induced quasi-cleavage (as found along the $\{100\}$ plane) does not exist along the $\{110\}$ plane [3]. The anomalously fast FCG observed here then needs to be interpreted solely by the slip concentration at the crack tip. Tabata et al. observed the effect of hydrogen atmosphere on the crack growth behavior in a BCC Fe foil by using a straining holder operated inside an environmental TEM [14]. It was found that ductile fracture was facilitated by the localization of plastic deformation around the crack tip when

Fig. 2



TEM image of a mode I fatigue crack tip: (a) wide area view, (b) magnification of crack tip, (c) SEM image of fracture plane (fractography). Material: single crystalline Fe-3.2%Si alloy, test environment: helium gas (0.58 MPa/R.T.), stress amplitude: 280 MPa, stress ratio: 0.05, frequency: 1 Hz, $\Delta K = 21 \text{ MPam}^{1/2}$, $da/dN = 0.25 \mu\text{m}/\text{cycle}$, $V_{\text{acc}} = 1250 \text{ kV}$, bright field/zero-loss image.

hydrogen was introduced. The observation shown here explicitly indicates that such a slip localization effect is also present around a fatigue crack in a bulk metal where constraint against out-of-plane slip is significant. The concentration of solute hydrogen is known to be dependent on hydrostatic pressure [15]. The existence of solute hydrogen is also shown to reduce dislocation-dislocation interaction through the modification of elastic stress field [16]. These effects may explain a scenario that the high concentration of hydrogen and the resulting high mobility of dislocations promote slip localization at the crack tip and hence large advancement per crack opening displacement (COD) is generated. The detail of this mechanism is discussed in ref. [3].

Evaluation of hydrogen effect on oblique crack growth (case 3)

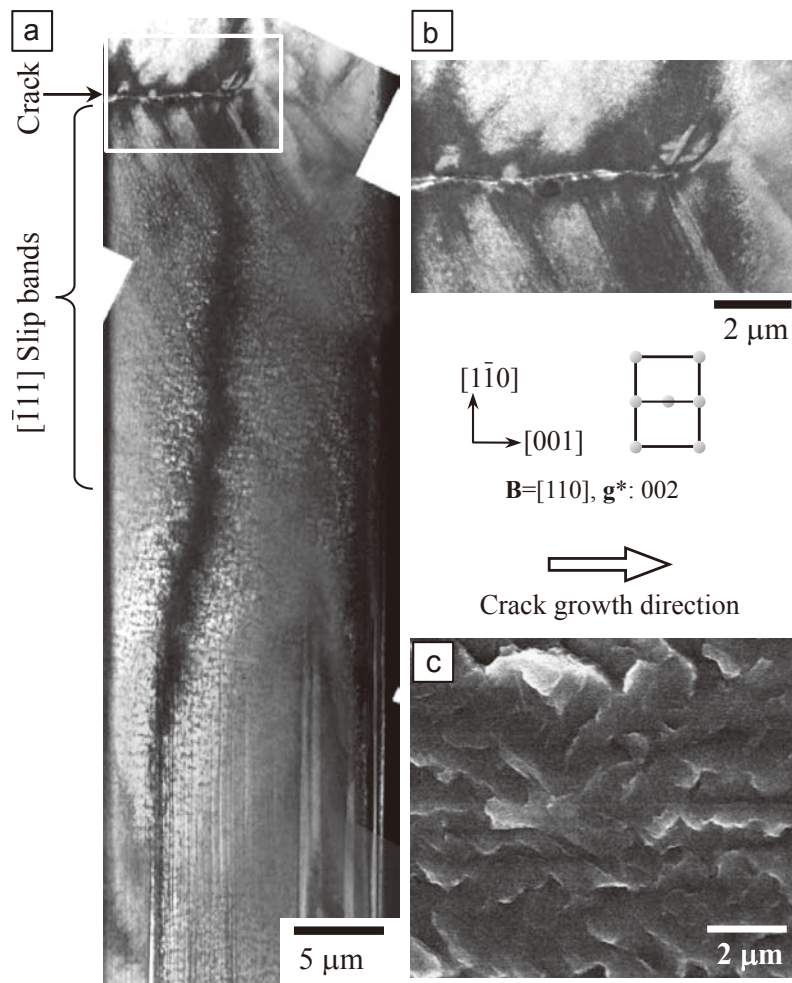
In the previous section, a Mode I type FCG controlled by symmetric slip about the crack plane (i.e. principal stress plane) was focused. In contrast, FCG tends to be strongly influenced by crystallographic orientation just after initiation event: the growth direction is then likely to be oblique to the principal stress plane. The mechanism of such a mixed-mode FCG, in terms of the relation between intense crack tip shear stress and asymmetric

slip about the principal stress plane, is not clear. In this section, detailed observation of the dislocation structures around an oblique fatigue crack in Fe-Si alloy is conducted. The effect of hydrogen on the FCG mechanism is also investigated.

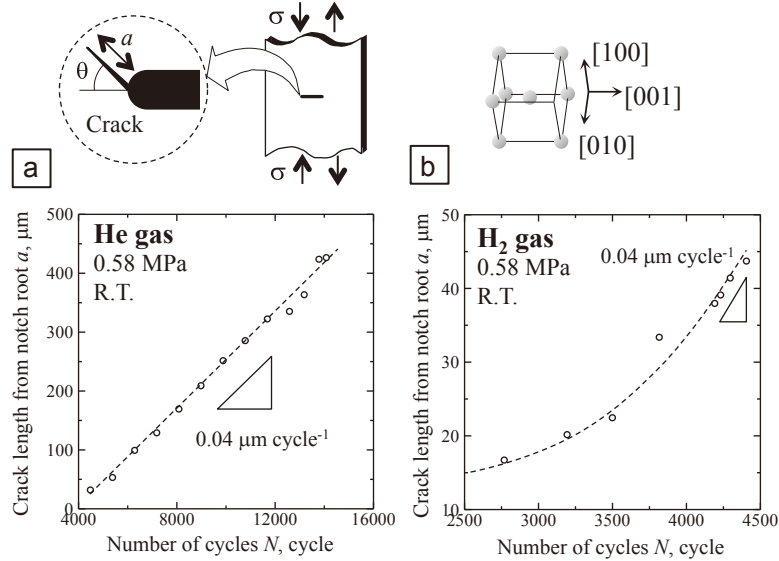
The fatigue specimen and test method are same as those used in the previous cases: a single-crystalline Fe-Si plate specimen with a center notch is uniaxially fatigued under helium/hydrogen atmosphere, and an oblique crack is initiated from the notch root. The relation between the fatigue cycles (N) and the crack length measured from the notch root (a) is shown in Fig. 4. In helium, crack growth rate, da/dN , is constant although a (and hence ΔK) increases. Such a growth property is different from a normal crack that obeys the fracture mechanics law where da/dN monotonically increases with ΔK . In hydrogen, on the other hand, the growth property is normal. Here, the crack tip region fatigued in helium/hydrogen is compared at the same da/dN ($\approx 0.04 \mu\text{m}/\text{cycle}$).

Figures 5 and 6 show the inverse pole figure (IPF) maps of the crack tip region fatigued in helium. Figure 6 is the magnified view of Fig. 5. These observations (JSM-7001F, JEOL) were conducted after a side face was milled; see Fig. 1(b). At low magnification (Fig. 5), the crack appears to grow straight. The angle of FCG ($\approx 47^\circ$) is slightly less than the angle of the

Fig. 3



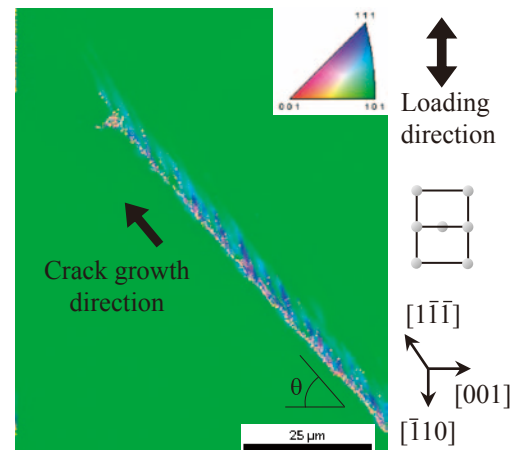
TEM image of a mode I fatigue crack tip: (a) wide area view, (b) magnification of crack tip, (c) SEM image of fracture plane (fractography). Material: single crystalline Fe-3.2%Si alloy, test environment: hydrogen gas (0.58 MPa/R.T.), stress amplitude: 280 MPa, stress ratio: 0.05, frequency: 1 Hz, $\Delta K = 21 \text{ MPa}\sqrt{\text{m}}^{1/2}$, $da/dN = 0.25 \mu\text{m}/\text{cycle}$, $V_{\text{acc}} = 1250 \text{ kV}$, bright field/zero-loss image.

Fig. 4


Comparison of growth properties of oblique fatigue cracks in different environments: (a) in helium gas, (b) in hydrogen gas. Material: single crystalline Fe-3.2%Si alloy, stress amplitude: 280 MPa, stress ratio: 0.05, frequency: 1 Hz.

$[1\bar{1}\bar{1}]$ slip direction (55°). Periodic array of misoriented cells is seen along the right side of the crack wake. The dimension of the cellular region, which can be regarded as the magnitude of the stress (strain) field exerted by the crack tip, is about $5 \mu\text{m}$ irrespective of the position along the crack. This corresponds to the *apparently* constant da/dN shown in Fig. 4(a). At high magnification (Fig. 6), the cellular region is found to be composed of fine elongated cells. The cell length is relatively small ($1 \mu\text{m}$) in the close vicinity of the crack, while relatively large (2 to $3 \mu\text{m}$) in the remote region. The pixels with low image quality (IQ) are seen at cell boundaries, indicating that the density of geometrically-necessary dislocations (GNDs) is significantly high at these boundaries. Since no eminent orientation change is seen in Fig. 6(a), the crystal in each cell is rotated around the $[110]$ axis. The rotation direction is clockwise as shown by the cubic symbols.

Figure 7 shows a TEM image of the crack tip region (bright field zero-loss image). This observation was conducted after the crack tip region was further thinned by FIB (JIB-4500, JEOL) as shown in Fig. 1(e). Note that the fine parallel lines formed along the $[\bar{1}\bar{1}\bar{1}]$ direction are flaws introduced by FIB. Various dislocation structures are seen around the crack tip. In the region denoted as “A”, a ladder-like structure, typically found in persistent slip bands (PSBs), is seen. On the upper side of the crack, cells elongated along the primary slip direction (i.e. $[1\bar{1}\bar{1}]$) exist and form a thick “cell band”. The cell band extends about $10 \mu\text{m}$ ahead of the crack tip. On the other side of the crack, few cells are seen. It is therefore postulated that the formation of the cells is firstly induced by the strong cyclic shear stress ahead of the crack tip and then the crack propagates along the boundary between cells and matrix. A small branched crack also appears along a cell, but this cell is probably formed by the activation of a conjugate slip system. In the region B, vein structure, which is formed by the primary edge dipoles, is seen. In region C, labyrinth structure is formed. These wall structures, respectively, are reported to be formed under small to moderate strain amplitude and relatively large strain amplitude [9]. Since the orientation difference between these structures and dislocation

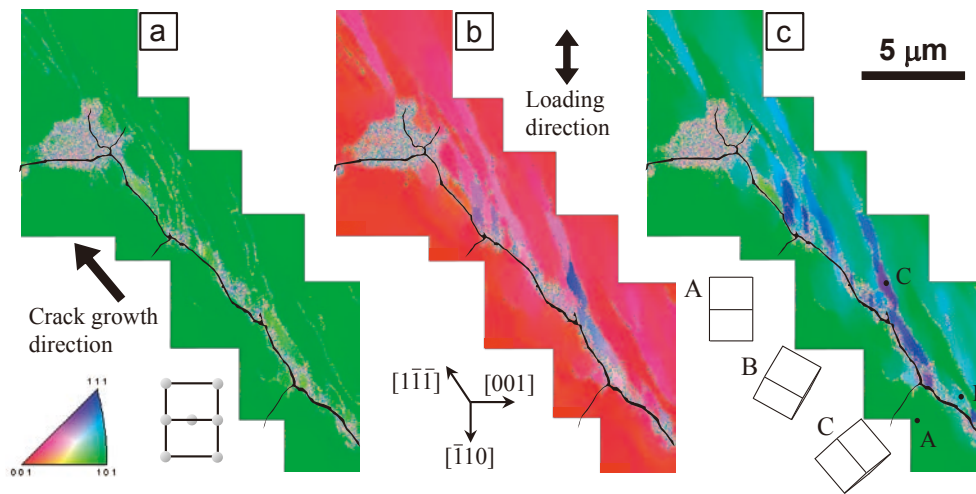
Fig. 5


IPF map around the near-tip region of an oblique fatigue crack. Material: single crystalline Fe-3.2%Si alloy, test environment: helium gas (0.58 MPa/R.T.), $\Delta K = 15.6 \text{ MPa}\sqrt{\text{m}}$, $da/dN = 0.04 \mu\text{m}/\text{cycle}$, SEM acceleration: 25 kV.

free matrix is very little, they cannot be identified in the IPF map data. These wall structures have been separately characterized by using different specimens subjected to different level of strain amplitude. On the other hand, the hierarchical distribution of these structures around a mixed-mode fatigue crack tip has not been reported. The distribution of dislocation structures revealed here, each of which reflects the local strain history, provides critical information regarding the crack growth mechanism (see ref. [4]).

Figure 8 shows the IPF map and TEM image of an oblique crack tip introduced in hydrogen. No dislocation structures having large orientation difference (such as cells) are present as shown in the IPF map. Vein and labyrinth are both seen in the TEM image. These wall structures, however, are not clear in the vicinity of the crack. This indicates that the wall structures are

Fig. 6



Magnified images of Fig. 5. (a), (b) and (c) respectively show crystal orientation seen from $[110]$, $[001]$ and $[\bar{1}10]$ directions.

changed by the dislocations emitted from the crack tip in the conjugate slip directions (i.e. $[1\bar{1}\bar{1}]/[\bar{1}11]$). It is then postulated that the present oblique FCG is attributed to the crack tip opening/closing caused by the alternate activation of two slip systems (slip-off mechanism).

The comparative observations shown here unambiguously reveal that the major difference of the FCG mechanism in helium and hydrogen atmospheres is attributed to the existence/inexistence of a cell structure. The formation of a cell structure indicates that cross slip plays an important role in cyclic deformation in helium. An in situ dislocation observation also confirmed that the operation of cross slip was restricted by the existence of solute hydrogen [17]. In hydrogen, therefore, cross slip and cell formation are restricted, and the FCG mechanism eventually changes to the normal slip-off type. Note that the ΔK value of the crack in hydrogen is smaller than that in helium while da/dN values are the same in both cases. In other words, the slip-off mechanism in hydrogen has lower resistance than the cell-mediated mechanism in helium, i.e. the former mode is more hazardous than the latter one.

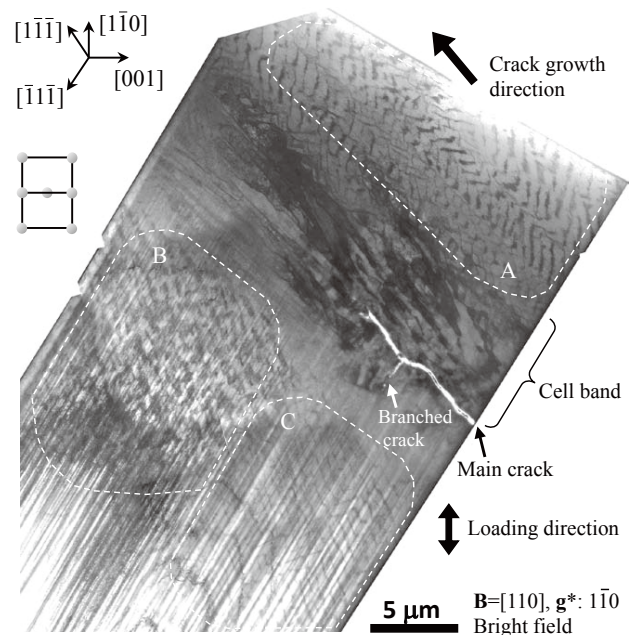
Summary

The analytical methodology of deformation structure around a fatigue crack tip and its applications are reviewed. EBSD is suited for the wide-area mapping of structures having clear orientation difference (cells), not suited for the analysis of structures having little orientation difference (dislocation walls). The diffraction contrast obtained by TEM, on the other hand, has high sensitivity to orientation difference, but a wide-area observation by TEM is difficult. By systematically combining these methods, a multi scale analysis that cannot be done by simple fractography is achieved.

Acknowledgments

The author is grateful to kind support by coworkers (Drs. H. Noguchi, K. Higashida, M. Tanaka, J. Sakamoto and Mr.

Fig. 7



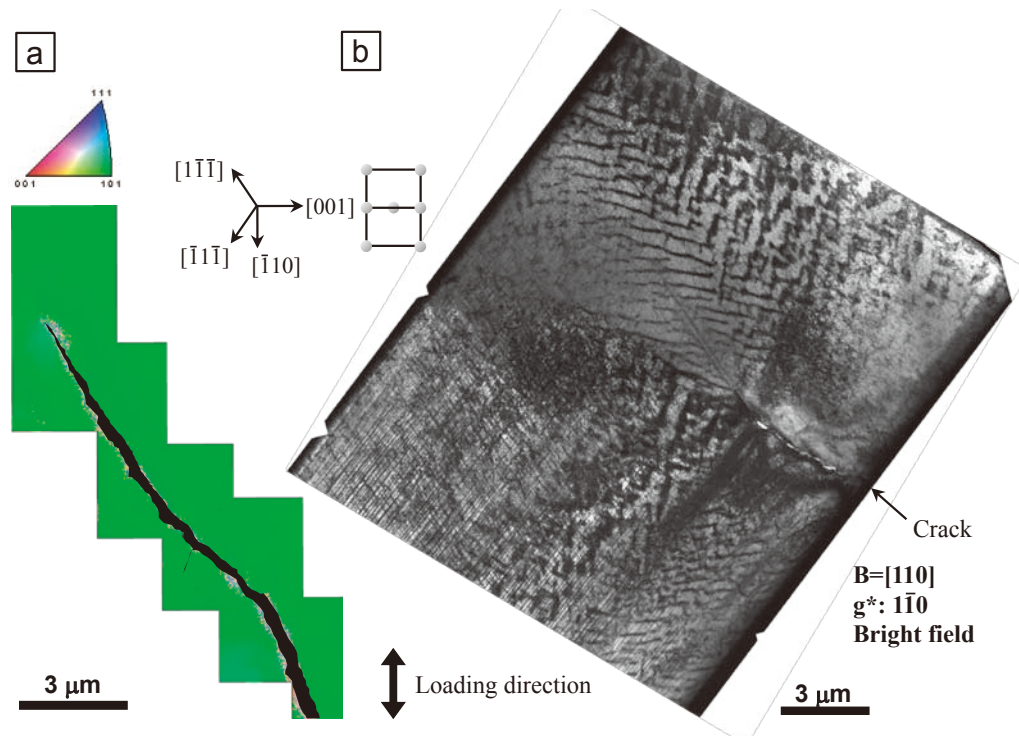
TEM image of an oblique fatigue crack tip. The thin foil sample used here was made after the EBSD observations shown in Figs. 5 and 6 were done. $V_{acc} = 1250$ kV, bright field/zero-loss image.

K. Yamaguchi). Cooperation by the Research Laboratory for HVEM (Kyushu University) is also greatly acknowledged. The research was conducted under the auspices of “Fundamental Research Project on Advanced Hydrogen Science” funded by New Energy and Industrial Technology Development Organization (NEDO), Japan.

References

[1] Takahashi Y., Tanaka M., Higashida K., Noguchi H., High-

Fig. 8



(a) IPF map and (b) TEM image of an oblique fatigue crack tip. Material: single crystalline Fe-3.2%Si alloy, test environment: hydrogen gas (0.58 MPa/R.T.), $\Delta K = 13.4 \text{ MPam}^{1/2}$, $da/dN = 0.04 \text{ }\mu\text{m/cycle}$, SEM acceleration: 25 kV, TEM acceleration: 1250 kV (bright field/zero-loss image).

voltage electron-microscopic observation of cyclic slip behavior around a fatigue crack tip in an iron alloy, *Scripta Materialia*, **60** (2009) 717-720.

- [2] Takahashi Y., Tanaka M., Higashida K., Noguchi H., Hydrogen-induced slip localization around a quasi-brittle fatigue crack observed by high-voltage electron microscopy, *Scripta Materialia*, **61** (2009) 145-148.
- [3] Takahashi Y., Tanaka M., Higashida K., Yamaguchi K., Noguchi H., An intrinsic effect of hydrogen on cyclic slip deformation around a {110} fatigue crack in Fe-3.2 wt.% Si alloy, *Acta Materialia*, **58** (2010) 1972-1981.
- [4] Takahashi Y., Sakamoto J., Tanaka M., Higashida K., Noguchi H., Characterization of dislocation structures around a mixed-mode fatigue crack tip in a single-crystalline iron-silicon alloy, *Scripta Materialia*, **64** (2011) 157-160.
- [5] Takahashi Y., Sakamoto J., Tanaka M., Higashida K., Noguchi H., Effect of hydrogen on dislocation structures around a mixed-mode fatigue crack tip in a single-crystalline iron-silicon alloy, *Scripta Materialia*, **64** (2011) 721-724.
- [6] Laird C., The influence of metallurgical structure on the mechanism of fatigue crack propagation, ASTM STP415, Philadelphia, Pennsylvania, 1967, pp. 131-180.
- [7] Sugeta A., Uematsu Y., Tanimoto K., Ueminami K., Hashimoto A., Jono M., AFM observation of slip deformation near Model I fatigue crack tip and quantitative analysis using image processing technique, Transactions of the Japan Society of Mechanical Engineers Series A, **66** (2000) 1157-1164 (in Japanese).
- [8] Oda Y., Furuya Y., Noguchi H., Higashida K., AFM and SEM observation on mechanism of fatigue crack growth in an Fe-Si single crystal, *International Journal of Fracture*, **113** (2002) 213-231.
- [9] Laird C., Charsley P., Mughrabi H., Low energy dislocation structures produced by cyclic deformation, *Materials Science and Engineering*, **81** (1986) 433-450.
- [10] Katagiri K., Awatani J., Koyanagi K., Onishi Y., Tsuji M., Dislocation structures adjacent to fatigue crack tips propagating at high rates in copper and 70/30 brass, *Metallurgical transactions*, **11A** (1980) 2029-2032.
- [11] For example: Oda Y., Noguchi H., Observation of hydrogen effects on fatigue crack growth behaviour in an 18Cr-8Ni austenitic stainless steel, *International Journal of Fracture*, **132** (2005) 99-113.
- [12] Tanaka K., Hojo M., Nakai Y., Plastic deformation around a fatigue crack near threshold in 3%Si-Fe, *Materials Science and Engineering*, **55** (1982) 85-96.
- [13] Shewmon P.G., Grain boundary cracking, *Metallurgical and Materials Transactions*, **29B** (1998) 509-518.
- [14] Tabata T., Birnbaum H.K., Direct observations of hydrogen enhanced crack propagation in iron, *Scripta Metallurgica*, **18** (1984) 231-236.
- [15] Morlet J.G., Johnson H.H., Troiano A.R., A new concept of hydrogen embrittlement in steels, *Journal of Iron and Steel Institute*, **189** (1958) 37-44.
- [16] Birnbaum H.K., Sofronis P., Hydrogen-enhanced localized plasticity—a mechanism for hydrogen-related fracture, *Materials Science and Engineering A*, **176** (1994) 191-202.
- [17] Ferreira P.J., Robertson I.M., Birnbaum H.K., Hydrogen effects on the interaction between dislocations, *Acta Materialia*, **46** (1998) 1749-1757.

Rapid Screening and Quantification of Synthetic Cannabinoids with DART-MS and NMR Spectroscopy

Michael A. Marino,¹ Robert B. Cody,² A. John Dane,² Ling Huang,¹

¹ Chemistry Department, Hofstra University

² JEOL USA Inc.

The usage of herbal incenses intentionally doped with synthetic cannabinoids has caused an increase in medical incidents and has triggered legislation to ban these products throughout the world. Law enforcement agencies are experiencing sample backlogs due to the variety of the products and the addition of new and still-legal compounds. In our study, proton Nuclear Magnetic Resonance spectroscopy (NMR) was employed to promptly identify the synthetic cannabinoids after their rapid, direct detection on the herbs and in the powders by Direct Analysis in Real Time-Mass Spectrometry (DART-MS). Compared to conventional lengthy pre-NMR sample clean-up and purification, a simple sample preparation protocol was employed on 50 mg of herbal product samples for quick NMR detection. The combined DART-MS and NMR methods can be used to quickly screen synthetic cannabinoids in powder and herbal samples. Subsequently rapid quantification of cannabinoids can be achieved with short proton-NMR scans when an internal standard, maleic acid, is employed.

Introduction

Since 2006, synthetic cannabinoids such as JWH-018 (**Fig. 1** and **Fig. 2a**) have been reportedly mixed with natural herbs and sold as cannabis substitutes all over the world [1]. Smoking these synthetic cannabimimetic compounds in their pure form, and more commonly in herbal blends, has produced adverse effects in users such as anxiety attacks, vomiting and psychotic episodes which resulted in increased emergency room visits. Legislations passed in many countries attempted to ban these compounds with limited effect. Drug users are often inhaling synthetic compounds that are misrepresented with varying concentrations with ever-changing identity. New generations of these so called “Spice” products are constantly being released into the international market and are continuing to cause harm [2]. As a result, it has become urgent for forensic labs to promptly detect, identify, and quantify synthetic cannabinoids in their original powder form and in other consumer products, with minimal sample preparation and clean-up steps.

Many current methods include a combination of chromatographic separation (TLC, LC, and GC) and spectroscopic investigation (FTIR, UV-Vis, NMR and MS). The sample preparation also involves lengthy and expensive steps in order to get pure and clean compounds or mixtures with minimal herbal matrix. We proposed to use DART-MS and NMR to treat with virtually

no or little sample preparation while taking advantage of the spectral separation power to rapidly identify and quantify (with proton-NMR) cannabinoids [3].

Direct Analysis in Real Time-Mass Spectrometry (DART-MS) has been previously used to rapidly detect narcotics with essentially no sample preparation and ultra-fast speed analysis under atmospheric conditions [4]. Uchiyama *et al* [5-7] have also utilized DART-MS as one of their confirmatory methods for several purified JWH- compounds extracted and separated from herbal blends. DART ionization occurs by introducing the sample (powder solids and liquids) into the gas stream, sometimes via a coated glass rod [4]. Peaks corresponding to protonated molecules are then detected within seconds by a high resolution Time-of-Flight Mass Spectrometer (TOF-MS). Using exact mass information, isotope peaks and fragmentation data under different cone voltage conditions, a compound of interest can be identified within minutes with minimal interference from the background. More recently, following rapid DART ionization, Musah *et al.* have successfully demonstrated how the fragmentation from the DART mass spectra can indicate the presence of specific structural features in synthetic cannabinoids [8, 9].

DART-MS, however, is not always able to differentiate between two isomers that have identical fragments. Thus it was recommended as a reliable screening tool for forensic

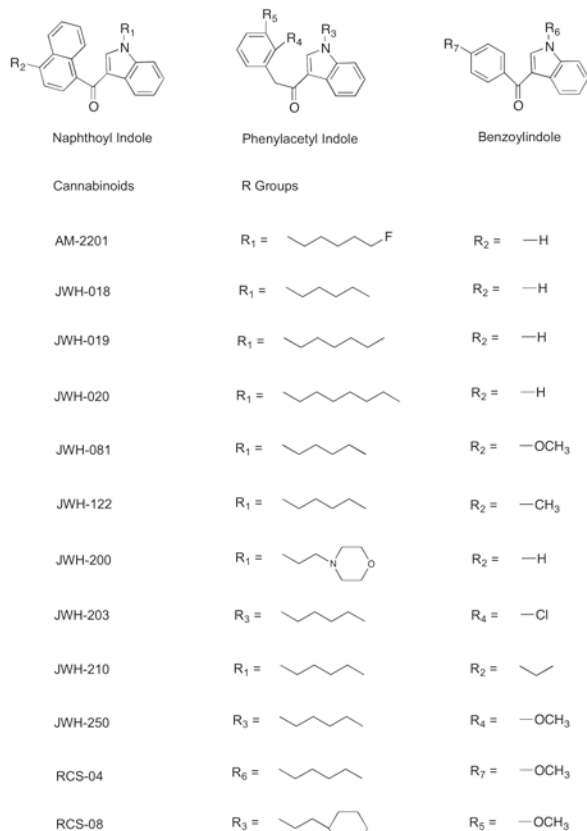
drug analysis [4]. Although time-dependent desorption can occur for compounds with differing volatility, the lack of a chromatographic separation method can in some cases limit the utility of the DART method. Additionally, when more than two synthetic components of varying concentrations are present in the herbal products, it may be difficult to interpret the overlapping fragment-ion mass spectra, thus resulting in the trace components possibly being overlooked. Consequently, additional confirmatory methods such as NMR can enhance the positive identification of positional isomers and all components

in a mixture.

NMR has been extensively used to derive the structures of purified synthetic cannabinoids [1, 4, 5, 10, 11]. JWH-series and AM-series compounds (Fig. 1) have distinctive peaks in the proton NMR aromatic regions (6.5-9 ppm) as well as around 4 ppm, with little to no interference from natural components from the herbal base. Because of the high abundance of H-1, only a minimal amount of cannabinoid analyte is necessary to reach very low detection limits with a small amount of herbs (~100 mg or less). To render the dosage effective, usually the concentration of the synthetic cannabinoid ranges from 1-40 mg/g of herb (10). When the synthetic compound is extracted from the surface of the herbs into an NMR solvent, the final concentration range is from 0.1-10 mg/mL, which exceeds the NMR detection limit (~1 µg/mL) by several orders of magnitude.

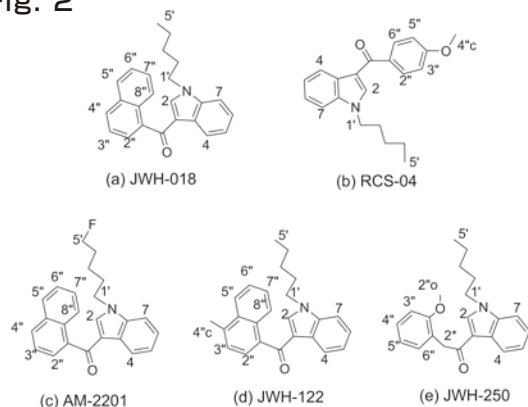
Conventional structural elucidation by NMR has required cumbersome sample preparation steps to collect enough purified compounds (5 mg or more) and lengthy NMR experiments with H1-NMR, C13-NMR, DEPT, COSY, HMQC and HMBC that can last several days [1, 6, 10]. To ensure clean spectra, the cannabinoid samples had to be extracted from the herbal matrices and separated on TLC plates or chromatographic columns multiple times to get enough pure compounds [1, 5]. Our NMR sample preparation method is designed as a simplified protocol to dramatically reduce the time and sample size needed to positively identify cannabinoids in herbal products. The combination of rapid DART-MS and NMR can provide concrete cannabinoid structural information with no ambiguity, which can be a useful alternative, or complement, to conventional GC-MS and LC-MS methods. With the addition of an internal standard, quantitative proton-NMR can be completed for quantification of cannabinoids.

Fig. 1



Structures of synthetic indole cannabinoids 154 x 223 mm (300 x 300 DPI)

Fig. 2



Synthetic cannabinoid structures with numbering scheme: (a) JWH-018, (b) RCS-04, (c) AM-2201, (d) JWH-122, (e) JWH-250, 138 x 107 mm (300 x 300 DPI)

Experimental

Materials:

The standard cannabinoids were purchased from two sources. Primary standards (see **Table 2**) with good quality control were purchased from Cayman Chemical (Ann Arbor, MI, USA) and all of the other “standards” (stored in round plastic vials like the one in **Fig. 3a**) were purchased online from Mountain Industry (California, USA). The Mountain Industry powders were found to be of low quality with mixtures and/or mislabeled compounds identified within these samples (**Table 1** and **Table 2**). This company was a major online distributor for other online sellers of “Spice” products. The structures of the standard cannabinoids and the ones detected in our herbal samples are listed in Figs 1 and 2. The sample packages are displayed in **Fig. 3** along with a microscopic image of an herb and a plastic vial containing one of the Mountain Industry powders. **Figure 3b** shows a close-up image of the leafy material in a product called “Moon Spice”.

All of the standards were stored in a desiccator at 4 C. Deuterated chloroform (CDCl₃) and maleic acid was purchased from Sigma Aldrich (St. Louis, MO, USA). Several pure herbs such as damiana, mullein, and mugwort (from Amazon.com) were used to serve as a background or as blank samples for MS and NMR analyses.

DART-MS methods:

An AccuTOF-DART (JEOL USA, Inc., Peabody, MA, USA) time-of-flight mass spectrometer (TOF-MS) was used for all exact mass measurements (resolving power = 6000, FWHM definition). A mass spectrum of polyethylene glycol (PEG), with an average molecular weight of 600 g/mol, was included in each

Table 1

| Label | DART-MS | Proton NMR |
|---|----------------------------|----------------------------|
| "Mountain Industry" Powder Samples | | |
| AM-1221 | AM-2201 (with impurity) | AM-2201 (with impurity) |
| AM-2201 | JWH-019 | JWH-019 |
| JWH-122 | JWH-200 | JWH-200 |
| JWH-203 | As labeled with impurities | As labeled with impurities |
| Herbs | | |
| Barely Legal | AM-2201 RCS-04 | AM-2201 RCS-04 |
| Melon Code Black | JWH-122 JWH-203 | JWH-122 JWH-203 |
| Moon Spice | RCS-04 JWH-018 | RCS-04 JWH-018 |
| Sweet Leaf | JWH-210 JWH-122 JWH-250 | JWH-210 JWH-122 JWH-250 |
| Apple Jacked | RCS-04 AM-2201 | RCS-04 AM-2201 |
| Chillin XXX | RCS-08 AM-2201 JWH-210 | RCS-08 AM-2201 JWH-210 |
| Funky Monkey | JWH-122 | JWH-122 |
| Ion Lab | RCS-04 AM-2201 | RCS-04 AM-2201 |
| Mr. Nice Guy | AM-2201 JWH-122 | AM-2201 JWH-122 |
| 4 Winds | No Cannabinoid | No Cannabinoid |

Identification results for synthetic cannabinoids and herbs.

data set as a reference standard for the exact mass measurements. The AccuTOF atmospheric pressure interface was operated with the potential settings for Orifice 1 = 20 V, Orifice 2 = 5 V, and Ring Lens = 3 V. At these potentials, little to no collision-induced dissociation (CID) occurs and the resulting mass spectra are dominated by protonated molecules ($[M+H]^+$). Fragmentation spectra were obtained via in-source CID with Orifice 1 voltages at 30, 60, 90 and 120 V, respectively. The RF ion guide voltage was set to 600 V to allow the detection of ions greater than m/z 60. The DART-SVP ion source (IonSense Inc., Saugus, MA) was operated with a helium gas heater temperature of 300°C and exit grid voltage of 250 V. TSSPro3 software (Shrader Analytical, Detroit, MI) and Mass Spec Tools software (ChemSW Inc., Fairfield, CA) were used for data processing and data interpretation. For standard analysis, the powdered sample was introduced directly into the DART stream on the closed end of a melting point tube. During spice analysis, three random pieces of plant material were selected from a given sample bag. Each sample was then held in the DART gas stream with forceps for 10 seconds. Afterwards, PEG 600 was measured within the same data file for the exact mass calibration. Prior to DART-MS analyses of the herbal blends with cannabinoids, the base herbs were also tested, which yielded no molecular ion peaks comparable to the synthetic cannabinoids. Most of the synthetic compounds possess molecular weights higher than 320 g/mol, and they produce strong, dominating, and distinctive peaks corresponding to protonated molecules.

NMR procedures:

¹H-NMR spectra were obtained on a JEOL JNM-ECS 400 MHz spectrometer (Peabody, MA, USA) with a JEOL 40th 5AT/FG2 5-mm proton/multi-frequency auto-tunable broadband probe and with CDCl₃ as the solvent. Chemical shifts were

Table 2

| Label | MI "AM-1221" | Cayman AM-2201 | MI "AM-2201" | Reference JWH-018 (1,7) | MI "JWH-081" | Cayman JWH-122 | MI "JWH-122" | MI "JWH-203" | Cayman JWH-210 | MI "JWH-250" | Cayman RCS-04 |
|---------------|----------------|----------------|---------------|-------------------------|--------------|----------------|----------------|--------------|----------------|--------------|---------------|
| Actual | AM-2201 | A.L. | JWH-19 | JWH-018 | A.L. | A.L. | JWH-200 | A.L. | A.L. | A.L. | A.L. |
| H-2 | 7.30-7.41 | 7.34 S | 7.34 S | 7.34 | 7.35 M | 7.32-7.38 | 7.44 M | 7.87 S | 7.36 M | 7.86 S | 7.57 S |
| H-4 | 8.49 M | 8.49 M | 8.48 M | 8.49 | 8.46 M | 8.48 M | 8.52 M | 8.39 M | 8.48 M | 8.40 M | 8.36 M |
| H-5 | 7.34-7.40 | 7.34-7.37 | 7.35 M | 7.33-7.39 | 7.35 M | 7.34 | 7.36 M | 7.28 M | 7.32-7.40 | 7.25 M | 7.28 M |
| H-6 | 7.34-7.40 | 7.34-7.37 | 7.33 M | 7.33-7.39 | 7.31-7.41 | 7.32-7.38 | 7.33-7.42 | 7.33 M | 7.32-7.40 | 7.25-7.32 | 7.31 M |
| H-7 | 7.34-7.40 | 7.34-7.37 | 7.37 M | 7.33-7.39 | 7.31-7.41 | 7.32-7.38 | 7.33-7.42 | 7.36 M | 7.32-7.40 | 7.25-7.32 | 7.38 M |
| H-2" | 7.65 M | 7.65 D | 7.65 dD | 7.64 | 7.65 D | 7.55 M | 7.65 D | - | 7.55 M | - | 7.84 D |
| H-3" | 7.51 M | 7.50 M | 7.50 M | 7.51 | 6.82 D | 7.36 M | 7.51 M | 7.38 M | 7.32-7.40 | 6.87 D | 6.98 D |
| H-4" | 7.96 D | 7.96 D | 7.96 D | 7.95 | - | - | 7.96 D | 7.19 M | - | 7.21 M | - |
| H-5" | 7.90 D | 7.90 D | 7.90 D | 7.89 | 8.30 M | 8.06 D | 7.90 D | 7.23 M | 8.12 D | 6.91 T | 6.98 D |
| H-6" | 7.50 M | 7.49 M | 7.51 M | 7.5 | 7.49 M | 7.54 M | 7.50 M | 7.29 M | 7.55 M | 7.29 M | 7.84 D |
| H-7" | 7.46 M | 7.45 M | 7.45 M | 7.45 | 7.50 M | 7.47 T | 7.45 M | - | 7.46 T | - | - |
| H-8" | 8.18 D | 8.18 D | 8.18 D | 8.19 | 8.33 M | 8.24 D | 8.17 D | - | 8.24 D | - | - |
| H-1' | 4.09 T | 4.09 T | 4.06 T | 4.03 | 4.07 M | 4.06 T | 4.14 T | 4.15 T | 4.06 T | 4.12 M | 4.14 T |
| H-5' | 4.37 dT | 4.37 dT | <3 | <3 | <3 | <3 | <3 | <3 | <3 | <3 | <3 |
| H-4"C1 | - | - | - | - | - | <3 | - | - | 3.17 Q | - | - |
| H-2"O | - | - | - | - | - | - | - | - | - | 3.81 S | - |
| H-4"O | - | - | - | - | 4.05 S | - | - | - | - | - | 3.88 S |
| H-2* | - | - | - | - | - | - | - | 4.31 S | - | 4.16 S | - |

H-1 NMR chemical shift values of the standards used for the confirmation of their presence in herbal extracts.

MI= Mountain Industry. A.L.= as labeled, S=singlet, D=doublet, T=triplet, Q=quadruplet, M=multiplet, dD=doublet of doublets, dT=doublet of triplets

referenced to residual CHCl_3 at 7.24 ppm (^1H). The proton sensitivity of the NMR instrument is $\geq 280:1$ using 0.1% ethylbenzene in CDCl_3 when methyl quartet signal region was evaluated with measured 200 Hz noise width between 3 ppm and 7 ppm. Typically one to five milligrams of the standard powder samples were weighed, dissolved in 1 mL CDCl_3 , and transferred to NMR sample tubes. Mountain Industry sample concentrations were roughly 5 mg/mL, and Cayman samples 1 mg/mL. The proton spectra were scanned 128 times (18 minutes) in the 0-10 ppm range, unless 512 scans (one hour) was necessary to obtain sufficient signal-to-noise ratio (S/N) for sample amounts less than 1 mg.

For "Spice" plant material sample analysis, ~50 mg of each herbal product was placed into ~1 mL of CDCl_3 and vortexed for one minute. The liquid solution was then transferred with a glass pipette to an NMR sample tube for NMR analysis. The proton NMR spectrum of each herbal extract was obtained after 32 scans (4 minutes) with a 4-second relaxation delay and chemical shift ranging from 0-10 ppm. The data were compared with the chemical shifts observed in the spectra of the standards to confirm the presence of the synthetic compounds.

With the powder sample, H-1 NMR was employed to elucidate the structures of synthetic cannabinoids. In most cases when a pure standard was available, matches of all chemical shift values were used to confirm its identity; for herbal samples, the standard chemical shift value ± 0.1 ppm range was used to account for peak marking deviation when the DELTA software (JEOL USA) was utilized. The H-1 NMR spectra of the herbal extracts were compared with their standard counterparts, particularly in the aromatic chemical shift region (6.5-9 ppm) and the mid-field region (4-5 ppm) where overlapping signals from both the base herb and the synthetic components were avoided.

Quantitative Herbal Extraction NMR Preparation:

For quantification, between 1 to 2 mg of maleic acid (e.g. 1.5 mg or 1.8 mg) was accurately weighed out and added to ~50 mg of herbal product, also accurately weighed. Approximately 1 ml of d_6 -acetone was added to extract the cannabinoid and subsequently served as the NMR solvent. The sample was then run utilizing the method previously described for H-1 NMR analysis of the herbal extracts. We have found that the longitudinal relaxation time, T_1 , for these indole cannabinoids are lower than 4 seconds so 4 seconds relaxation was used to speed up the analytical process without sacrificing the quantitative accuracy.

Results

The DART-MS spectra of JWH-019 and "Moon Spice" herbal sample are presented in **Figs 4a** and **4b**, respectively and are typical of the mass spectra observed for DART analyses. Figure 4c shows the comparison between the 90 V fragmentation mass spectrum from the Moon Spice sample and the pure JWH-018 standard. The exact masses for the matching ions within each spectrum were within 5 mmu of each other, thus indicating that they have the same elemental compositions. The other ions depicted in the Moon Spice 90 V spectrum (Fig. 4c) were produced from the fragmentation of the other cannabinoid compound present in the sample, RCS-04. The identification results on all of the other standards and herbal blends along with their NMR confirmations are presented in Table 1. The DART-MS results are generally supported by the NMR results.

Sometimes, due to the limitation on NMR sensitivity, the minor ingredients had a poor S/N compared to the major ingredients or in some cases the signals from the minor components dropped below the limit of detection of the instrument. As a result, the ratio of peak areas is only a rough and semi-quantitative measure of each component.

Three of the Mountain Industry powders were mislabeled synthetic cannabinoids and three contained other cannabinoids as contaminants (Table 1). The H-1 NMR chemical shift values of the standards are listed in Table 2, in which the Cayman standards had been correctly labeled and their spectra compared with those from Mountain Industry powders and the herbal extracts (Table 2 and **Table 3**).

Figure 5a is an H-1 NMR spectrum for the CDCl_3 extract of 50 mg of cannabinoid-free mugwort leaf. The sharp peak at 7.25 ppm is from protonated chloroform (CHCl_3), an impurity in the NMR solvent. As indicated in the spectrum, most of the signals from the leaf are within 1-3 ppm. Besides the residual solvent peak, the CDCl_3 extraction method did not produce any strong or noticeable signal from 3-10 ppm. The same phenomena were observed with mullein and damiana leaves, two popular choices for the base herb in incense products as indicated in online discussions among drug users.

Figure 5b is the H-1 NMR spectrum of 1.0 mg RCS-04 cannabinoid standard purchased from Cayman Chemical. As the spectrum indicates, the signals within 3.5-9 ppm do not overlap with blank herbal signals shown in the top panel. The bottom panel is from the CDCl_3 extracts of "Moon Spice" herbal incense. The signals for RCS-04 were found at seven locations. The remaining signals from 4-9 ppm are from JWH-018 according to literature values [1, 5] and the correlating chemical shift values are listed in Table 3. JWH-018 and RCS-04 were detected by both DART-MS and NMR (Table 1). Occasionally a proton signal for water (a broad singlet anywhere from 1.2 to 1.8 ppm) is present in the resulting spectra, but has not interfered with our region of interest: 3.5-9 ppm.

As Table 2 indicates, the "AM-1221" compound from Mountain Industry is indeed a mislabeled AM-2201 (Fig. 1).

Fig. 3



Various Spice products: (a) "Mountain Industry" JWH-122 powder, (b) "Moon Spice" leaf, (c) "Mr. Nice Guy" "Spice" package, (d) "Melon: Code Black" "Spice" package. 152 x 139 mm (300 x 300 DPI)

The herbal extract NMR data (Fig. 5 and Table 3) confirmed the results obtained in the DART-MS experiments (Figs 4b and 4c). HPLC-DAD and conventional GC-MS methods were utilized to confirm all positive identifications indicated in Table 1.

To quantify the cannabinoids present in the extract it is important that a well-phased spectrum is obtained. Minor phasing parameter adjustment can be made so the spectrum is

in phase. The internal standard, maleic acid (MA), produces a signal at 6.37 ppm due to the two equivalent protons of the methylene group (**Fig. 6**). Well-resolved sample peaks are identified and manual integration is performed (Fig. 6). The MA peak area is normalized and the values obtained are plugged into the equation below to calculate the amount of cannabinoid in milligrams.

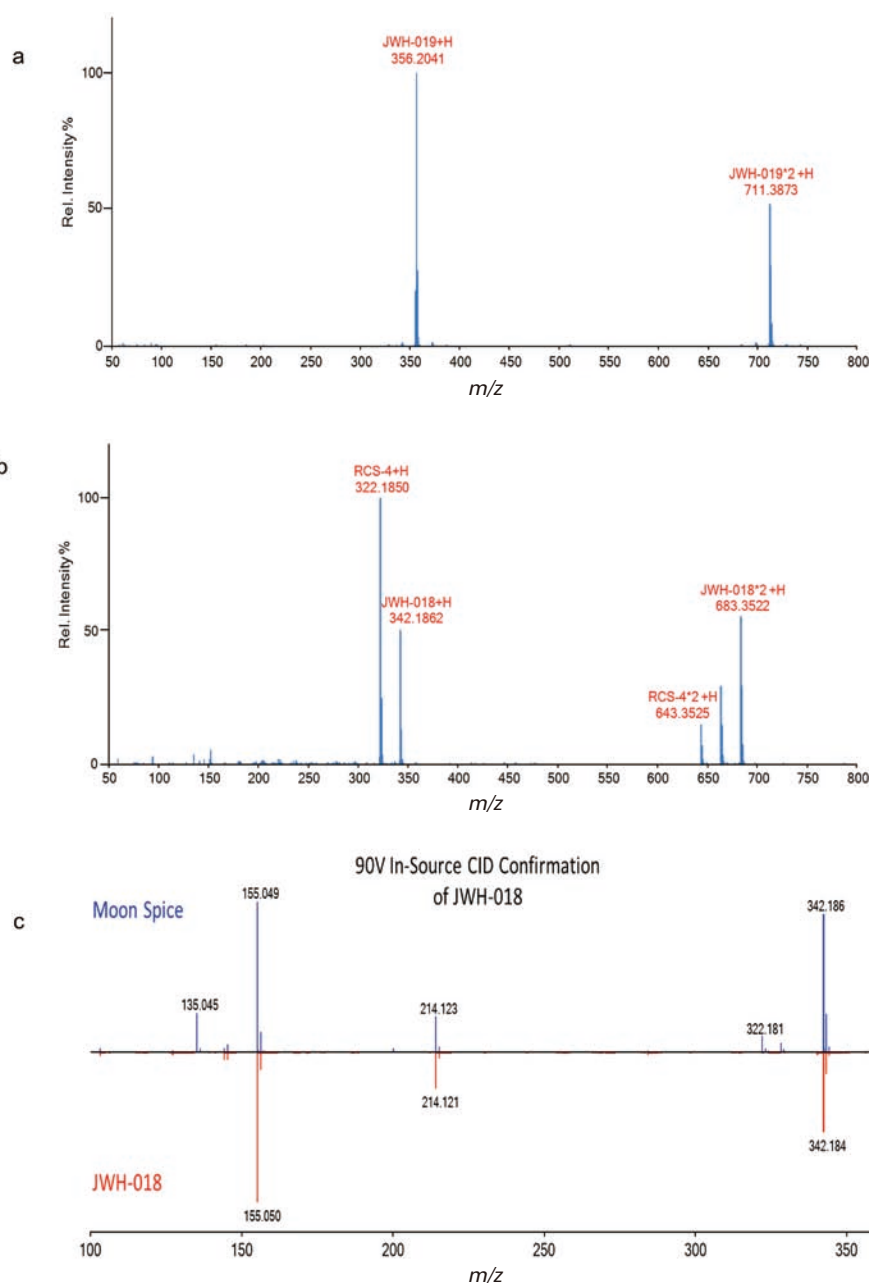
$$mg\ of\ cannabinoid = \frac{(mg\ of\ MA) \times (\#\ of\ protons\ in\ MA) \times (Integral\ of\ cannabinoid\ peak) \times (FW\ of\ cannabinoid)}{(Integral\ of\ MA\ peak) \times (FW\ of\ MA) \times (\#\ of\ protons\ represented\ by\ cannabinoid\ peak)}$$

MA = Maleic Acid

FW = Formula weight (in g/mol)

Integral = integrated area under the peak of interest with arbitrary unit.

Fig. 4



DART-MS Spectra of (a) JWH-019 powder standard and (b) one piece of "Moon Spice" leaf, along with (c) the comparison of the 90V-spectra between "Moon Spice" leaf and JWH-018 standard powder. 381 x 508 mm (300 x 300 DPI)

The calculated mass of cannabinoid is divided by the amount of herb (in grams) initially weighed out in order to acquire a concentration in the form of mg of cannabinoid per g of herb in the Spice sample. The entire process of quantifying one sample is completed in less than 10 minutes. The quantitative NMR results are comparable to our chromatographic quantification results, both methods yielding 0.5-122 mg of cannabinoids per gram of herbal product. Because extraction with methanol is less efficient than with acetone, chromatographic quantification results only represent a fraction of the actual amount as indicated in our previous work (Table 2).

The quantitative results of twelve Spice products are displayed in Table 3. Variation in the manual peak integration was found to average about 3% using the same spectrum with five repeated integrations on three different peaks. Some herbal samples (K250, Head Trip, and Extremely Legal) were only quantified using three trials due to low sample availability. The integration results from different proton peaks of the same cannabinoids are very similar. As indicated in Table 3, the relative standard deviation varies (from 7% to 68%) due to the uneven spreading of synthetic components on herbal surface during the manufacturing process. This indicates that there is little to no quality control in the production of these substances, adding to the danger for consumption. Ingestion of even small amounts may result in pronounced effects because of inconsistencies in the dosage, significantly increasing the risk of these drugs. The LOD and LOQ were found to be 0.11 mg/mL and 0.36 mg/mL, respectively, with AM-2201 external standard calibration (0.1-1.5 mg/mL) and accurately-weighed maleic acid internal standard (1-2 mg).

Due to small sample size and uneven coverage of cannabinoids on the herbal samples, the results are only semi-

quantitative with short proton scanning (4-second relaxation). Despite that, the methodology accurately represents drug consumption and therefore provides valuable information in this respect. Quantitative scanning takes the same amount of time as a qualitative scanning with CDCl_3 . The total analytical time for five repeated trials is about one hour.

Summary

The selected blank herbal leaves are popular base-herb choices among makers of synthetic marijuana because they have pleasant aromas, low prices and are readily available. These leaf samples were analyzed through DART-MS as blanks and showed no mass spectral peaks that could be associated with synthetic cannabinoids. For the NMR experiments, the blank leaves were prepared using the same extraction method utilized for the herbal spice samples prior to their NMR analyses. Peaks were not found between 6.5-9 ppm or from 3.5-5 ppm, which is where most synthetic cannabinoids demonstrate strong signals. These results confirmed that the detected signals in the spice samples all originated from the synthetic compounds rather than natural herbal constituents.

The combination of DART-TOF-MS and NMR, used in conjunction with the standards, quickly identified the synthetic cannabinoids in their powder form and as an additive in the herbal products. Total analysis time was under one hour including about five minutes for DART-MS analysis and under 10 minutes for NMR analysis. According to our study, the four-minute 32-NMR scans generated an S/N of 4 to 1 for as little as 50 μg of a cannabinoid sample with successful identification. Our HPLC-Diode Array Detection (DAD) quantification on all the herbs (data not shown) revealed that the concentration

Table 3

| Label | Barely Legal | | Melon Code Black | | Moon Spice | | Sweet Leaf | | |
|-------|--------------|-----------|------------------|-----------|------------|-----------|------------|-----------|-----------|
| | AM-2201 | RCS-04 | JWH-122 | JWH-203 | RCS-04 | JWH-018 | JWH-210 | JWH-122 | JWH-250 |
| H-2 | 7.28-7.41 | 7.41-7.58 | 7.32-7.40 | 7.88 S | 7.57 S | 7.36 M | 7.32-7.40 | 7.32-7.38 | 7.86 S |
| H-4 | 4.48 M | 8.36 M | 8.46 M | 8.39 M | 8.36 M | 8.47 M | 8.48 M | 8.48 M | 8.39 M |
| H-5 | 7.28-7.41 | 7.28-7.41 | 7.32-7.40 | 7.28 M | 7.25-7.38 | 7.33-7.38 | 7.32-7.40 | 7.32-7.38 | 7.25-7.32 |
| H-6 | 7.28-7.41 | 7.28-7.41 | 7.32-7.40 | 7.32-7.40 | 7.25-7.38 | 7.33-7.38 | 7.32-7.40 | 7.32-7.38 | 7.25-7.32 |
| H-7 | 7.28-7.41 | 7.28-7.41 | 7.32-7.40 | 7.32-7.40 | 7.25-7.38 | 7.33-7.38 | 7.32-7.40 | 7.32-7.38 | 7.25-7.32 |
| H-2" | 7.64 M | 7.83 M | 7.55 M | - | 7.84 D | 7.64 M | 7.55 M | 7.55M | - |
| H-3" | 7.41-7.58 | 6.98 M | 7.32-7.40 | 7.32-7.40 | 6.98 D | 7.52 M | 7.32-7.40 | 7.32-7.38 | 6.87 D |
| H-4" | 7.96 M | - | - | 7.19-7.23 | - | 7.96 D | - | - | 7.21 M |
| H-5" | 7.90 M | 6.98 M | 8.05 M | 7.19-7.23 | 6.98 D | 7.90 D | 8.12 D | 8.06 D | 6.91 T |
| H-6" | 7.41-7.58 | 7.83 M | 7.54 M | 7.26-7.30 | 7.84 D | 7.48 M | 7.55 M | 7.54 M | 7.25-7.32 |
| H-7" | 7.41-7.58 | - | 7.47 T | - | - | 7.48 M | 7.46 T | 7.47 T | - |
| H-8" | 8.16 D | - | 8.22 M | - | - | 8.17 D | 8.24 D | 8.24 D | - |
| H-1' | 4.09 M | 4.15 M | 4.06 T | 4.15 T | 4.15 T | 4.05 T | 4.06 T | 4.06 T | 4.12 T |
| H-4"O | - | 3.88 S | - | - | 3.88 S | - | - | - | 3.81 S |
| H-5' | 4.37 dM | - | - | - | - | - | - | - | - |
| H-4"C | - | - | - | - | - | - | 3.17 Q | - | - |
| H-2* | - | - | - | 4.31 S | - | - | - | - | 4.16 S |

Chemical shift values identified in 50 mg herbal extracts. S=singlet, D=doublet, T=triplet, Q=quadruplet, M=multiplet

of cannabinoid on herbal base ranges from 1-50 mg/g of herb. 50 µg is usually below the amount we found on 50 mg herbal product. When the sample concentration falls below 0.05 mg/mL comparable to DART-MS LOD [4], the NMR scan times have to be increased to four hours or more in order to obtain a spectrum with a S/N higher than 5. The adoption of 50 mg of herbal sample size for NMR investigation implies that at least 50 µg was placed in an NMR tube along with 0.5-1 mL CDCl₃. The concentration of a cannabinoid was much higher than the detection limit of 1 part per million or 1 µg/g for H1-NMR. Mixtures of two or three cannabinoids were readily identified by using the combined NMR and MS methods (Table 1).

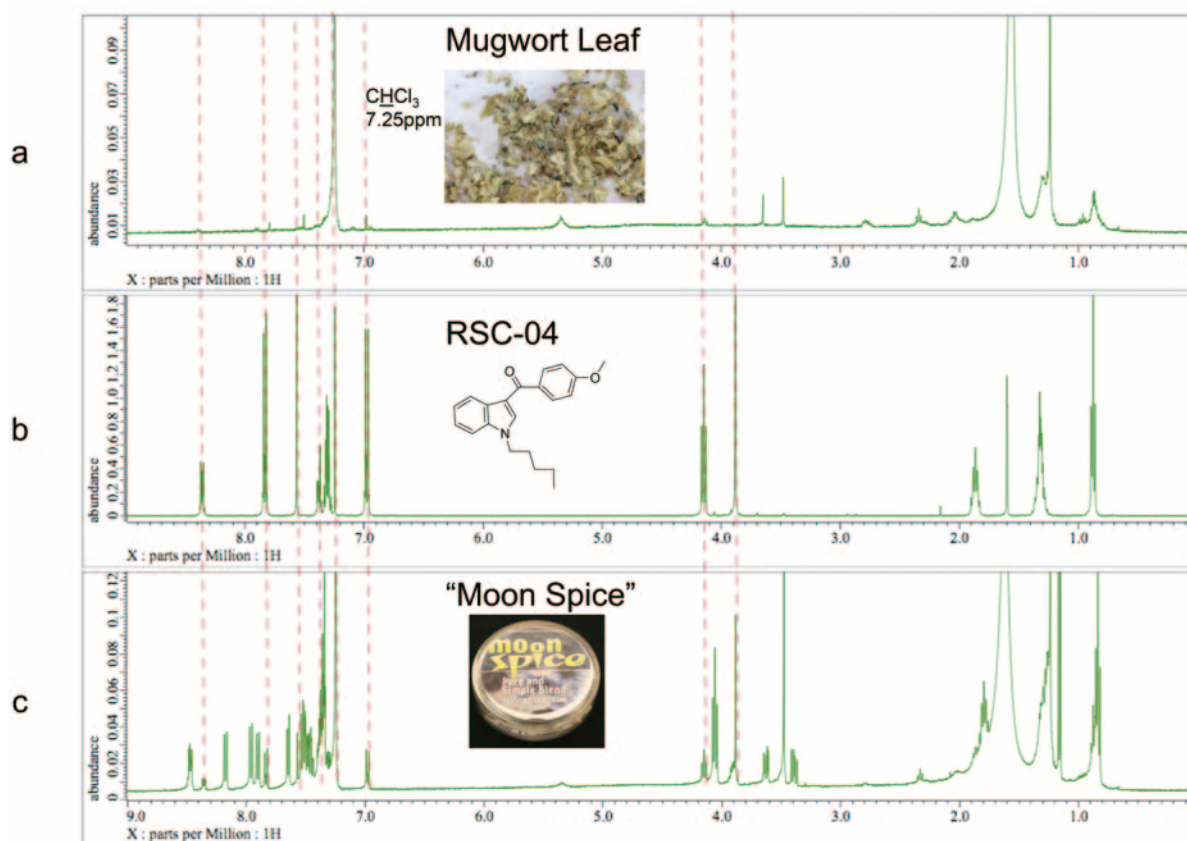
As Table 1 demonstrates, NMR and DART-MS complement each other in the analysis of herbal blends, especially when more than one synthetic cannabinoid is present. If one minor component is missed by one method, the other method usually detects it. The minor ingredient in the NMR spectrum often produces peaks with poor S/Ns so either more scans need to be acquired, which increases experiment time, or an increased sample amount (e.g. 200 mg) is necessary. Additionally, increased sampling with more sample batches is sometimes necessary to get a better representation of the whole package. The herbal sample is not homogenized to demonstrate the variation in concentrations for “hot” and “cold” spots, which could cause great harm for unaware users. Mixtures were detected with DART-MS spectra as signals of various heights, which further confirmed the non-uniformity of the synthetic compound distribution among the herbal bases. Sometimes

only one compound was discovered on one piece of leaf while another piece from the same bag at a different location produced peaks responsible for two synthetic compounds in the mass spectrum. These results show that it is important to perform at least three different measurements using different leaves from a particular herbal sample to comprehensively identify all of the components in an herbal mixture. And this also made NMR confirmation very important as the 50-mg sample size usually contains more than a dozen pieces of leaves.

Our recent research efforts have extended towards using 2D NMR techniques for both identification and quantification [12]. The added dimension from the 2D NMR techniques provided additional signals that were easier to differentiate than those acquired by 1D NMR analysis, and valuable correlation signals for screening and comparison.

In summary, the combination of NMR and DART-MS can provide concrete identifications of synthetic cannabinoids rapidly and without ambiguity. The combined method also maximizes the potential of instrumental detection and signal separation power that is inherent in DART-MS and NMR while minimizing cumbersome wet chemistry processing and organic solvent usage. Up to a three-component mixture from herbal Spice sample was detected with the correct isomer identifications (Table 1). The DART-MS+NMR method will hopefully accelerate the drug detection process in the enforcement of current laws and regulations, as well as the detection of future blends sold as “herbal potpourri” or “legal highs”.

Fig. 5



Proton-NMR spectra of (a) 50 mg blank herb "Mugwort Leaf" extracted with CDCl₃, (b) 5 mg RCS-04 standard powder in 1 mL CDCl₃, and (c) 50 mg "Moon Spice" herbal sample extracted with 1 mL CDCl₃, 558 x 431 mm (300 x 300 DPI)

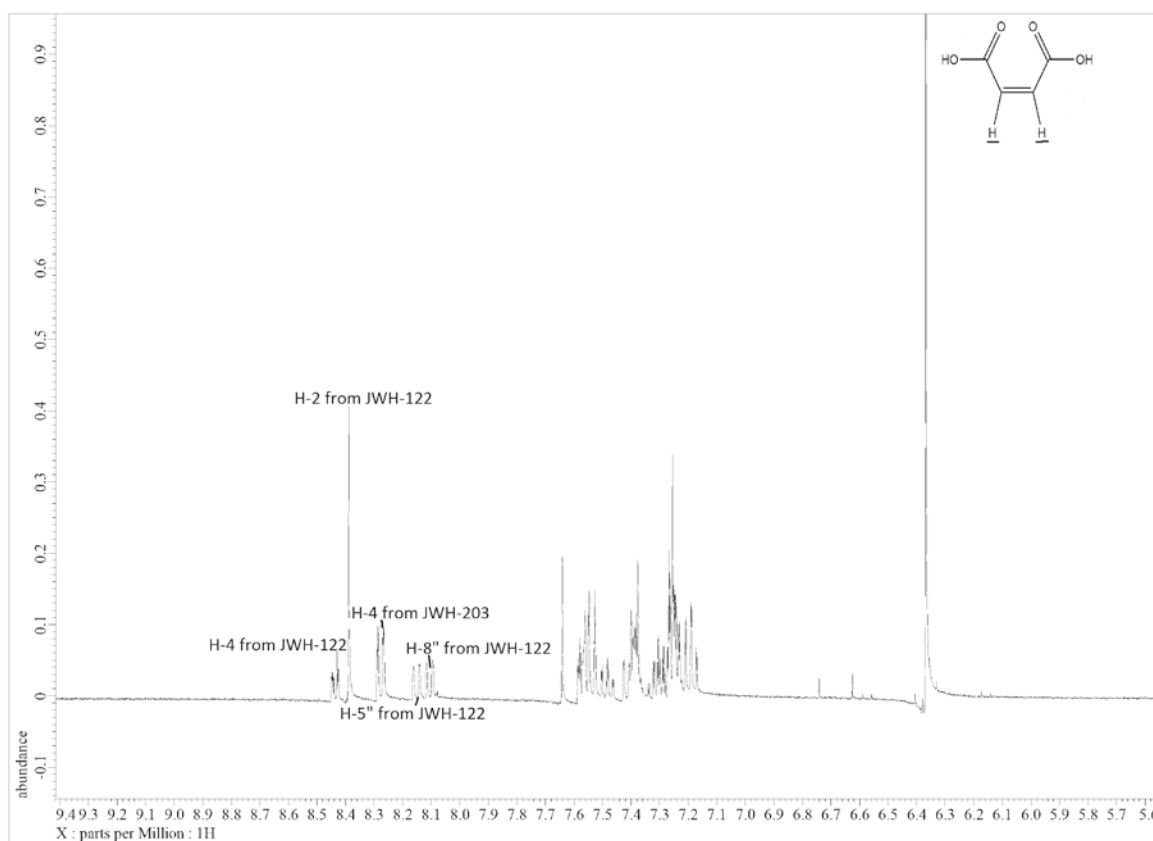
Acknowledgments

The authors acknowledge Dr. Nanette Wachter for her support and helpful discussion on the NMR experiments. Ashok Krishnaswami from JEOL USA provided some technical information on NMR. We thank Richard Picciochi for the photography assistance with Fig. 3. Amanda Rivera and Michaela Vertorano conducted HPLC separations with DAD detection to confirm our DART-MS and NMR findings. Joseph Guttieri performed conventional GC-MS analysis as another confirmatory method.

References

- [1] Lindigkeit R, Boehme A, Eiserloh I, Luebbecke M, Wiggermann M, Ernst L, Beuerle T. Spice: A never ending story? *Forensic Sci Int.*, 2009;**191**:58-63.
- [2] Fattore L, Fratta W. BeyondTHC: the new generation of cannabinoid designerdrugs. *Front Behav Neurosci.*, 2011;**5**:1-12.
- [3] Marino, M. A., Voyer, B., Cody, R. B., Dane, A. J., Veltri, M. and Huang, L. (2016), Rapid Identification of Synthetic Cannabinoids in Herbal Incenses with DART-MS and NMR. *J. Forensic Sci.*, **61**: S82-S91.
- [4] Steiner R, Larson R. Validation of the direct analysis in real time source for use in forensic drug screening. *J. Forensic Sci.*, 2009;**54**: 617-22.
- [5] N. Uchiyama, R. Kikura-Hanajiri, N. Kawahara, Y. Goda, *Forensic Toxicol.*, 2009, **27**, 61.
- [6] N. Uchiyama, R. Kikura-Hanajiri, J. Ogata, Y. Goda, *Forensic Sci. Int.*, 2010, **298**, 31.
- [7] N. Uchiyama, R. Kikura-Hanajiri, M. Kawamura, Y. Goda, *Forensic Toxicol.*, 2010, **29**, 25.
- [8] Musah RA, Domin MA, Cody RB, Lesiak AD, Dane AJ, Shepard JRE. DART-MS Collision Induced Dissociation (CID) for structural analysis of synthetic cannabinoids. *Rapid Comm Mass Spec.*, 2012;**26**(19):2335-42.
- [9] Musah RA, Domin MA, Walling MA, Shepard JRE. Rapid identification of synthetic cannabinoids in herbal samples via direct analysis in real time mass spectrometry. *Rapid Comm Mass Spec.*, 2012;**26** (9):1109-14.
- [10] Ernst L, Schiebel HM, Theuring C, Lindigkeit R, Beuerle T. Identification and characterization of JWH-122 used as new ingredient in "Spice-like" herbal incenses. *Forensic Sci Int.*, 2011;**208**:e31-e35.
- [11] Jankovics P, Váradi A, Tölgyesi L, Lohner S, Németh-Palotás J, Balla J. Detection and identification of the new potential synthetic cannabinoids 1-pentyl-3-(2-iodobenzoyl)indole and 1-pentyl-3-(1-adamantoyl)indole in seized bulk powders in Hungary. *Forensic Sci Int.*, 2012;**214**:27-32.
- [12] Fowler F, Voyer B, Marino MA, Finzel J, Veltri M, Wachter NM, Huang L. Rapid screening and quantification of synthetic cannabinoids in herbal products with NMR spectroscopic methods. *Anal. Methods*, 2015, **7**, 7907.

Fig. 6



Quantitative proton NMR spectrum of Melon Code Black with maleic acid internal standard. JWH-122 and JWH-203 were found and quantified.

Nanostructured Surface Phonon Polariton Systems for Mid-Infrared Nanophotonics

Alexander J. Giles^{1,2}, Richard Kasica³, Joshua D. Caldwell²

¹ National Research Council Postdoctoral Fellow

² The United States Naval Research Laboratory

³ The National Institute for Standards and Technology

In this article, novel, phonon-based silicon carbide nanopillar antenna arrays are described. Using fabricated SiC structures, sub-diffractive, localized resonances are observed with exceptionally high quality factors (40-305) and corresponding high modal confinements in the mid-infrared (IR) spectral region. These results exceed the theoretical limit of plasmonic systems and establish a basis for nanophotonics in the mid-IR and beyond, opening the door to a wide range of applications in sensing, lithography, optical circuitry and more.

Introduction

The manipulation of light at sub-wavelength dimensions has become a compelling field of research, as the limits imposed by classical diffraction can now be largely surpassed [1]. Initially observed on metal films [2], surface plasmon polaritons (SPPs) are electromagnetic excitations that exhibit sub-diffractive confinement of optical fields. The discovery of these SPPs led, in part, to the field of plasmonics, nanophotonics [3] and metamaterials [4], which in turn have led to advancements in optics and electronics [5, 6]. However, much of the promise of these SPPs has not been realized due to the high optical losses in these metals at optical frequencies [7-9]. Further, such materials have very large, negative permittivities at longer wavelengths, limiting their efficacy for nanophotonics beyond the near-infrared (IR) regime. These issues have motivated a search for alternative materials and strategies that can provide low optical losses, while also extending the operational polaritonic bands into the IR and terahertz (THz) regimes.

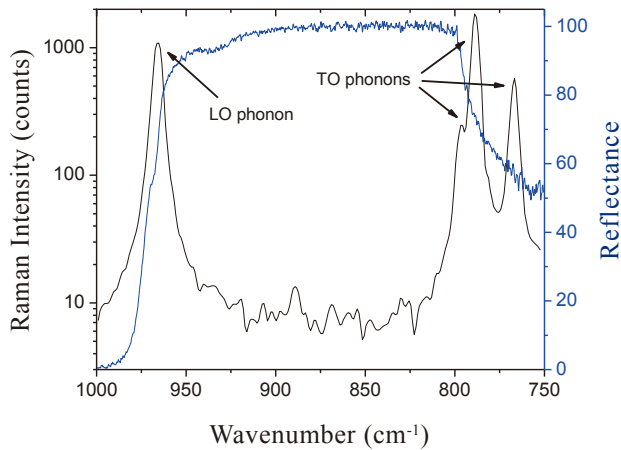
Polar dielectrics such as SiC afford an opportunity to achieve sub-wavelength confinement with low optical losses and operation in the mid-IR through surface *phonon* polaritons (SPhPs). This spectral region offers a tremendous variety of applications, including an atmospheric window for free-space communications between 8-12 μm , near-room temperature black-body emission peaks ($\sim 10 \mu\text{m}$), and a variety of IR-active molecular vibrational resonances, useful for the identification of chemical species. SPhPs are a consequence of a coupling between incident electromagnetic fields (light) and the polar optic phonons present in polar dielectric materials. This results in a coherent oscillation of these charged ionic species enabling the formation of these SPhPs and the ability to confine light at these frequencies to sub-diffractive dimensions. The corresponding operating frequency bands exist between the

transverse optic (TO) and longitudinal optic (LO) phonon modes, a region known as the Reststrahlen band [10, 11], within which extremely high reflectivity occurs (**Fig. 1**). As these SPhPs are phonon-based, their loss is derived from the scattering lifetimes of optic phonons, which are on the order of picoseconds [11, 12]. This provides a dramatic improvement over their SPP-based analogues, whose electron scattering lifetimes are orders of magnitude shorter [13, 14].

Nanostructured surface phonon polariton systems

Within the highly reflective Reststrahlen band, the reflection of incident light approaches 100% (Fig. 1) [10]. This is due to the coherent oscillations of bound charges on the atomic lattice, which screen out the incident electromagnetic fields and are manifested in a negative real part of the dielectric function [15]. This situation is analogous to the highly reflective behavior of metals at frequencies below the plasma frequency of that material, in which case coherent free electron oscillations [12]. In either case, the dispersion relation can be approximated as a Lorentz oscillator, however, for the case of SPhPs, the ability to stimulate and support polaritonic modes only exists within this Reststrahlen band. The local electromagnetic fields resulting from the SPhP decays evanescently as one moves away from the polar dielectric surface into a dielectric medium with positive permittivity (air, for example).

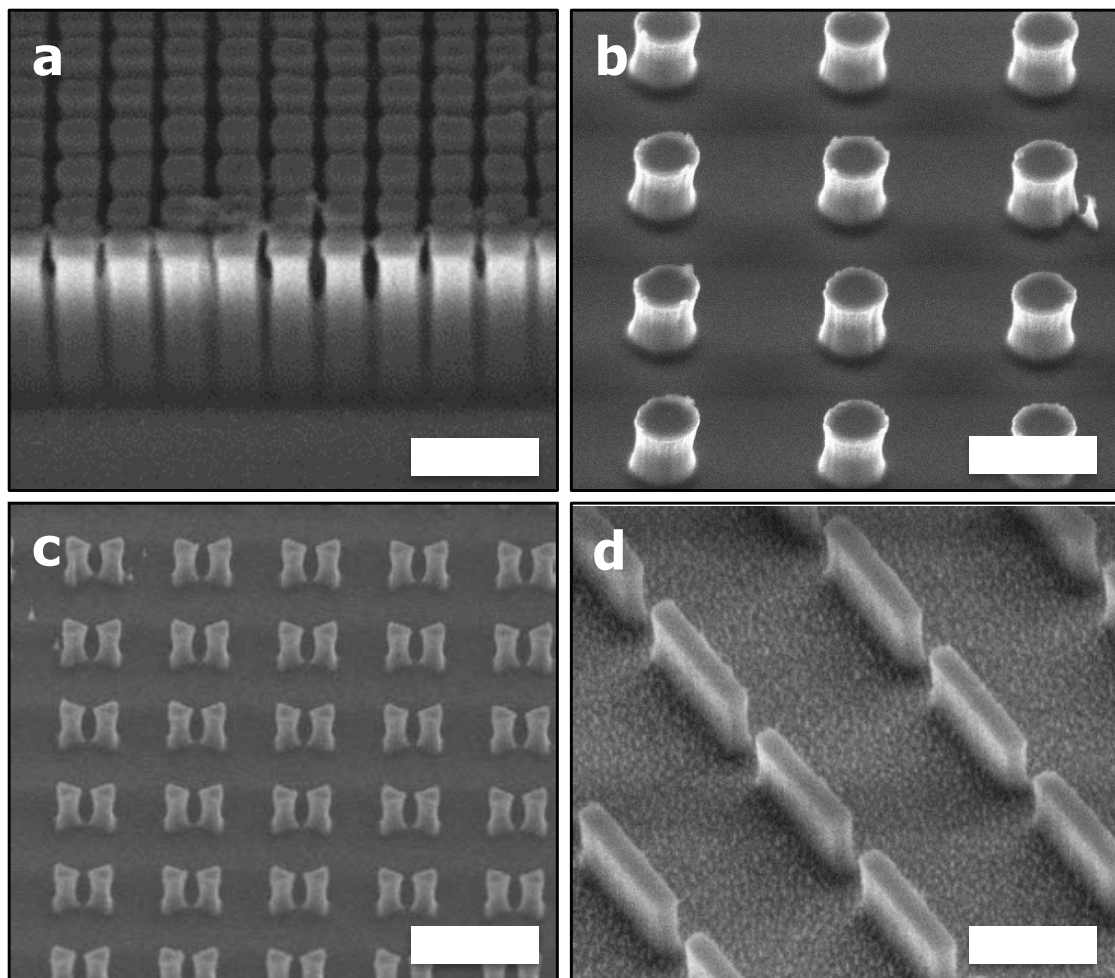
Similar to SPPs, the momentum mismatch between the incident light and the SPhP modes, requires a means to reduce the momentum of light such that an overlap between the light line, $k = \omega/c$ and the SPhP dispersion curve can be established. This mismatch can be overcome with a high index prism [16, 17], diffraction gratings, a scanning near field microscopy (SNOM) tip [18, 19], or via nanostructuring the material into

Fig. 1


Raman spectra (black line) and reflection spectra (blue line) of un-patterned 6H-SiC. The phonon resonances are seen in the labeled Raman peaks which bound the highly reflective Reststrahlen band.

sub-wavelength elements [15, 18].

In order to probe the fundamental SPhP excitations within these polar media, we fabricated a variety of nanostructured arrays (**Fig. 2**) in high quality, ~ 350 μm thick semi-insulating 4H- and 6H-SiC samples using a JEOL JBX-6300FS direct-write electron beam lithography (EBL) system. The wide-bandgap and low-background doping of the semi-insulating SiC results in poor electron transport through the substrate, severely limiting the resolution of traditional EBL techniques due to charging and back scattering [20]. We attempted several methods to mitigate these effects and found that a commercially available charge dissipation solutions (eSpacer, Showa Denko) provided the best results via spinning a thin coating on top of the resist stack. We used a bilayer PMMA resist consisting of a 120 nm bottom layer (molar mass = 495k Da) and a 50 nm top layer (molar mass = 950k Da), which greatly improved liftoff success rates. Further, by employing proximity correction techniques and writing at a 100 kV beam energy, we were able to resolve structures with lateral dimensions as small as 50 nm and gaps as small as 25 nm over large area arrays (> 300 μm). After e-beam writing and development, a 30 nm Al/Cr hard mask was

Fig. 2


Different designs of phonon polariton nanoantennas fabricated in SiC. All scale bars are 1000 nm. (a) Closely spaced nanopillar array. (b) Widely spaced nanopillar array. (c) Coupled bowties. (d) High aspect ratio cuboids.

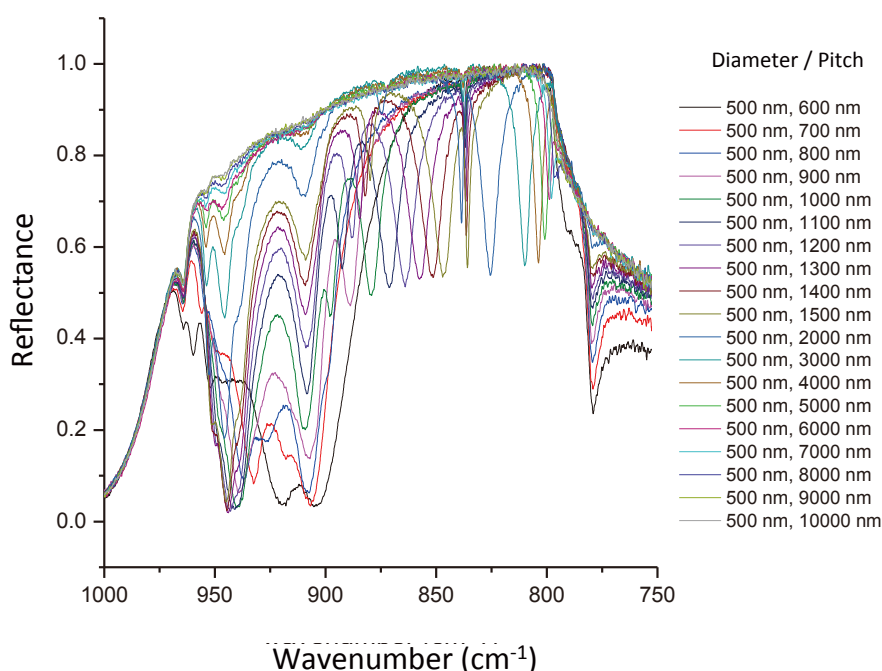
deposited via electron beam evaporation and then lifted off in a 60°C n-methyl-2-pyrrolidone solution.

The sample was then characterized optically before reactive ion etching (RIE) was carried out. Equal partial pressures of SF₆ and Ar were used at 150 W RF power at 25°C for 38 minutes, resulting in an etch depth of approximately 800 nm. After the RIE process, the metal caps were removed in consecutive baths of 50° C 16:1:1:2 HNO₃:H₃PO₄: CH₃COOH:H₂O and 25°C 2:3:28 HClO₄:Ce(NH₄)₂(NO₃)₆:H₂O to remove the Al and Cr, respectively. Several methods were investigated to repair residual surface damage associated with fluorine and other etch gas contaminants during the RIE process. The surface condition of these resonators is especially important as the SPhP modes are confined to the surface, and therefore are extremely sensitive to any morphological or chemical defects. We obtained the highest quality factors via a post-process treatment of the structures in a 70°C mixture of 2-(2-aminoethoxy) ethanol, hydroxylamine and 1,2-dihydroxybenzene (commercially sold as DuPont™ PlasmaSolv® EKC-265™) for 60 minutes. This process removes most chemical surface contaminants, while leaving the morphology of the SiC features relatively unharmed. FTIR spectroscopy was used to characterize the mid-IR reflectance properties of these nanopillar arrays. A 15x, 0.58 NA objective was used to illuminate the sample with a SiC glow bar at incident angles between 10-35° off normal, with a weighted average angle of 25°. This experimental setup provided polarization vector components both in plane and out of plane (with respect to the substrate surface), exciting modes in both the transverse and longitudinal directions. The spectra were collected at a 0.5 cm⁻¹ resolution with 128 scans averaged. The aperture was set to a 50 × 50 μm square, in order to coincide with the dimensions of the each array. Freshly deposited, optically thick Au films were used to collect background spectra at the same spectral resolution.

Tunable, high quality, sub-diffractive SiC nanoresonators

Figure 3 illustrates the tremendous tunability of the resonant properties of the SPhP modes within these SiC nanopillar arrays, providing high quality factor, highly absorptive resonances at almost any spectral position within the Reststrahlen band. For any damped oscillator, the ratio of the resonance linewidth (FWHM) to resonance frequency, is defined as the quality factor Q , and represents the rate of energy loss compared to the stored energy within the resonator. For the 100-500 nm diameter nanopillars we measured quality factors ranging from 40-305 [19-21]. This is in excess of any reported values for single particle plasmonic resonator, with silver having a theoretical limit for a spherical particle of about 40 [9]. Further, it is important to realize the scale of confinement within these structures. Incident free-space photon wavelengths are on the order of 10-12.5 μm, while nanopillar dimensions are on the order of 100 nm, providing exceptionally sub-wavelength field confinements and dramatic electric field enhancements. Simulations suggest electric field enhancements of 5000x [22], while enhancements as high as 27,700 were calculated for a single mode. Electromagnetic simulations of such nanopillars further suggested two fundamental types of modes: A transverse dipole that oscillates in-plane and a longitudinally oscillating ‘monopole’ mode that is supported by the SiC substrate. The latter is not seen in isolated plasmonic structures as they do not possess a polaritonic substrate (ground plane) to support the opposite charge. We have found that we can preferentially excite each of these types of modes by changing the polarization angle of the incident field: The stronger a vertical component of polarization is, the stronger the monopole resonance is; the stronger the in plane component of polarization is, the stronger the transverse dipole resonances are. We discuss this is more

Fig. 3



SPhP resonances in nanopillar arrays of 500 nm diameter SiC pillars. By varying the center to center distance (pitch) of the pillars in these arrays, one can precisely tune the spectral positions of these absorptive resonances.

detail in a recent article [22].

Beyond cylindrical nanopillars, we have recently explored the effect of nanopillar shape, observing that specific geometries can allow for the excitation of over a dozen distinct modes that cannot be excited in structures with higher degrees of symmetry (i.e. spheres or cylinders). Further, these resonances can be tuned spectrally without affecting the near-field profile of the mode. These SPhP modes can be highly complex three dimensional field geometries that are able to concentrate charge and electromagnetic fields to exceptionally small areas of the pillar, providing an avenue towards nanoscale control of electromagnetic field patterns for tailored, narrow band thermal emitters [23, 24] that can provide ‘LED’-like performance in the mid- to far-IR with a simple, low-cost, solid-state device consisting of the nanostructured material and an integrated heater [25].

Summary

In summary, we have demonstrated fabrication of high quality SiC nanostructure arrays in a variety of shapes, sizes and spacings. These nanostructures exhibit strong localized surface phonon polariton (SPhP) resonances, which are highly tunable both spectrally and geometrically with respect their near field profiles. These modes are derived from optic phonons and thus have long modal lifetimes and exceptionally narrow linewidths, corresponding to quality factors as well in excess of any previously reported polaritonic material systems. The phonon polariton materials described in this article open up new opportunities not accessible to plasmonic materials, such as reciprocal hyperbolicity [18, 26], tuning via modulation of the carrier concentration [27], broadband operation via multi layered materials [28], and more. It is our hope that this approach will stimulate further research and new advances in mid-infrared nanophotonics and beyond.

Acknowledgements

The author acknowledges support from the National Research Council (NRC) NRL Postdoctoral Fellowship Program. Funding was provided via the Office of Naval Research and distributed by the Nanoscience Institute at the Naval Research Laboratory.

References

- [1] Koenderink, A. F.; Alù, A.; Polman, A. *Science* (2015) **348**, (6234), 516-521.
- [2] Ritchie, R. H. *Physical Review Letters* (1957) **106**, (5), 874-881.
- [3] Brongersma, M. L.; Kik, P. G., *Surface plasmon nanophotonics*. Springer: New York (2010).
- [4] Engheta, N.; Ziolkowski, R. W., *Metamaterials: physics and engineering explorations*. Wiley & Sons: Hoboken, NJ, (2006).
- [5] Caldwell, J. D.; Glembocki, O.; Bezares, F. J.; Bassim, N. D.; Rendell, R. W.; Feygelson, M.; Ukaegbu, M.; Kasica, R.; Shirey, L.; Hosten, C. *ACS Nano* (2011) **5**, (5), 4046-4055.
- [6] Caldwell, J. D.; Glembocki, O. J.; Bezares, F. J.; Kariniemi, M. I.; Niinistö, J. T.; Hatanpää, T. T.; Rendell, R. W.; Ukaegbu, M.; Ritala, M. K.; Prokes, S. M.; Hosten, C. M.; Leskelä, M. A.; Kasica, R. *Opt. Express* (2011) **19**, (27), 26056-26064.
- [7] Khurgin, J. B.; Boltasseva, A. *MRS Bulletin* (2012) **37**, 768-779.
- [8] Khurgin, J. B.; Sun, G. *Applied Physics Letters* (2010) **96**, 181102.
- [9] Khurgin, J. B.; Sun, G. *Applied Physics Letters* (2011) **99**, 211106.
- [10] Adachi, S., The Reststrahlen Region. In *Optical Properties of Crystalline and Amorphous Semiconductors: Materials and Fundamental Principles*, Springer Science+Business Media, LLC: New York, NY, (1999) pp 33-61.
- [11] Yu, P. Y.; Cardona, M., *Fundamentals of Semiconductors: Physics and Materials Properties*. Springer: New York, NY, (1999).
- [12] Bohren, C. F.; Huffman, D. R., *Absorption and Scattering of Light by Small Particles*. John Wiley & Sons, Inc.: Weinheim, Germany, (2004).
- [13] Bosman, M.; Ye, E.; Tan, S. F.; Nijhuis, C. A.; Yang, J. K. W.; Marty, R.; Mlayah, A.; Arbouet, A.; Girard, C.; Han, M.-Y. *Scientific Reports* (2013) **3**, 1312.
- [14] Kreibig, U.; Vollmer, M., *Optical Properties of Metal Clusters*. Springer: Berlin, (2010).
- [15] Caldwell, J. D.; Lindsey, L.; Giannini, V.; Vurgaftman, I.; Reinecke, T.; Maier, S. A.; Glembocki, O. J. *Nanophotonics* (2015) **4**, (1), 44-68.
- [16] Lahiri, B.; Holland, G.; Aksyuk, V.; Centrone, A. *Nano Letters* (2013) **13**, (7), 3218-3224.
- [17] Ng, S. S.; Hassan, Z.; Abu Hassan, H. *Solid State Communications* (2008) **145**, 535-538.
- [18] Caldwell, J. D.; Kretinin, A.; Chen, Y.; Giannini, V.; Fogler, M. M.; Francescato, Y.; Ellis, C.; Tischler, J. G.; Woods, C.; Giles, A. J.; Hong, M.; Watanabe, K.; Taniguchi, T.; Maier, S. A.; Novoselov, K. S. *Nature Communications* (2014) **5**, 5221.
- [19] Chen, Y.; Francescato, Y.; Caldwell, J. D.; Giannini, V.; Maß, T. W. W.; Glembocki, O. J.; Bezares, F. J.; Taubner, T.; Kasica, R.; Hong, M.; Maier, S. A. *ACS Photonics* (2014) **1**, (8), 718-724.
- [20] Brewer, G., *Electron Beam Lithography in Microelectronic Fabrication*. Academic Press: New York, (2012).
- [21] Caldwell, J. D.; Glembocki, O. J.; Sharac, N.; Long, J. P.; Owrutsky, J. O.; Vurgaftman, I.; Tischler, J. G.; Bezares, F. J.; Wheeler, V.; Bassim, N. D.; Shirey, L.; Francescato, Y.; Giannini, V.; Maier, S. A. *Nano Letters* (2013) **13**, (8), 3690-3697.
- [22] Caldwell, J. D.; Glembocki, O. J.; Sharac, N.; Long, J. P.; Owrutsky, J. O.; Vurgaftman, I.; Tischler, J. G.; Bezares, F. J.; Wheeler, V.; Bassim, N. D.; Shirey, L.; Francescato, Y.; Giannini, V.; Maier, S. A. *Nano Letters* 2013, **13**, (8), 3690-3697.
- [23] Greffet, J.-J.; Carminati, R.; Joulain, K.; Mulet, J. P.; Mainguy, S. P.; Chen, Y. *Nature* 2002, **416**, (6876), 61-64.
- [24] Schuller, J. A.; Zia, R.; Taubner, T.; Brongersma, M. L. *Physical Review Letters* 2007, **99**, 107401.
- [25] Ellis, C. T.; Tischler, J. G.; Glembocki, O. J.; Bezares, F. J.; Giles, A. J.; Kasica, R.; Shirey, L.; Owrutsky, J. C.; Chigrin, D. N.; Caldwell, J. D. *Under review* 2016.
- [26] Giles, A. J.; Dai, S.; Glembocki, O. J.; Kretinin, A. V.; Sun, Z.; Ellis, C. T.; Tischler, J. G.; Taniguchi, T.; Watanabe, K.; Fogler, M. M.; Novoselov, K. S.; Basov, D. N.; Caldwell, J. D. *Under review* 2016.
- [27] Spann, B. T.; Compton, R.; Ratchford, D.; Long, J. P.; Dunkelberger, A. D.; Klein, P. B.; Giles, A. J.; Caldwell, J. D.; Owrutsky, J. C. *Physical Review B* 2016, **93**, (8), 085205.
- [28] Caldwell, J. D.; Novoselov, K. S. *Nature Materials* 2015, **14**, 364.

Visualization of Invisible Defects in Semiconductor Devices

Kyoichiro Asayama

EM Business Unit, JEOL Ltd.

The failure analysis of semiconductor devices using an electron microscope plays a wide role from the yield improvement in the mass production factory to assurance of the long-term reliability in the market. In the failure analysis of the semiconductor devices, defects sometimes cannot be specified from the ordinary imaging and analysis techniques, even though the cause of failure is logically confirmed by electric diagnosis. Such cause of failure is called “invisible defect” in this article. However, possibility to visualize some of the defects becomes attainable by a recent advanced performance of an electron microscope and the progress of analysis technique. Here I would like to introduce an approach to the dopant and strain issue from these topics. Accompanying with proceeding high precision and high performance of semiconductor devices, the instability, unevenness and deterioration of electrical properties have been actualized. The invisible defects are assumed in many models as an origin of these failures in the current stage. To verify grounds of a failure model, I present some defects that are expected to be visualized in the future.

Introduction

Moore's law [1] was a guiding principle in the development of semiconductor device and process, though this situation has been changing in recent years. The principle of miniaturization does not accord with the reality of the device. The scaling law of semiconductor device has not been held for long [2]. However, the instability of the device and the reliability issue become more serious as a result of high integration and miniaturization of the semiconductor devices. Therefore researchers search for the compromise point to compensate the issue of miniaturization by using various exotic materials, new structures, and additive doping elements. But in many cases, the effects and the grounds of those trials are not clear. Actually the device failure increases if we use an unstable material or adopt an uncertain ground. Certain countermeasures are necessary for this situation. Hereafter, it will be necessary to ensure the reliability based on a convinced physics based grounds so that the semiconductor device can be widely used in the world as trustworthy electronic parts. The various interactions of the electron beam and the material are utilized skillfully in electron microscopy. Electron microscope is the analytical equipment appropriate for failure analysis of the semiconductor devices. After all, the analysis by electron microscopy will give the basis for reliability.

Some attempts to visualize invisible defects

Even when the failure analysis is carried out for

semiconductor devices, a corresponding defect is sometimes not found. This defect will be called an invisible defect. There might be a lot of defects that can be visualized by a current technical breakthrough. **Table 1** shows the techniques to visualize such defects. The observations of chemical-bonding state by EELS (Electron Energy Loss Spectroscopy) [3] and three dimension imaging [4] brought a lot of useful information. On the other hand, the measurement of the permittivity [5] is difficult and only few examples were reported [6].

Analytical visualization of dopant impurity

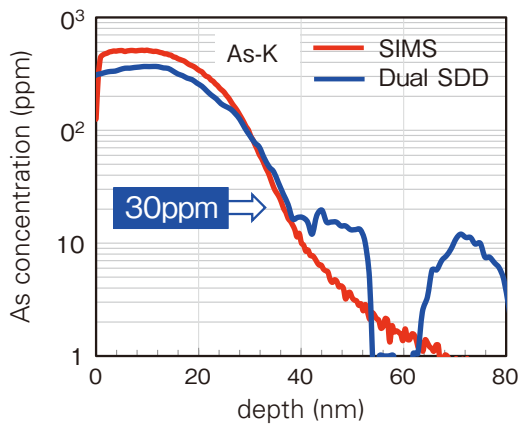
As for impurities of the semiconductor device, the arsenic and boron are used as a dopant. The density is about 1×10^{13} to $1 \times 10^{20} \text{cm}^{-3}$. This density is too low to be analyzed by the electron microscope. The analysis sensitivity of the electron microscope has been improved using the spherical aberration correction system [7, 8] and SDD (Silicon Drift Detector). As a result, the analysis of the dopant in a real device becomes possible [9]. **Figure 1** shows the example of analyzing the n-type dopant of arsenic. The detection limit ensures the analysis of the dopant densities in the diffusion layer of about $1.5 \times 10^{18} \text{cm}^{-3}$ (30 ppm) except in the Well layer.

This type of measurement is applied to the boron of p-type dopant [10]. If a target area is a high density area such as the source and drain area, the presence level of the dopant atom can be confirmed [11]. The MCR (Multivariate Curve Resolution) method that was a kind of the multivariate analysis was applied to the EELS spectrum analysis with higher sensitivity [12, 13]. The dopant density of boron implanted in the Si substrate is

Table 1 Visualized defects in the semiconductor devices.

| | technique | application |
|------------------------------|--|---|
| Chemical binding information | TEM-EELS + Multivariate analysis | oxide, nitride composition ratio in 1nm ² area |
| Strain (device · crystal) | NBD, CBED STEM-Moire, LAADF Image | strain(0.02~1%) strain distribution image |
| permittivity | Low loss spectrum, Kramers-Kronig analysis | Permittivity isolation film, Low-K, High-K |
| 3D Imaging | Tomography imaging FIB-SEM slice & view | wiring, Via, gate electrode, gate edge line roughness, crystal defect, dislocation |
| Dopant | High sensitivity analysis (+ multivariate analysis) Electron holography | diffusion area (2×10 ¹⁸ cm ⁻³ ~) leak current, current failure of MOS transistor |

Fig. 1 Depth profile of arsenic concentration by EDS.



The profile measured for 70 minutes with the Dual SDD detector of EDS is overlaid with the data by SIMS. Detection limit of arsenic dopant is about $1.5 \times 10^{18} \text{cm}^{-3}$ (30 ppm).

shown in Fig. 2. The boron edge was confirmed to be located at 189 eV as a result of applying the MCR method to the EELS spectrum. The detection limit of boron is about $5 \times 10^{19} \text{cm}^{-3}$ (1,000 ppm) as shown in Fig. 3.

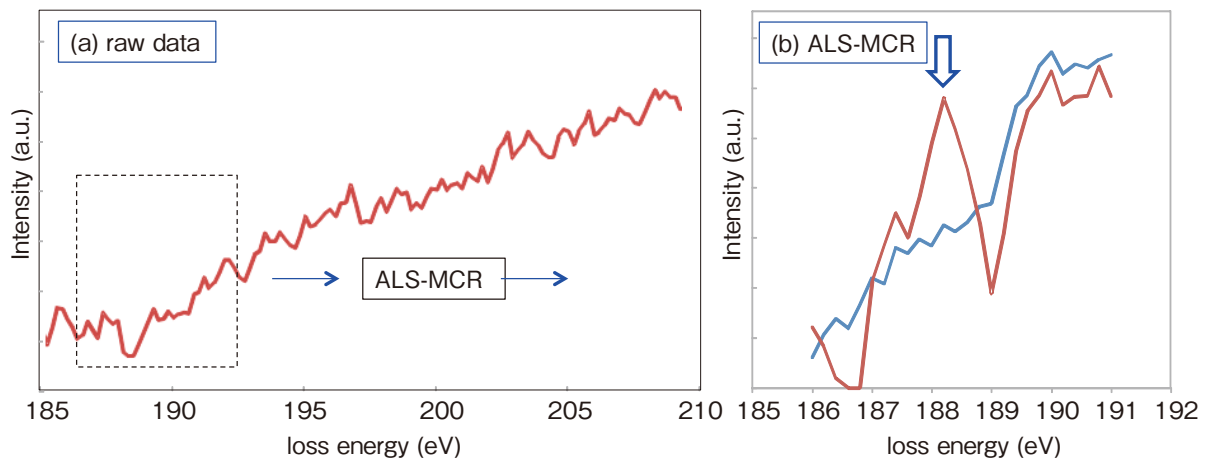
Direct imaging of dopant atom

Visualization of the contrast of the dopant atom has been attempted. The high resolution image of Si substrate that implanted arsenic is shown in Fig. 4. The contrast of the arsenic atom was confirmed from this image [14]. As for the contrast of the atom, the possibilities of antimony (As) [15], the lithium (Li) [16], and hydrogen (H) [17], etc., were suggested. Various kinds of impurity atoms doped to the semiconductor devices are listed in Table 2. The purpose of impurity atom in the semiconductor devices is diverse.

Visualization of strain

The strained silicon is used for the high-speed operation and the low power consumption of the semiconductor device [18].

Fig. 2 Boron dopant detection by EELS with multivariate analysis.



(a) EELS raw data of the Si substrate including boron dopant. There is no edge of boron in the raw data of EELS spectrum from a boron doped sample. The part in the dotted square was analyzed by MCR.
 (b) EELS spectrum of the boron edge processed by the multivariate analysis (ALS-MCR). Another peak can be attributed to the element involved in the Si substrate.

As for the measuring methods of the strain, there are CBED (Convergent Beam Electron Diffraction) [19], NBD (Nano Beam Diffraction) [20], the dark field electron holography [21], and high resolution TEM image [22], etc. Recently, the STEM (Scanning Transmission Electron Microscopy) moire method has been developed [23], and it was applied to the strain measurement of the semiconductor devices [24]. **Figure 5** shows the example of applying the GPA (Geometrical Phase Analysis) method to high resolution TEM image of InGaN/GaN. GPA is a method of strain analysis assuming that the difference of the lattice spacing is regarded as a phase change. It was found that the strain of 3% or less is caused by the addition of indium.

Visualization of defect will be needed in the future

TDDDB (Time Dependent Dioxide Breakdown)

The cause of the initial failure of the gate oxide thin film is often a particle or contamination. **Figure 6** shows an example of the failure of gate oxide. The cause of leakage current failure of gate insulating film after long time uses is not clear. **Figure 7** shows the percolation model that is one of the failure models. A trap, an interface state and a fixed charge in the insulating film, has not been visualized so far.

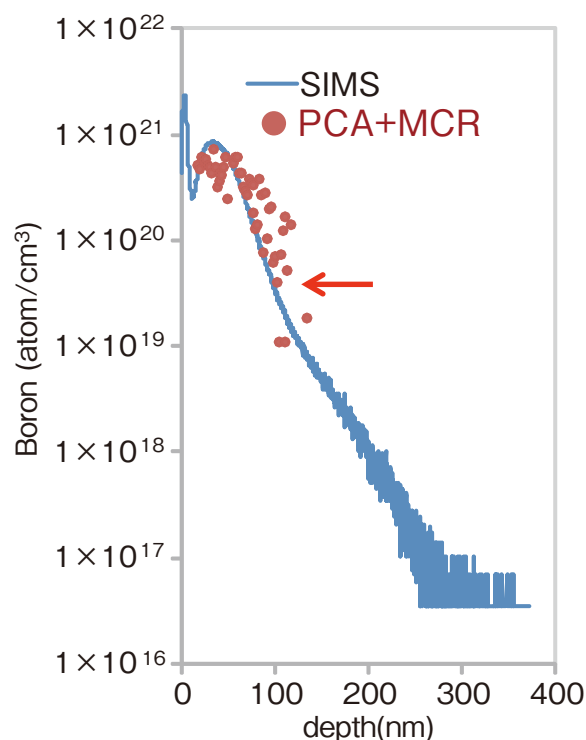
Scatter of device characteristics (Dopant Fluctuation)

The gate area per one MOS transistor decreases as shown in **Fig. 8**. Number of the dopant atoms per one MOS transistor is different. As a result, the current of MOS transistor is fluctuated [27].

Instability of MOS transistor (Random Telegraph Noise)

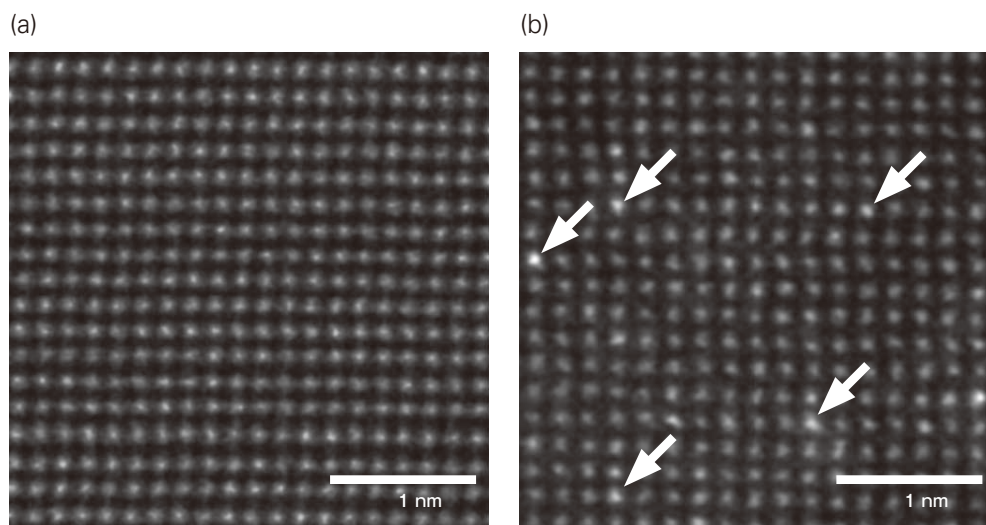
The phenomenon of changing in the threshold voltage of

Fig. 3 Detection limit of the boron dopant in the EELS spectrum processed by the multivariate analysis.



The boron doped sample was measured by STEM-EELS and SIMS. The ALS-MCR method was applied to estimate the detection limit, after noise reduction (PCA), background removal (Power-law model), and multiple scattering removal (Fourier ratio deconvolution).

Fig. 4 Contrast of the Si atomic column including arsenic atom.

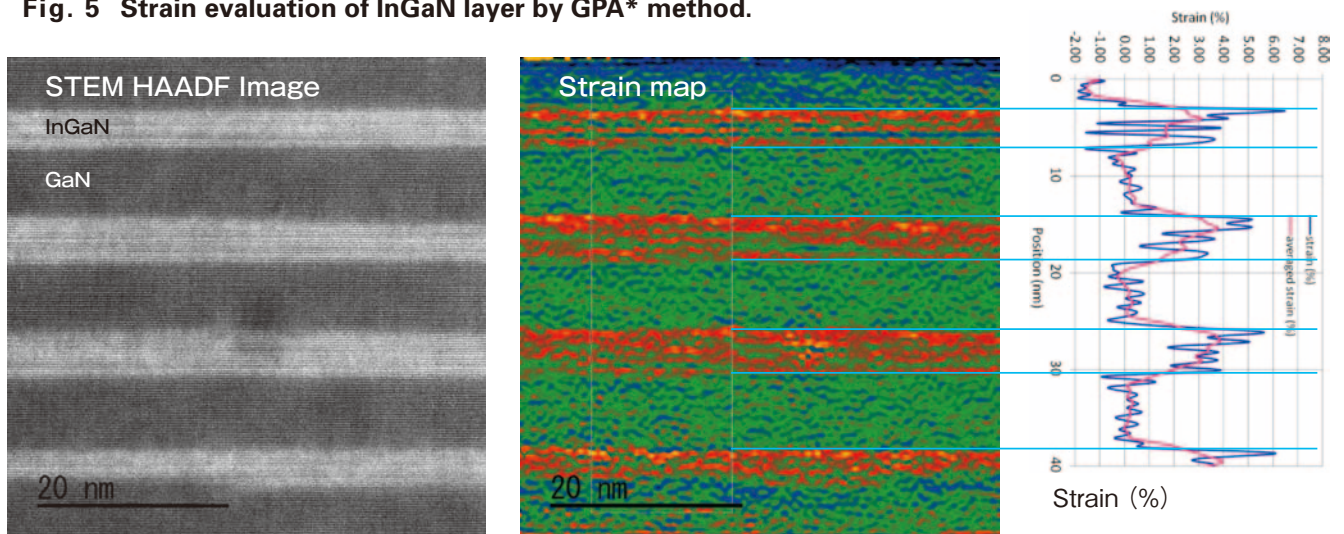


When the incident electron beam propagates along the atomic column which includes another atom, that column shows different contrast compared to the surroundings.
 (a) No arsenic dopant in the Si substrate. The contrast of any atomic column is the same.
 (b) High resolution image of the arsenic doped ($1 \times 10^{15} \text{cm}^{-2}$, 30 kV) Si substrate. The contrasts of the atomic columns indicated by arrows are higher than the surroundings. These atomic columns are considered to include one or more arsenic atoms.

Table 2 Minor elements doped in the semiconductor devices as a target of visualization.

| elements | type | doped area | purpose | failure | concentration(cm ⁻³) |
|------------|------|--|--|---|-------------------------------------|
| As | N | NMOS S/D NMOS extension PMOS enhancement | Vth, Ids control NMOS field relaxation Vth control | NMOS Vth, Ids failure short channel effect Ids leak | 1E18 ~ 5E20 |
| P | N | NMOS S/D N type PolySi N Well | Vth, Ids control gate electrode resistance PMOS junction | NMOS Vth, Ids failure gate depletion Vth increase, leak current | 1E13 ~ 5E20 |
| Sb | N | PMOS Halo N Buried Layer | PMOS Vth control NMOS capacitance | NMOS Vth failure NMOS parasitic capacitance | 1E19~ |
| B | P | PMOS S/D PMOS extension P Well | Vth, Ids control PMOS field relaxation NMOS junction | PMOS Vth, Ids failure short channel effect leak current | 1E13 ~ 5E20 |
| In | P | NMOS Halo | NMOS Vth control | NMOS Vth failure | 1E19~ |
| N | | insulation film interface of Si substrate | SiON gate insulation film decrease interface charge | break down voltage PMOS NBTI | 1E18 ~ 1E21 |
| F | | solid solution of Boron | PMOS resistance decrease interface charge termination of dangling bond | PMOS Ids decrease PMOS NBTI | 1E18 ~ 5E20 |
| Ge | | SiGe stressor | increase mobility | S-D leak by Ge diffusion | a few atoms |
| La (Zr) | | gate insulation film Hi-K gate material | Vth control ϕ_M | Vth shift, leak current | a few atoms ~ crystallization |
| Hf | | gate insulation film Hi-K gate material | permittivity improvement | TDDDB deterioration by Hf diffusion | a few atoms ~ crystallization |
| C | N? | near Extension | dopant profile control diffusion stopper | ? | 1E19 ~ 5E20 |
| O | | depth 500nm~20 μ m | anti contamination impurity gettering | leak current increase contamination Vth, Ids failure | 1E19 ~ precipitate |

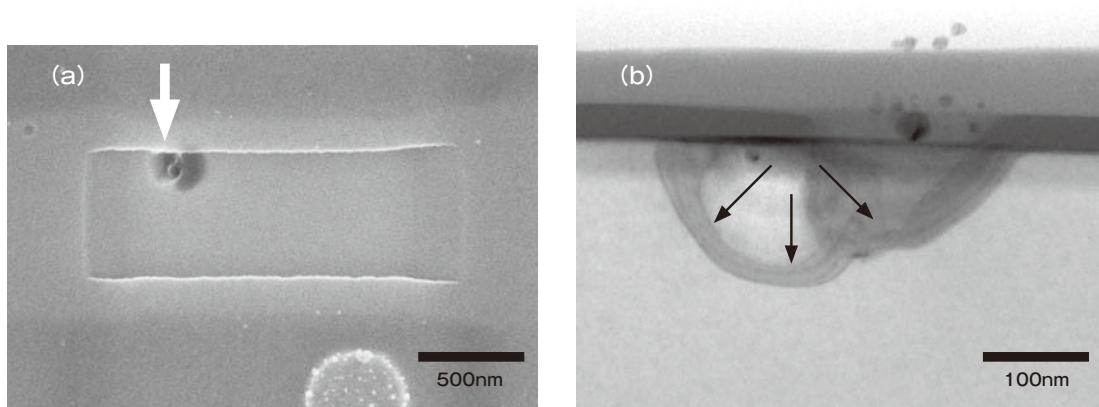
Fig. 5 Strain evaluation of InGaN layer by GPA* method.



The lattice strain in a local area was visualized by the GPA method which indicates a variation of the lattice spacing directly in the high resolution image of InGaN/GaN layer. The shift of the atomic location due to the addition of In is extracted by comparing the atomic location of pure-GaN. The phase shift is measured and analyzed similar to the electron holography.

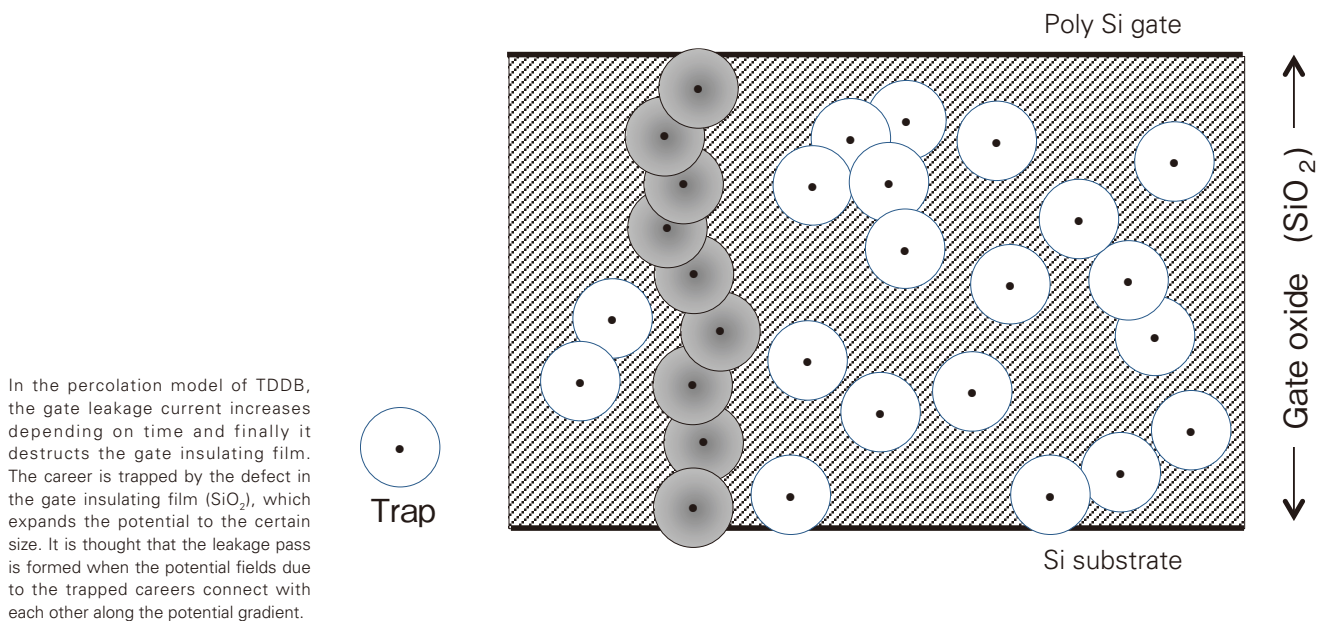
*GPA: Geometrical Phase Analysis

Fig. 6 Failure analysis of early stage in TDDB (analytical example of gate pin-hole).



(a) The early stage failure of TDDB is detected as a gate pin-hole by the failure analysis. In this case the thinning of gate insulating film is considered to be caused by a particle.
 (b) The cross sectional TEM image of (a). The isotropic cave is observed in the Si substrate. This cave was formed by the wet etching which actualizes the gate pin-hole for SEM observation.

Fig. 7 Mechanism of TDDB failure by the percolation model.



the MOS transistor is called RTN (Random Telegraph Noise) [28, 29]. It is believed that the phenomenon is due to charges in defects in the gate insulating film which repeat release and capture (Fig. 9). However, the defects in the insulating film, which are classified into multiple species have not yet been observed [30, 31].

Time depending deterioration (NBTI: Negative Bias Temperature Instability)

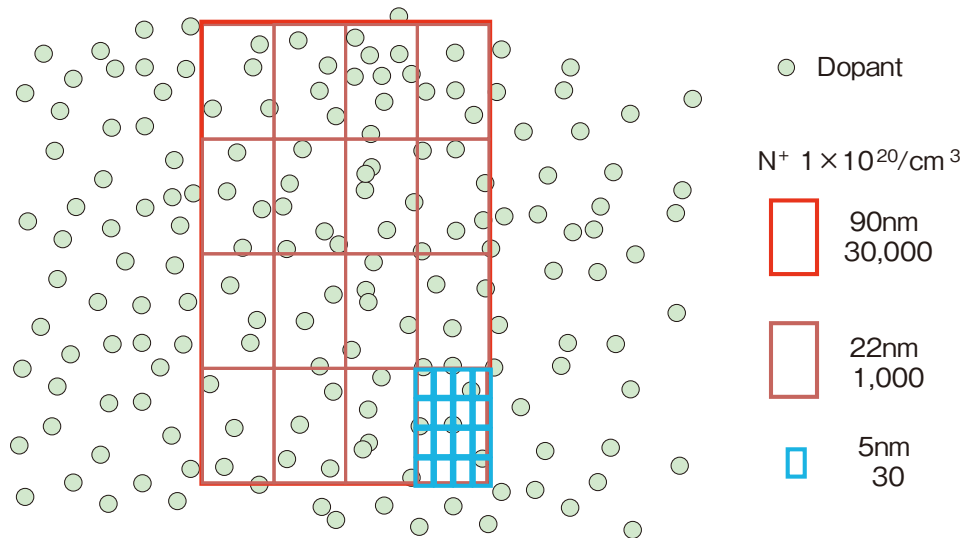
The rise of the threshold voltage and the decrease of the current arise under the negative bias and high temperature PMOS operation. “Reaction Diffusion Model” [32] and “Trap-Deptrap Model” [33] are proposed to explain the cause. According to the

measurement of ESR (Electron Spin Resonance Spectroscopy), the states that exist in the interface of the Si substrate and the insulating film seem to be the cause [34].

Deterioration of Flash memory

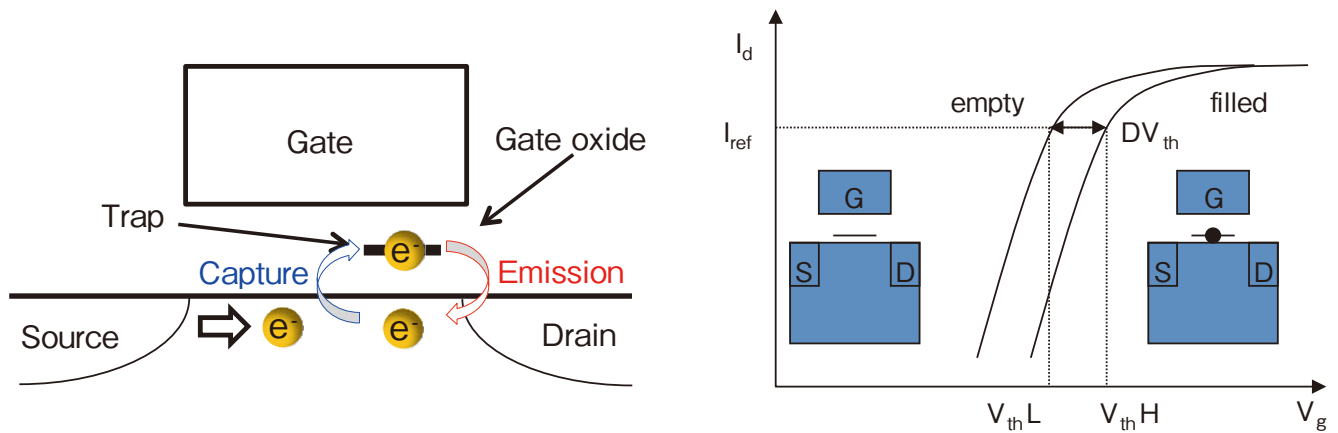
The reading and writing mechanism of the flash memory is that the accelerated electrons into high energies go back and forth through the gate insulating film for charging and discharging. The insulating film is deteriorated by the penetration of high energy electrons. Such electron movement is considered to cause deterioration of the bonding state and an increase the dangling bonds at the interface between the Si substrate and the gate insulating film [35].

Fig. 8 Dopant fluctuation.



The number of dopants per device is decreased according to the miniaturization in the design rule. As a result, the fluctuation of the dopant hidden in the statistical error is actualized.

Fig. 9 RTN (Random Telegraph Noise).



The threshold bias voltage (V_{th}) rises when the defect (energy levels) in the gate insulating film captures a carrier. V_{th} returns to the former value when the carrier is discharged. Since this V_{th} shift is repeated at random, it is called RTN.

In the future semiconductor devices, the visualization of the defects listed in **Table 3** will be needed. In this table, there are many defects of different types, i.e., dangling bonds, hydrogen atoms, point defects, fixed charge, interface level and chemical bonding state, and the visualization of them is difficult by using a current electron microscope. There is a place to look forward to future development.

Conclusion

In the failure analysis of the semiconductor devices, failure cause is not clarified only by the ordinary observation and the analysis. In this article, I introduced the method of visualizing the

invisible defects such as dopant and strain. In future the scatter and instability of the devices are expected to be actualized. And visualization of the defects is significantly requested. The reliability, quality, and yield of the semiconductor devices will be improved along with the development of advanced methods to visualize the invisible defects.

Acknowledgement

This article includes contents already published by the author who was engaged in Renesas Electronics Ltd. Some parts of this article are attributed to the joint research with OSAKA Univ. and Tokyo Institute of Technology. The author wishes to

Table 3 Defects in the semiconductor devices to be visualized in the future.

| defects | technique | phenomenon of semiconductor |
|--|---|--|
| atomic position (dopant, C, F, N) | ultra thin film sample high resolution imaging geometric phase analysis(GPA) cathodoluminescence | impurity in the transistor point defect, dislocation dopant fluctuation |
| point defect cluster defect | | trap-detrapp model, RTN ionization rate of dopant |
| defect , trap in insulation film dangling bond interface energy level fixed charge | high energy resolution EELS Multivariate analysis (MCR) electron holography ionized contrast | transistor instability (RTN) TDDB NBTI mechanism flash memory deterioration |

thank Dr. S. Muto, professor Nagoya University for guidance of multivariate analysis. The author also wishes to thank Dr. E. Murakami, professor Kyushu Sangyo University and Dr. Y. Oshima, associate professor JAIST for the stimulating discussion. Ms. M. Morita, University of Tokyo offered some observation samples and data for this article.

References

- [1] G. Moore: "Cramming more components onto integrated circuits", Electronics Magazine, Mcgraw-Hill, New York (1965).
- [2] R. H. Dennard: *IEEE J.of SSC*, **9-5**,256 (1974).
- [3] K. Kimoto, T. Sekiguchi and T. Aoyama: *J.Electron Microsc.*,**46**, 369 (1997).
- [4] K. Asayama, Y. Kato, T. Fujii, K. Yoshida, A. Takaoka and H. Mori: Proc.16th Int. Microscopy Congr.,Sapporo,1441 (2006).
- [5] R. F. Egerton: "Electron Energy-loss Spectroscopy in the Electron Microscope", Springer, New York (2011).
- [6] Y. Anan, M. Koguchi, K. Asayama, K. Kimoto, and Y. Matsu: *Kenbikyo* **44**, 227 (2009).
- [7] O. Scherzer, "The theoretical resolution limit of the electron microscope", *J. Appl. Phys.* **20**, 20 (1949).
- [8] M. Haider et al., "Electron microscopy image enhanced", *Nature* **392**, 768 (1998).
- [9] K. Fukunaga, N. Endo, M. Suzuki and Y. Kondo: *Microsc.Microanal.***21-3**, p0412 (2015).
- [10] T. Sato, Y. Suzuki, H. Matsumoto, T. Hashimoto, K. Nakamura, T. Miura and H. Yoshida: *Microsc.Microanal.* **21-3**, p1005 (2015).
- [11] K. Asayama, N. Hashikawa, K. Kajiwara, T. Yaguchi, M. Konno and H. Mori: *Appl. Phys. Express*, **1**, 074001 (2008).
- [12] S. Muto, T. Yoshida and K. Tatsumi: *Mater. Trans.*, **50**, 964 (2009).
- [13] S. Muto: *Kenbikyo* **46**, 24 (2011).
- [14] Y. Oshima, Y. Hashimoto, Y. Tanishiro and K. Takayanagi, H. Sawada, T. Kaneyama and Y. Kondo, N. Hashikawa and K. Asayama: *Phys.Rev.***B81**, 035317 (2010).
- [15] S. Kim, Y. Oshima, H. Sawada, N. Hashikawa, K. Asayama, T. Kaneyama, Y. Kondo, Y. Tanishiro and K. Takayanagi: *Appl. Phys. Express* **3**, 081301 (2010).
- [16] Y. Oshima, H. Sawada, F. Hosokawa, E. Okunishi, T. Kaneyama, Y. Kondo, S. Niitaka, H. Takagi, Y. Tanishiro and K. Takayanagi: *Microscopy* **59-6**, 457 (2010).
- [17] S. D. Findlay, T. Saito, N. Shibata, Y. Sato, J. Matsuda, K. Asano, E. Akiba, T. Hirayama, and Y. Ikuhara: *Appl. Phys. Express* **3**, 116603, (2010).
- [18] D. K. Nayak, J. C. Woo, J. S. Park, K. L. Wang and K. P. MacWilliams: *Appl.Phys.Lett.*, **62(22)**, 2853 (1993).
- [19] K. Usuda, T. Numata, T. Irisawa, N. Hirashita, and S. Takagi: *Mat.Sci.Eng.B*, **124**, 143 (2005).
- [20] K. Tsuda, Ha. Mitsuishi, M. Terauchi, and K. Kawamura: *J.Electron.Microsc.*, **56(2)**, 57 (2007).
- [21] M. J. Hytch, F. Houdellier, F. Hue and E. Snoeck: *Nature*, **453**, 1086 (2008).
- [22] M. J. Hytch, E. Snoeck and R. Kilaas: *Ultramicroscopy*, **74**, 131 (1998).
- [23] Y. Kondo, N. Endo: *Kenbikyo* **49**, 226 (2014).
- [24] S. Kim, S. Lee, Y. Oshima, Y. Kondo, E. Okunishi, N. Endo, J. Jung, G. Byun, S. Lee and K. Lee: *Appl.Phys. Lett.*,**102**,161604 (2013).
- [25] R. Degraeve, G. Groeseneken, R. Bellens, J. L. Ogier, M. Depas, P. J. Roussel, and H. E. Maes, "New Insights in the Relation between Electron Trap Generation and the Statistical Properties of Oxide Breakdown," *IEEE Trans. Electron Devices*, **45**, 904 (1998).
- [26] J. H. Stathis, "Percolation Model for Gate Oxide Breakdown," *J. Appl. Phys.*, **86**, 5757 (1999).
- [27] F. L. Yang, J. R. Hwang, H. M. Chen, J. J. Shen, S. M. Yu, Y. Li and D. D. Tang: Symposium on VLSI Technology Digest Of Technical Papers, **11B-3**, 208 (2007).
- [28] S. Realov, et al. International Electron Devices Meeting 2010. San Francisco, CA, USA, 2010-12, IEEE.2010, 28.2.1 (2010).
- [29] T. Nagumo et al. International Electron Devices Meeting 2010. San Francisco, CA, USA, 2010-12, IEEE., 28.3.1 (2011).
- [30] S. M. Joe, et al. *IEEE Trans.Electron Devices*, **58**.1.67 (2011).
- [31] M. Schulz: *J.Appl.Phys*,**74**, 4, 2649 (1993).
- [32] M. A. Alam, H. Kufluoglu, D.Varghese, S. Mahapatra: *Microelectron. Reliab.* **47**, 853 (2007).
- [33] H. Reisinger, T. Grasser, W. Gustin and C. Schlunder: Proc.IEEE Int.Rel.Phys.Symp. 2A.1.1 (2010).
- [34] J. P. Campbell, P. M. Lenahan, C. J. Cochrane, A. T. Krishnan, S. Krishnan: *IEEE Trans. Device and Material Reliability*, **7-4**, 540 (2007).
- [35] Van den Bosch, G. et al.: IEEE International Memory Workshop (IMW2009). Monterey, CA, USA, IEEE., 84 (2009).

Development of Cryo-Coil MAS Probe for Multinuclear Measurement

Takashi Mizuno JEOL RESONANCE Inc.

A Cryo-Coil MAS Probe for multinuclear measurement was developed. This innovative probe achieves a sensitivity improvement of up to 4.5 times that of a normal NMR probe and expands the measurement efficiency (throughput) to 20 times or larger. This achievement is made by cooling the detection system while spinning the sample with high speed at around room temperature. The Cryo-Coil MAS Probe is expected to become a frontier tool for new applications mainly for high-resolution NMR measurement of various inorganic materials, which was conventionally difficult with the NMR system because inorganic-material measurement provides low sensitivity and requires long measurement time.

Introduction

In 1958, the Magic Angle Spinning (MAS) method was developed by Andrew et al., which pioneered to realize High-Resolution Solid-State Nuclear Magnetic Resonance (NMR) spectroscopy, since then, about 60 years have passed[1]. NMR uses lowest energy ranges of electromagnetic waves among various spectroscopic methods, and its sensitivity is very low. In particular for Solid-State NMR, technological innovation for enhanced sensitivity is potentially demanded because multinuclear measurement of substances (e.g. inorganic materials) is highly requested for this NMR technique. A great deal of researchers and engineers have strived to make efforts to increase NMR sensitivity for incessantly creating new markets.

Up to now, research and development of sensitivity enhancement of NMR has been primarily promoted by the development of Super Conducting Magnet (SCM) which corresponds to an external field for NMR signal. On the other hand, another different approach has been attracting attention, that is, the development of NMR probes that correspond to the first-stage of the NMR signal detection system. In general, an NMR signal is detected as a high-frequency induced electromotive force that is generated in a detection coil (near a sample) due to macroscopic nuclear magnetization in the sample. Thus, it could be easily thought that when the detection circuit is placed at a ultra-low temperature environment and the metal resistance of the detection coil is lowered to reduce thermal noise of the coil, the signal-to-noise ratio (S/N ratio) of the detection circuit is improved compared to when placed at a room temperature environment. The theory of improved S/N ratio with “NMR Probe with cryogenic-detection system”

was quantitatively estimated by Hoult et al., for the first time in 1976 [2]. In 1980s, for Liquid-State NMR, experimental studies of a practical “NMR Probe with cryogenic-detection system,” in which the first-stage high-frequency circuit was encapsulated in a cryostat for NMR measurement of a sample at room temperature, have been started [3]. Also in 1980s, it is worthy to note that as an epoch making event for realizing this innovative NMR probe, an HEMT (high-electron-mobility transistor) device, which is made of GaAs semiconductor, was put into practical use, leading to the development of a low-temperature, low-noise amplifier for radio waves to micro waves in the radio astronomy field. This revolutionized amplifier has a noise temperature of as low as 20K or below [4]. Utilizing these achievements, in 1990s to 2000s, the patents of “NMR Probe with cryogenic-detection system” for Liquid-State NMR were applied one after the other [5]. Up until now, this probe achieves a sensitivity improvement of 4 to 6 times that of the equivalent room-temperature probe. Thus, as is well known, this probe with cryogenic detection system is practically used in a wide range of fields [6].

Viewing from the entire NMR system, a major advantage of the “NMR Probe with cryogenic-detection system” is that the mechanism of sensitivity improvement depends only on simple physical phenomena (electromagnetic induction and thermal noise) and therefore, this mechanism acts cumulatively on the other sensitivity-improvement methods. For example, when applying the probe with cryogenic detection system to a high field NMR magnet, more improved sensitivity is expected compared to when using a normal NMR probe with the same magnet. Accordingly, this technological benefit should have been promptly utilized for Solid-State NMR.

However in fact, the development of the “NMR Probe with cryogenic-detection system” for High-Resolution Solid-State NMR, that is, “Cryo-Coil MAS Probe” was behind with that for Liquid-State NMR. The reason is that MAS at room temperature is essential for Solid-State NMR and this was a big challenge. To realize MAS, it is absolutely necessary to place detection coil at ultra-low temperature while keeping a space at room temperature, where both a sample bore with a tilt of 54.74° from the static magnetic field direction and a built-in sample spinning system are maintained. However, in order to implement this work in a limited space in the normal NMR magnetic field, it was estimated to be difficult in terms of mechanical designing. In addition, a high-power RF field of 100 W or larger is often needed for Solid-State NMR, but this task was estimated to have a difficulty. This is due to the fact that, when trying to create high-frequency circuits that are resistant to such a high-power RF field and stably operate at low temperature, designing of electrical and vacuum systems is very difficult. Mainly owing to these reasons, it was considered that the development of a Cryo-Coil MAS Probe was rather far from implementation among researchers and engineers (e.g. NMR manufactures).

In 2005, our NMR R&D team started a joint research with Professor Kiyonori Takegoshi of Kyoto University who addressed, that we should endeavor to complete this difficult task. Our joint research on basic research of a Cryo-Coil MAS Probe for multinuclear measurement was launched as a project of “Fundamental technology to realize high-sensitive Solid-State NMR for multinuclear measurement” supported by Japan Science and Technology Agency (Core Research for Evolutional Science and Technology (CREST) programs). The outline of the research and development of the probe is described in this paper.

Instrument

Firstly, the principle of sensitivity improvement of the Cryo-Coil MAS Probe is explained.

In the normal NMR probe for which observation frequencies are several MHz to several hundreds of MHz, the physical substance of NMR signal means high-frequency electromotive force induced by electric charges in the conductor of detection coil, which are coupled with near fields produced by nuclear magnetic dipoles in a sample. On the other hand, the major noise in those observation frequencies is the Johnson noise (thermal noise) that originates from fluctuations of phonons in the conductor of detection coil. This thermal noise possesses a constant intensity (white noise) irrespective of carrier frequencies. In addition, an NMR signal often is extremely small (~microvolt), so that amplification of the signal with a preamplifier is required while the additional noise from the preamplifier is obtained. If all of these factors are packaged, the equation for the S/N ratio of an NMR spectrum is given by the following one.

$$\frac{V_S}{V_N} = M_0 \sin \theta_m \sqrt{\frac{Q_c \mu_0 \eta_f v_s \omega_0}{4k_B(T_c + T_a) \Delta f}}$$

The definitions of each parameter are as follows.

- V_S Electromotive force of NMR signal originating from detected nuclear spins (unit: voltage).
- V_N Total sum of the noise electromotive force ranging from the detection coil to preamplifier output (unit: voltage).
- M_0 Thermal equilibrium magnetization induced by nuclear spins per unit volume.
- θ_m Angle between the coil axis and the static magnetic field

direction.

(In the case of High-Resolution Solid-state NMR, the magic angle is ~ 54.7°.)

- μ_0 Magnetic permeability of vacuum.
- v_s Sample volume.
- ω_0 Larmor frequency of nuclear spins in the relevant static magnetic field.
- k_B Boltzmann constant.
- Δf Observation frequency width.
- Q_c Q value of the detection coil.
- η_f Filing factor: Ratio of the spatial integral dominated by the sample to the total spatial integral of the magnetic field strength produced by detection coil (in the case of the solenoid coil, this factor is simply expressed by the ratio of the cylinder volume in the coil to the sample volume).
- T_c Real temperature of the conductor of detection coil.
- T_a Noise temperature of the preamplifier.

For example, the temperature of the conductor of detection coil (T_c) is around room temperature (~ 300K). If T_c is set to 3K (note that the additional noise of the preamplifier is not taken into consideration), the S/N ratio improves to as high as $\sqrt{(300/3)} = 10$ times even when the other parameters are not changed. That is, this temperature (T_c) is of prime importance for the S/N ratio. When the temperature (T_c) is additionally lowered, the conductor resistance is also lowered; therefore Q_c ; which corresponds to the detection efficiency of the coil is increased to 4 to 5 times that at room temperature. At that time, the lowered noise temperature of the amplifier (T_a) contributes also to the improvement of the detection sensitivity.

In order to spin the sample with high speed at around room temperature, there needs a space where thermal insulation between the sample and the detection coil is enabled. In this case, although the filing factor should be smaller, it becomes possible to enhance the total sensitivity if the gain exceeds that filing factor. Owing to these effects, it is estimated that a sensitivity enhancement of 4.5 times is obtained relatively.

Secondly, the outline of the probe construction and its features are described. **Fig. 1** shows the external view of a manufactured (prototype) Cryo-Coil MAS Probe for multinuclear measurement. Up to now, seven prototype probes have been completed. We have been enhancing the technological capabilities of the Cryo-Coil MAS Probe with various approaches. Firstly, we examined the sensitivity improvement effect through the cryo-coil methodology by a feasibility study [7]. Along with the increased number of the manufactured probes, we have tried to take multinuclear measurements. Those include designing of efficient cooling, pursuit of mechanical precision applicable to shrinkage of the probe materials due to the temperature difference, development of discharge-resistant technologies for irradiation of high-power RF field [8] and optimization of the filing filter.

The presently manufactured prototype Cryo-Coil MAS Probe for multinuclear measurement is a single-tuned NMR probe that adopts a balancing circuit for tuning of the detection coil, applicable to a wide-bore magnet whose magnetic field ranges from 9.4T to 14T. A series of the prototype probes are equipped with a tunable system for exchanging the capacitor in the tuning circuit of the detection coil even at low-temperature operation. The tuning range of a prototype NMR probe reaches 70 MHz to 190 MHz (for the fifth prototype) and 30 MHz to 70 MHz (for the sixth prototype).

In order to explain the present prototype probe, **Fig. 2** shows

a cross sectional view of the probe main body and the top of the probe. This probe is applicable to a wide-bore magnet. The probe is designed in such a way that a series of the outer peripheries is utilized as an insulative partition and the pressure of its internal space is reduced to 1.0×10^{-4} Pa or below, enabling it to function as a cryostat. In the inside of the probe, with the aid of the cooling system described later, a series of detection systems (detection coil, tuning circuits, duplexer (circuits for transmitter & receiver switching), etc.) is connected against a heat exchanger. These cooled parts are placed so that they do not undergo thermal conduction directly from the insulative partition (outer-periphery surface). The detection coil keeps ribbon-like solenoidal shapes on the internal surface of the penetration hole in the insulator block fixed to the heat exchanger. Then the axis of the coil is located along a direction inclined to the magic angle from the axis of the external field. In the inside of the detection coil, there is the cylindrical insulative partition between the coil and the sample space. Through this thin vacuum layer, thermal insulation between the sample and the detection coil is realized. The sample spinning system is placed under atmospheric environment at room temperature,

which is separated by one wall from the detection coil. The sample is spun after encapsulated into a sample tube that is almost the same for a normal Solid-State NMR Probe (maximum spinning speed 18 kHz for a 4 mm diameter sample tube). Precise adjustment of the magic angle is enabled by tilting the entire probe using a unique system in the magic-angle range of $\pm 0.4^\circ$. Furthermore, the use of a top-load system allows easy exchange of sample tube with the NMR probe being installed in the magnetic field.

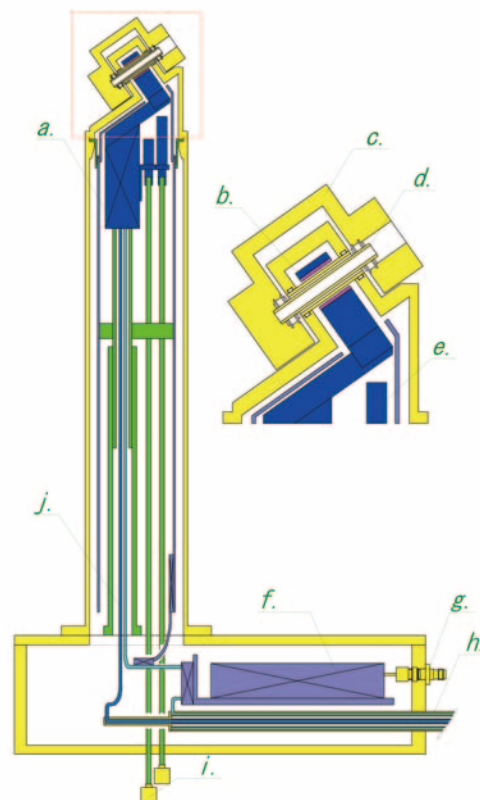
Cooling of the detection system of the Cryo-Coil MAS Probe is carried out with a circulation-type cooling system (Fig. 3). This system consists of a circulator and a refrigerator, and the system forms a closed cycle circuit by combination with pipes via a transfer tube with the Probe. Then, gaseous helium that acts as refrigerant is transferred from the pump outlet of the circulator placed at room temperature. Then in the middle of the transfer, the helium is cooled to 10K by heat exchange via the GM refrigerator. After that, the helium undergoes heat exchange with the cooled parts in the probe while its temperature is increased to room temperature. Finally, the helium is returned to the inlet of the pump. It is necessary to spend approximately

Fig. 1



Photo of the external view of a prototype Cryo-Coil MAS Probe for multinuclear measurement.

Fig. 2



Cross sectional view of the Cryo-Coil MAS Probe for multinuclear measurement. The top section of the probe (framed by red-dashed line) is shown to the right with an enlarged view. Names of each part are as follows. a) Heat exchanger, b) Detection coil and insulator block, c) Sample spinning system, d) Sample tube, e) Part of tuning circuits, f) Duplexer and preamplifier, g) RF input & output port, h) Refrigerant transfer tube, i) Frequency tuning knob, j) Refrigerant pipes. Coloration for each part is applied to different temperatures depending on when each part reaches a thermal equilibrium state. Blue: Room temperature, Light purple: Medium-low temperature, Dark blue: Ultra-low temperature.

6 hours from switching on the GM refrigerator until when the respective cooled parts in the NMR probe reach their lowest temperatures at the relevant portions. It was experimentally verified that after the detection system reaches the lowest temperature, this obtained temperature of the detection system is maintained continuously and stably for 30 days or longer. During that period of days, the consumption volume of helium (refrigerant) is 0 (zero) and also the maximum required power is only 8 kW (equivalent to the consumption power for the GM refrigerator), indicating that the running cost is very low.

Experiments

We performed one-dimensional MAS-NMR measurements so as to confirm the sensitivity-improvement effect offered by the Cryo-Coil MAS Probe. All of the NMR measurements were conducted with a JEOL JNM-ECA600 NMR spectrometer system and a 14T wide-bore magnet (JASTEC) at Professor Takegoshi's laboratory, Department of Chemistry, Graduate School of Science, Kyoto University.

For measurements of ${}^6\text{Li}$ MAS-NMR and ${}^{29}\text{Si}$ MAS-NMR, the fifth-prototype Cryo-Coil MAS Probe for multinuclear measurement was used. For comparison with conventional NMR measurement data, a 600 MHz DSI-1062 (HXY triple resonance MAS probe of Doty) was used. The reason for using this triple resonance probe is that the size and shape of this probe and the Cryo-Coil MAS Probe are the same.

For measurement of ${}^{43}\text{Ca}$ MAS-NMR, which is a low-gamma nucleus, the sixth-prototype Cryo-Coil MAS Probe for multinuclear measurement was used. As for ${}^{43}\text{Ca}$, the comparison was carried where the detection system of the sixth-prototype probe was placed at low temperature and at room

temperature. The fifth and sixth prototype probes were equipped with an in-house low-temperature and low-noise preamplifier. In addition, as a preamplifier for the comparison, N141-305AA (Thamway) was used.

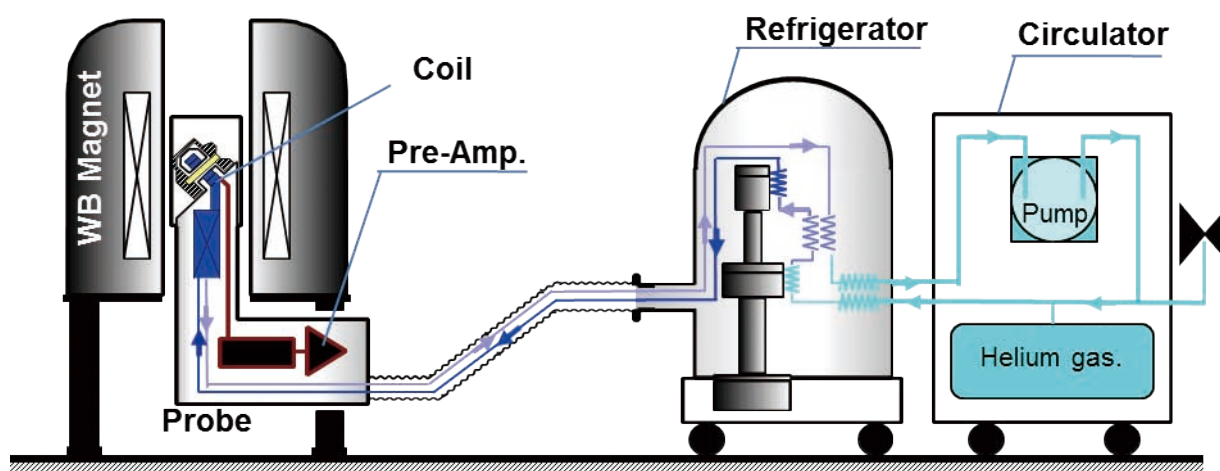
The use of the circulation-type cooling system made it possible to remarkably cool the detection coil for the detection systems in both the fifth-prototype probe and the sixth-prototype probe, with the temperature of these coils down to 17K or lower. For measuring the achieving temperature of those detection systems, light temperature sensors Reflex-1 and T1S-02 (Neoptix) were used.

Results and Discussion

Firstly, NMR measurement of ${}^6\text{Li}$ was conducted, which is contained in lithium cobalt oxide and is used as a positive electrode material. The reason for measuring this nucleus are: 1) Since the magnetic rotation ratio of ${}^6\text{Li}$ is lower compared to that of ${}^7\text{Li}$, dipole interactions with paramagnetic ions become small, 2) Since the quadrupole moment of ${}^6\text{Li}$ is lower compared to that of ${}^7\text{Li}$, the spectral line width of ${}^6\text{Li}$ becomes small and the other reasons. Those features enable one to obtain good conditions for high-resolution NMR observation with an improved sensitivity.

Figure 4 shows two ${}^6\text{Li}$ MAS-NMR spectra acquired with the fifth-prototype Cryo-Coil MAS Probe (a) and with an HXY triple resonance probe (b), where the sizes of the two spectra are compared with the same scale factor. It should be noted that, in order to easily compare the baselines, the two spectra are enlarged. The experimental conditions for both the fifth-prototype Cryo-Coil MAS Probe and the HXY triple resonance probe were as follows. Carrier frequency: 88.30 MHz, Sample: 100% ${}^6\text{Li}$ labeled lithium cobalt oxide (${}^6\text{LiCoO}_2$), Sample

Fig. 3



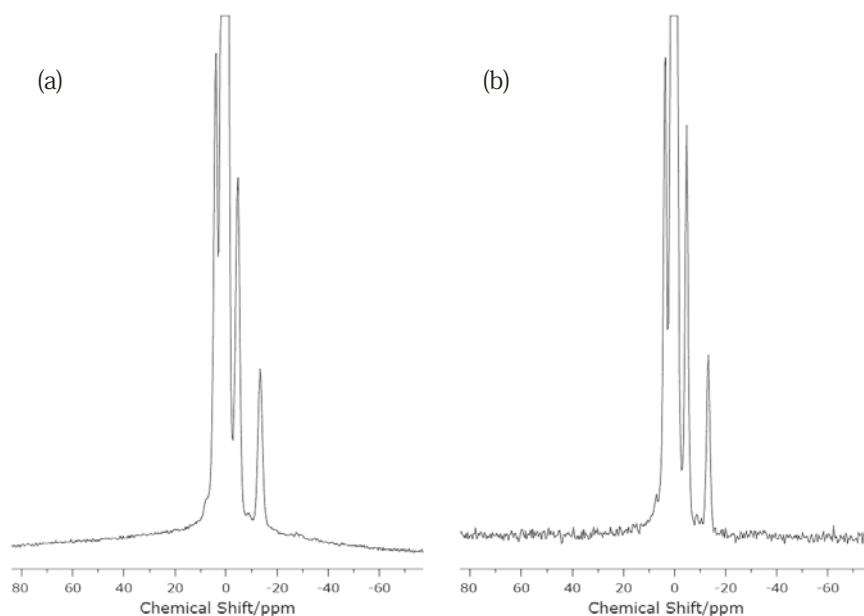
Conceptual diagram of the circulation-type cooling system of the Cryo-Coil MAS Probe. Coloration for each pipe is applied to different temperatures depending on when each pipe reaches a thermal equilibrium state. Blue: Room temperature, Light purple: Medium-low temperature, Dark blue: Ultra-low temperature.

volume: 170 mg, Number of accumulations: 16, Repetition time: 32 s, Sample spinning speed: 17.35 kHz. When comparing the both spectra, the sensitivity improvement ratio for the Cryo-Coil MAS Probe reached 4.40 times. This means that, from the throughput viewpoint, measurement time is drastically reduced by 19.4 times shorter. When attention is focused on around -30 ppm for the ^6Li spectrum, very small peak components which

are not found because of the noise in Fig. 4 (b) are detected in Fig. 4 (a). This peak corresponds to very small components that experienced paramagnetic shift due to a lattice defect contained with a very small amount in lithium cobalt oxide (acting as positive electrode material) [9].

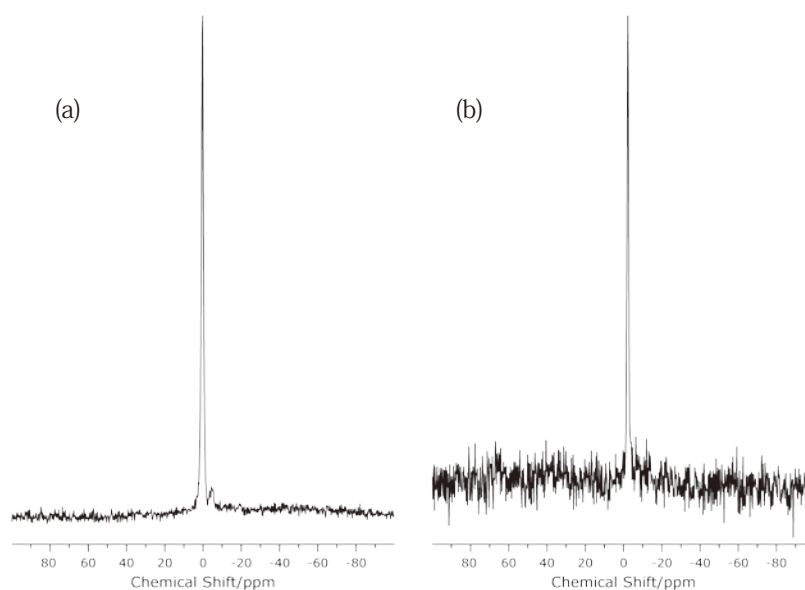
Secondly, in order to present an experiment example for the other nucleus, **Fig. 5** shows two ^{29}Si MAS-NMR spectra

Fig. 4



(a) ^6Li MAS-NMR spectrum of 100% ^6Li labeled lithium cobalt oxide, acquired with the fifth-prototype Cryo-Coil MAS Probe by cooling the detection system.
 (b) For comparison, ^6Li MAS-NMR spectrum of the same sample in (a) under the same experimental conditions was acquired with an HXY triple resonance MAS probe. Pulse sequence for the both spectra is Hahn echo (refocus time: 57 μs). Input power for the both spectra is 88 W. $\pi/2$ pulse width is 3.8 μs for the spectrum in (a) and 7.0 μs for the spectrum in (b).

Fig. 5



(a) ^{29}Si MAS-NMR spectrum of natural abundance LTA zeolite, acquired with the fifth-prototype Cryo-Coil MAS Probe.
 (b) For comparison, ^{29}Si MAS-NMR spectrum of the same sample in (a) under the same experimental conditions was acquired with an HXY triple resonance MAS probe. Pulse sequence for the both spectra is Hahn echo (refocus time: 52.8 μs) for the spectrum in (a) and Single 90° pulse (dead time: 20 μs) for the spectrum in (b). Input power for the both spectra is 105 W. $\pi/2$ pulse width is 4.6 μs for the spectrum in (a) and 6.5 μs for the spectrum in (b).

acquired with the fifth-prototype Cryo-Coil MAS Probe (a) and with an HXY triple resonance MAS probe (b), where the sizes of the two spectra are compared with the same scale factor (with enlargement). The experimental conditions for both the fifth-prototype Cryo-Coil MAS Probe and the HXY triple resonance MAS probe were as follows. Carrier frequency: 118.30 MHz, Sample: natural abundance LTA zeolite ($\text{[Na}_{12}(\text{H}_2\text{O})_{27}]\text{[Al}_{12}\text{Si}_{12}\text{O}_{48}]$), Sample volume: 50.6 mg, Number of accumulations: 100, Repetition time: 22.5 s, Sample spinning speed: 16.58 kHz. When comparing the both spectra, the sensitivity improvement ratio for the Cryo-Coil MAS Probe reached 4.45 times. This means that, from the throughput viewpoint, measurement time is drastically reduced by 19.8 times shorter. When attention is focused on around -5 ppm for the ^{29}Si spectrum, very small peak components which are not found because of the noise in Fig. 5 (b) are clearly detected in Fig. 5 (a). Thus from these two experimental examples, the Cryo-Coil MAS Probe is found to be particularly effective for the measurement of very small components with small content.

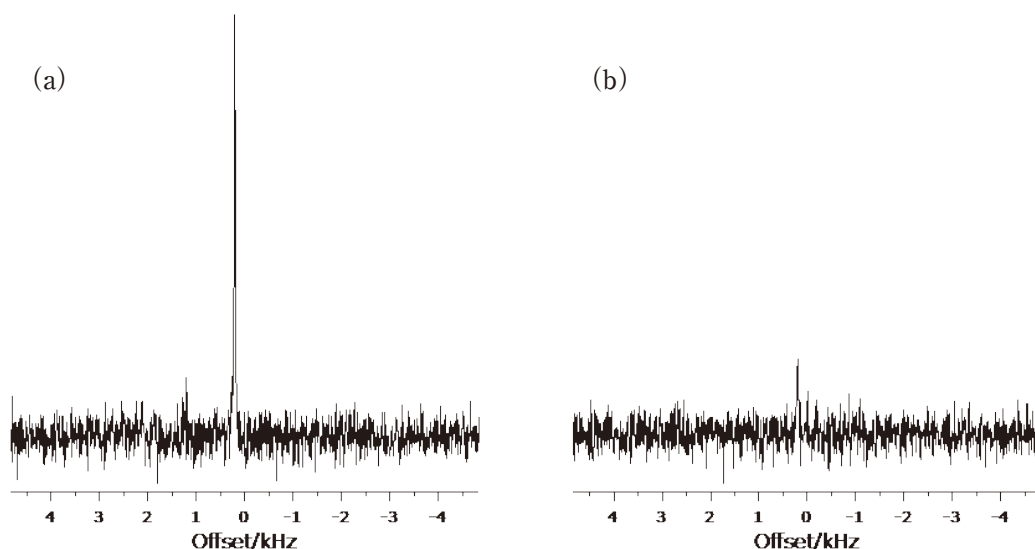
Moreover, for the sixth-prototype Cryo-Coil MAS Probe, which was manufactured so as to observe low-gamma nuclei whose carrier frequency is 70 MHz or a few lower, we implemented a modification. That is, in order to enable tuning even for further low-gamma nuclei whose carrier frequency is down to 30 MHz, we manufactured a new detection coil for which the number of turns of a solenoid coil was increased from 4 to 12, and then we applied this new coil to the sixth-prototype probe.

To confirm the effectiveness of this modification, **Fig. 6** shows two ^{43}Ca MAS-NMR spectra acquired with the sixth-prototype Cryo-Coil MAS Probe, where the detection system (comprised of a detection coil, a preamplifier and a duplexer) was placed at low temperature (a) and at room temperature (b). The experimental conditions for the two cases were as

follows. Carrier frequency: 40.38 MHz, Sample: Calcium oxide (CaO), Sample volume: 42.38 mg, Number of accumulations: 64, Repetition time: 100 s, Sample spinning speed: 13.0 kHz. When comparing the both spectra, the sensitivity improvement ratio at low temperature reached 4.35 times. This result is rather inferior to that presented in Fig. 4 and Fig. 5 for the case of the comparison between the fifth-prototype probe and a conventional probe. The reason for this result is considered to be an increased resistance value per unit inductance for the solenoid coil, which may degrade the sensitivity. That is, compared to the conventional solenoid coil with 4 turns, a new solenoid coil with 12 turns decreases the line width of the coil in a limited coil space for increasing the inductance. Trade-off between the sensitivity and tuning range and creation of a low-loss coil will solve this problem.

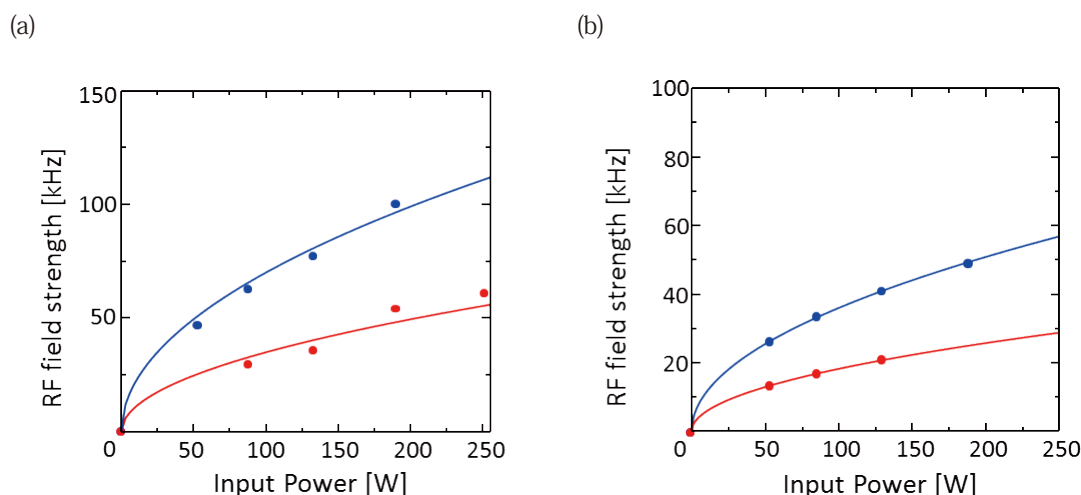
Finally, the efficiency of the RF irradiation field for the Cryo-Coil MAS Probe is discussed. **Figure 7** shows the RF field-strength dependence on the input power, where ^6Li and ^{43}Ca were measured in 14T magnetic field. In the present prototype-probe, under an ultra-low temperature environment, the probe Q value is increased to approximately 4 times from that at room temperature. Thus, the irradiated RF field strength is proportionally increased to approximately 2 times larger than the square of the RF field strength. Although there exists the carrier frequency dependence, it is possible to output the RF field strength of 60 kHz to 100 kHz against an input power of 250 W. This result demonstrates that the Cryo-Coil MAS probe is suitable to excite a wide spectrum characteristic of Solid-state NMR measurement. In principle, in order to maximize the RF field strength at the center of the detection coil, the proto-type probe adopts the balanced circuit method to sandwich capacitors of the same capacity between the both ends and the grounded surface of the detection coil. However, in the both fifth and sixth prototypes used for the present experiments, the capacity

Fig. 6



(a) ^{43}Ca MAS-NMR spectrum of natural abundance calcium oxide, acquired with the sixth-prototype Cryo-Coil MAS Probe, where the temperature of the detection coil is at low temperature (< 17K).
 (b) For comparison, ^{43}Ca MAS-NMR spectrum of the same sample in (a) under the same experimental conditions was acquired with the sixth-prototype Cryo-Coil MAS Probe, where the temperature of the detection coil is at room temperature (= 296K).
 Pulse sequence for the both spectra is Single $\pi/6$ pulse (dead time: 500 μs). Input power for the both spectra is 121 W. $\pi/2$ pulse width is 12.6 μs for the spectrum in (a) and 6.3 μs for the spectrum in (b).

Fig. 7



Plots of the RF field strength of two prototype Cryo-Coil MAS Probes against the input power.

(a) RF field-strength dependence on the input power for ${}^6\text{Li}$ (with the fifth prototype. Carrier frequency: 88.3 MHz).

(b) RF field-strength dependence on the input power for ${}^{43}\text{Ca}$ (with the sixth prototype. Carrier frequency: 40.38 MHz).

The two plots are obtained by least-squares fit with a quadratic curve. Red filled circles indicate the experimental plotted values with the temperature of the detection coil being 296K. Blue filled circles indicate the experimental plotted values with the temperature of the detection coil being 17K.

of each end of the detection coil is not equal and therefore, the maximization of the efficiency of the RF irradiation field is not achieved. Thus, we are now manufacturing a new seventh prototype probe that is equipped with a tunable system that enables to balance the capacity of capacitors between the both ends of the detection coil [10]. Using this new prototype, we will intend to maximize the efficiency of the RF irradiation field for multiple nuclei whose resonated frequency ranges from low to medium frequencies (25 MHz to 200 MHz).

Conclusion

A Cryo-Coil MAS Probe for multinuclear measurement, which enhanced the Solid-state NMR sensitivity of 4.45 times that of a normal NMR probe, was developed. We presented the principle, outline and performance of the Cryo-Coil MAS probe by our experiments using the prototype probes. In particular, this NMR probe facilitates measurement of nuclei of inorganic materials, which was difficult due to very low measurement sensitivity for those materials.

Owing to this powerful feature, the Cryo-Coil MAS Probe is expected to extend its application fields for Solid-state NMR. In the future, we will also strive to continue the research and development of a double-resonance probe capable of 1H irradiation so as to broaden the application fields to nuclei of organic materials.

Acknowledgments

This joint research work was supported as several programs (Core Research for Evolutional Science and Technology (CREST: 2005-2010) and Development of Systems and Technology for Advanced Measurement and Analysis (SENTAN: 2010-2012, 2013-2015)) by Japan Science and

Technology Agency. The author would like to acknowledge Professor Kiyonori Takegoshi of Kyoto University and Station Director Tadashi Shimizu at High Magnetic Field Station of National Institute for Materials Science for their warm guidance and support.

References

- [1] E. R. Andrew et al., *Nature* **182**, 1659 (1958); *Nature* **183**, 1802 (1959).
- [2] D. I. Hoult et al., *J. Magn. Reson.* **24**, 71 (1976).
- [3] P. Styles et al., *J. Magn. Reson.* **60**, 397 (1984); *J. Magn. Reson.* **84**, 376 (1989).
- [4] R. F. Bradley, *Nucl. Phys.* **B 72**, 137 (1999).
- [5] D. Marek, US 5247256 A (1993); V. Kotsubo et al., US 5508613 A (1996).
- [6] M. W. Voehler et al., *J. Magn. Reson.* **183**, 102 (2006).
- [7] T. Mizuno et al., *Rev. Sci. Instrum.* **79**, 044706 (2008); K. Takegoshi et al., JP4933323 B4 (2012), US8013608 A1 (2007).
- [8] T. Mizuno et al., *Rev. Sci. Instrum.* **80**, 124702 (2009); K. Takegoshi et al., JP5464445 B4 (2014), US2011-0187371 A1 (2011), EP2357485 B1 (2014).
- [9] S. Levasseur et al., *Chem. Mater.* **15**, 348 (2003).
- [10] T. Mizuno et al., JP2015-022651 B2 (2015).

Development of JEM-F200(F2) Multi-Purpose Electron Microscope

Kazuya Yamazaki
EM Business Unit, JEOL Ltd.

High-resolution analytical systems, such as transmission electron microscopes (TEM) and scanning transmission electron microscopes (STEM) are still attracting the attention of many researchers. Higher resolution and higher efficiency are required for modern microscope systems, along with further improved ease of use. To meet those needs, a multi-purpose electron microscope, the JEM-F200 (nickname: F2), has been developed as a next-generation electron microscope. The special features of this revolutionized microscope system, F2, are described in this article.

Features

In the JEM-F200 (nickname: F2), TEM lattice image resolution of 0.1 nm and STEM image resolution of 0.14 nm are achieved (with cold field-emission gun (Cold FEG) and ultra-high resolution configuration). This powerful, next-generation microscope system also has a wide variety of features presented below.

Smart Design

As a next-generation electron microscope, the appearance of F2 has been rebuilt under the design concept “Smart” (Fig. 1). In addition, development of a sophisticated system which enables one to instantaneously know the instrument conditions has become a high priority. Thus, a new user interface focusing on intuitive operation has been developed for analytical electron microscopy (Fig. 2). F2 is equipped with the TEM Center (for microscope operation) and the Analysis Center (for image analysis). Data acquisition is supported utilizing these software systems. In the TEM Center, an intuitively-understandable animation enables very smooth operations of the electron beam, apertures, the specimen stage, detectors, etc. F2 also incorporates automatic systems including the automatic coma-free alignment software. The Analysis Center enables the operator to analyze the image data obtained with the TEM center, through an image analysis function for length measurement and/or fast Fourier transformation (FFT) and a database function. Another unique feature of F2 is that the operator can carry out traditional visual image-observation through the fluorescent screen in the viewing chamber and also can view a digital image obtained with a remote camera system. Furthermore, the knowhow on mechanical and electrical stability of microscope, which has been accumulated for many years in JEOL, is effectively reflected to the design of F2. This design results in greatly improved stability of the microscope compared to conventional JEOL TEMs. Therefore, performance

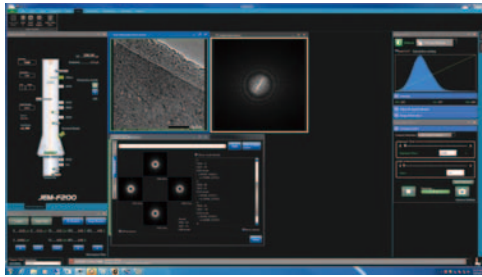
Fig. 1 Entire appearance of JEM-F200 (F2).



A “Smart” exterior design that is suitable for a next-generation microscope is made by adopting pure white for the base color and metallic silver for the accent color. In addition, the placement of apertures and detectors is optimized to make no protrusion of the microscope units.

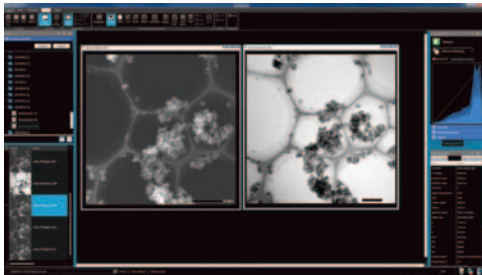
that surpasses the predecessor model JEM-2100F is achieved for F2 (Fig. 3). JEOL’s proven optical system is also succeeded to F2, thus making this microscope system applicable to Lorentz electron microscopy which is an important method for analysis of magnetic materials (Fig. 4).

Fig. 2 JEM-F200 control software.



TEM Center

Software system to control the microscope operations. The system consists of a control section with an easy-to-understand animation, and an image display section.



Analysis Center

Software system to analyze the obtained image data, including length measurement, FFT and image processing.



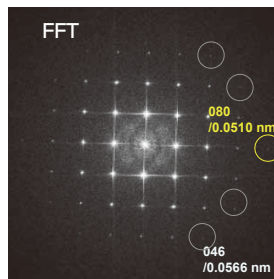
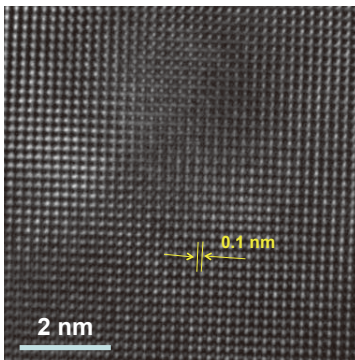
F2 operation section

With a focus on "intuitive operation", a control panel with minimum necessary switches and knobs are provided.

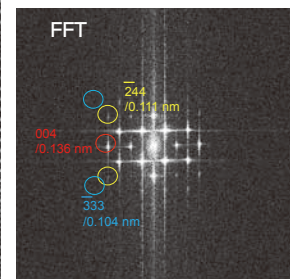
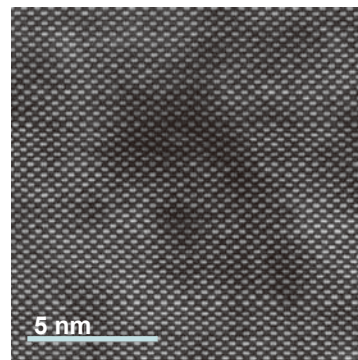
In the TEM Center, a new user interface incorporating an intuitively-understandable animation, which shows the operations of the microscope column and peripheral units, allows the operator to smoothly know the instrument conditions. The Analysis Center is an image-analysis software system to meet the requirements of users and this system enables the operator to analyze the image data obtained with the TEM center, through an image analysis function for length measurement and/or fast Fourier transformation and a database function.

Fig. 3 TEM resolution and STEM resolution.

TEM Basic Performance

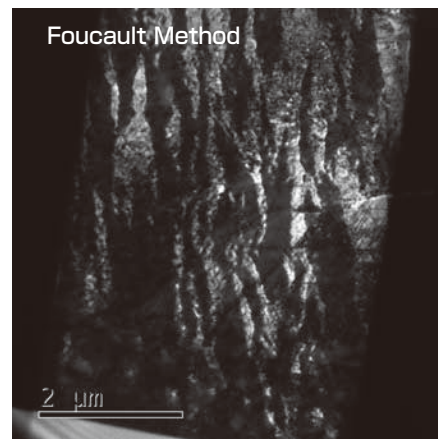
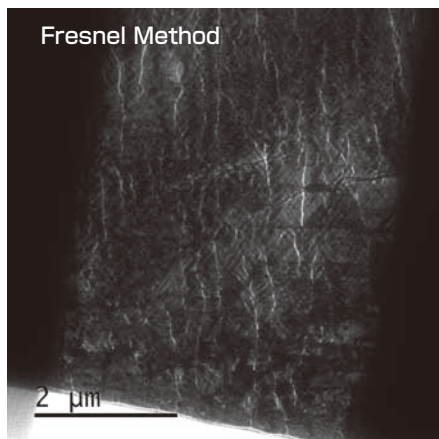


STEM-HAADF Basic Performance



In an FFT pattern of a TEM lattice image obtained from Au (gold) thin foil in the [100] orientation, spots of 0.05 nm (50 pm) are confirmed (second from left). In an FFT pattern of a STEM-HAADF image obtained from a Si (silicon) single crystal in the [110] orientation, spots of 0.1 nm are confirmed (right edge). This result demonstrates high mechanical and electrical stability of F2.

Fig. 4 Example of Lorentz electron microscopy.



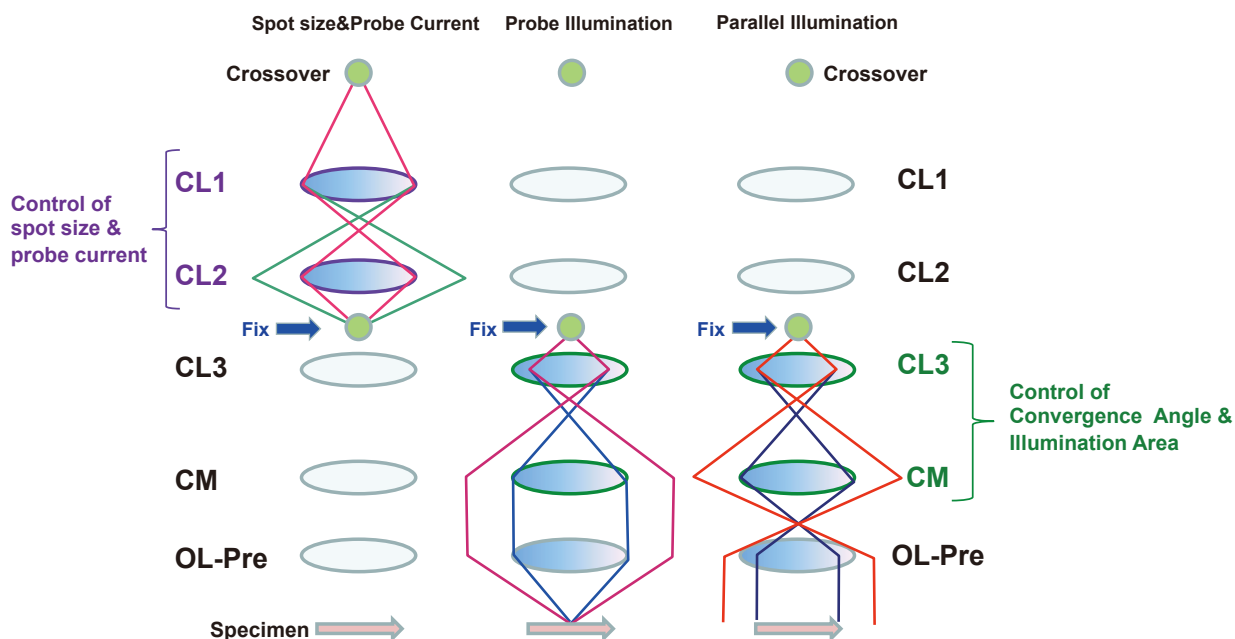
Lorentz electron microscope images (Fresnel method and Foucault method) of Sm_2Co_7 magnet thinned with a JEOL JIB-4000 Focused Ion Beam System. It is confirmed that nano-scale magnetic domain walls and magnetic domains are clearly imaged with sufficient contrast.

Quad-Lens Condenser System

Modern electron microscopes must satisfy a wide range of imaging techniques from traditional bright-field (BF) & dark-field (DF) TEM and STEM that use a variety of detectors. To meet such sophisticated needs, F2 incorporates the “Quad-Lens condenser system” which consists of 4-stage illumination (probe-forming) optical system so as to support a variety of

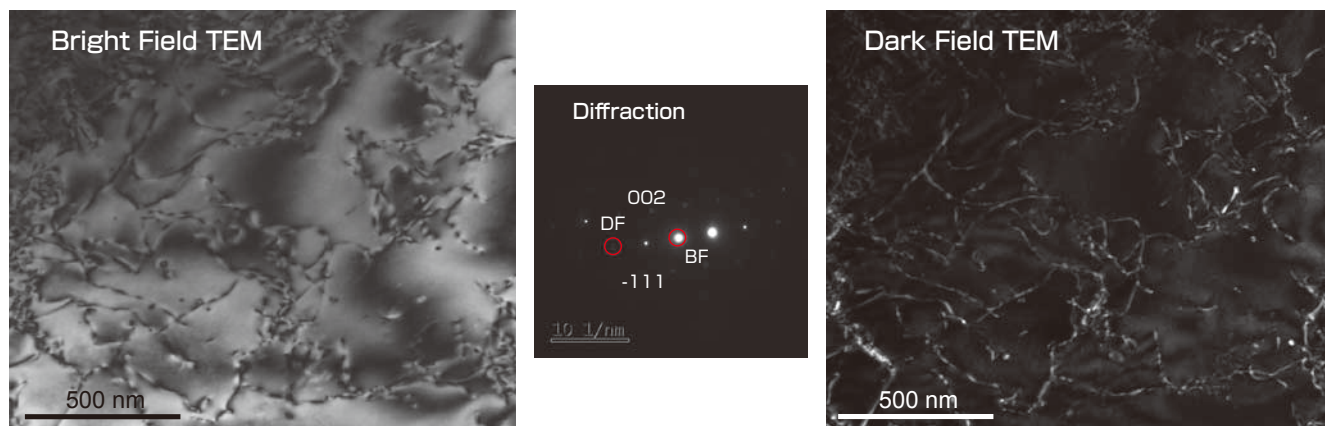
applications. With this new optical system, a crossover formed by the electron source is fixed to a designated position, thus enabling independent control of the electron beam intensity and the convergence angle. In addition, parallel beam illumination which is essential for TEM imaging is realized in the same manner as conventional TEMs (Fig. 5). The use of the Quad-Lens condenser system enables formation of high-quality BF-TEM & DF-TEM images (Fig. 6).

Fig. 5 Quad-Lens condenser system.



F2 incorporates four-stage condenser lenses. Control of the spot size and probe current is made with CL1 and CL2 (upper part), whereas the control of the convergence angle and illumination area is implemented with CL3 and CM (lower part). The crossover formed by CL1 and CL2 is controlled to always fix this crossover to a designated position. All of the spot size, probe current, convergence angle and illumination area are independently controlled, thus achieving a sophisticated control of the convergence angle so that this angle is unchanged even when the spot size is changed.

Fig. 6 Example of bright-field & dark-field TEM images.



Bright-field & dark-field TEM images are traditionally used for materials analysis. In this example, dislocations in over-aged Al alloy are imaged by an incident electron beam from the [110] direction. Both images reveal the dislocations in a wide field-of-view.

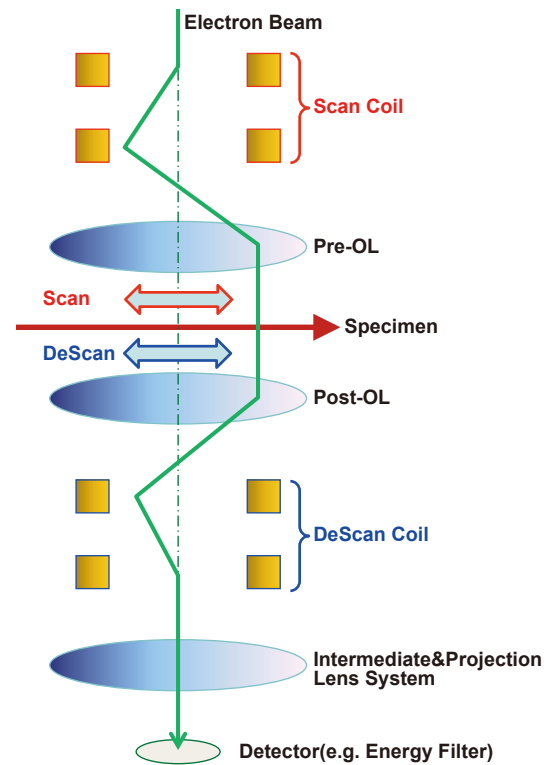
Advanced Scan System

The scan system in an electron microscope is of prime importance for ultrahigh-resolution analytical techniques. F2 enables simultaneous image acquisition of STEM-DF/STEM-BF/BEI and/or SEI, and also incorporates a function to obtain STEM-ABF images that has been attracting attention as a light-element imaging method with ultrahigh resolution. In addition to these functions, F2 is equipped with the “Advanced Scan System” to enable installation of the DeScan system into the microscope column, by which the movement of a scanned electron beam on the detector plane is compensated by the scan coil below the specimen (Fig. 7). This powerful system plays an outstanding role in STEM-EELS where electron energy-loss spectroscopy (EELS) and STEM are combined. With this system, a wide-field STEM-EELS spectrum (and mapping image) over the micrometer order can be obtained, which could not be acquired before (Fig. 8).

Pico Stage Drive

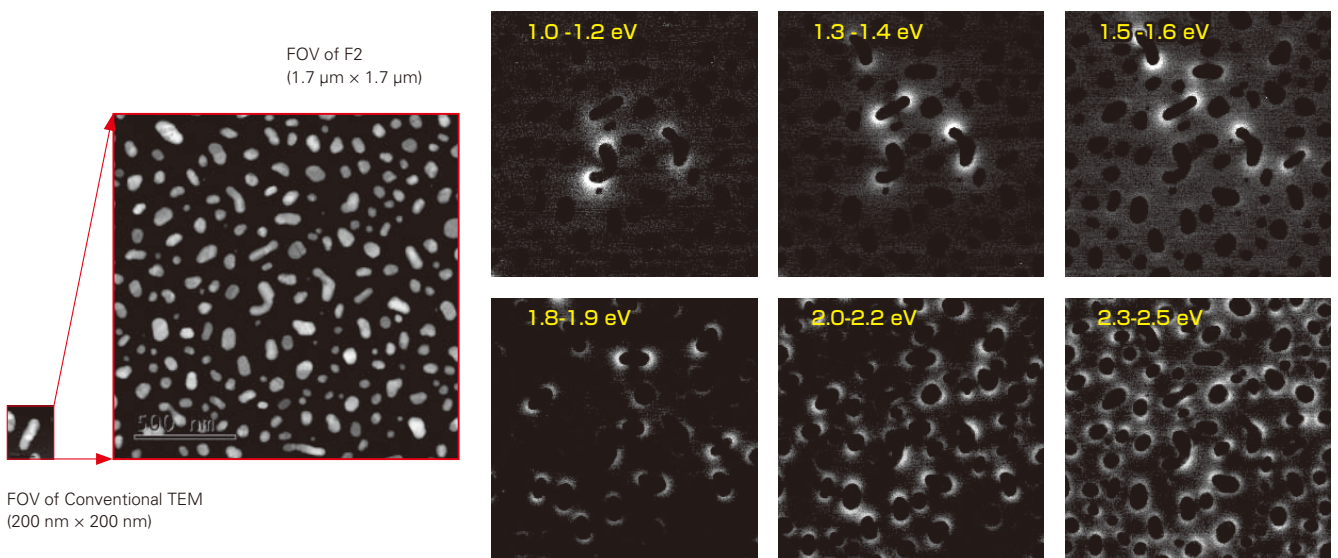
The specimen stage for a TEM requires fast and highly-precise drive performance. F2 comes with an ultra-fast, high-precision “Pico Stage Drive”, as well as a super-high-precision piezo drive mechanism. This Pico Stage Drive simultaneously achieves both ultra-fast drive that enables the stage to move in approximately 7 seconds over a wide area of the diameter of 2 mm (highest speed: 0.3 mm/s) and ultrahigh-precision drive that allows a specimen (on the stage) to move in steps of subnanometers (0.2 nm/step). Incorporation of the Pico Stage Drive into F2 enables the operator to perform screening of the entire area of the specimen, and also to perform superbly-fine drive in ultrahigh-resolution imaging. Thus, F2 is expected to achieve greatly improved throughput for observation at low to ultrahigh magnifications.

Fig. 7 Schematic of DeScan.



Scanning the DeScan coil in the image forming system in conjunction with the scan coil above the specimen makes it possible to compensate the movement of the scanned electron beam so that the electron beam always coincides with the optical axis of the image forming system. This capability suppresses the movement of the electron beam to the minimum on a given detector plane.

Fig. 8 Example of STEM-EELS mapping images in a wide field.



The left mapping image shows surface plasmon resonance of Ag (silver) nanoparticles dispersed on a carbon film. With the conventional microscope, the FOV (field-of-view) was confined to 200 nm squares. An effective use of the DeScan in F2 broadly expands the FOV to up to 1.7 μm squares for obtaining STEM-EELS spectrum and mapping images (shown in a series of right-side images). In this example, the energy range displayed is varied. Each six image clearly demonstrates imaging of the resonance from a STEM-EELS spectrum. (Accelerating voltage: 200 kV, taken with GATAN Quantum ER. Specimen courtesy: Dr. T. Sannomiya at Tokyo Institute of Technology)

SPECPORTER

Insertion or extraction of a specimen holder has been considered to be a difficult part of operations, especially for novice users. To eliminate this problem, we have developed the SPECPORTER that facilitates loading and unloading of the specimen holder (trademark registration of “SPECPORTER” is being applied). When the operator sets a specimen holder at a designated position and activates the SPECPORTER by simply clicking a switch, the holder is automatically inserted or extracted in safety. While taking over a highly-regarded JEOL double O-ring holder (for the first use with JEM-2010), the operator can smoothly insert or extract the specimen holder (Fig. 9). This system also allows manual loading and unloading of the holder, thus enabling the operator to use conventional manual-operation holders for the previous microscopes. Furthermore, a conventionally-used specimen holder can be modified so that the holder is inserted or extracted using the SPECPORTER (not applicable to some holders).

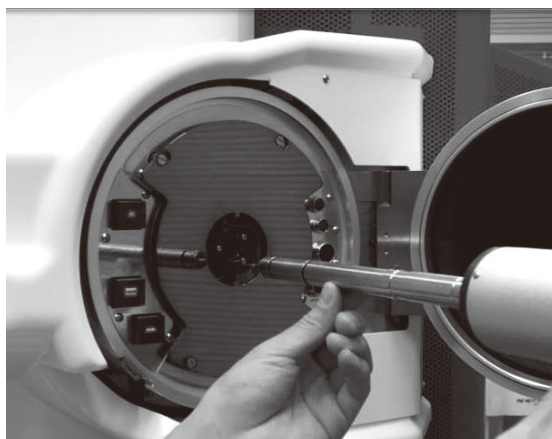
High-Brightness Electron Gun

In addition to a long-time proven Schottky electron gun, F2 supports an optional cold field-emission gun, “Improved Cold FEG”. With its high-brightness, high energy-resolution electron source, this Cold FEG enables high energy-resolution analysis and high-resolution imaging (Fig. 10). Standard accelerating voltages for F2 are set to 200 kV and 80 kV. This voltage setting enables observation and analysis of carbon nanotube, which requires low accelerating voltages (Fig. 11). Furthermore, various accelerating voltages are optionally available (120 kV, 100 kV, 60 kV, 40 kV, 20 kV), allowing the operator to select a desired voltage depending on research purposes.

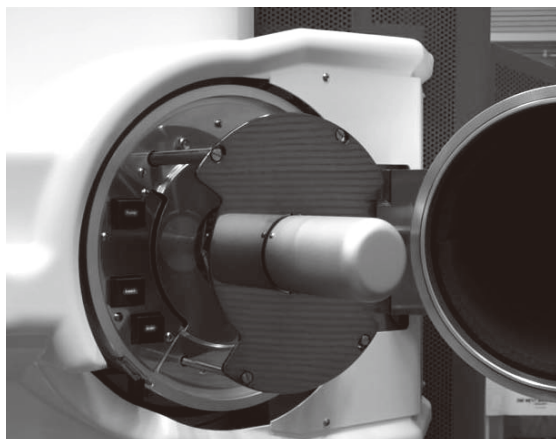
Dual SDD

Two large solid-angle silicon drift detectors (SDDs) with high analytical sensitivity can be simultaneously installed into the microscope column. This configuration of the Dual SDD system enables analysis of characteristic X-rays emitted from a sample with higher sensitivity and throughput. Among this system, SDD1 is placed at 90 degrees with respect to the

Fig. 9 Operations of SPECPORTER.



(1) Set Specimen Holder and Click Switch



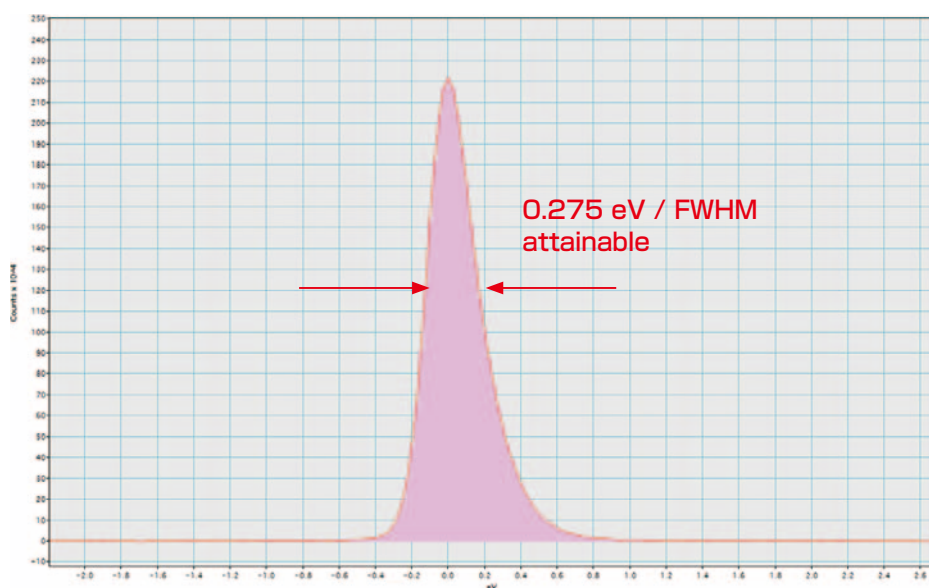
(2) Open the isolation valve and Loading-Plate transfer holder



(3) Holder insert to Goniometer automatically

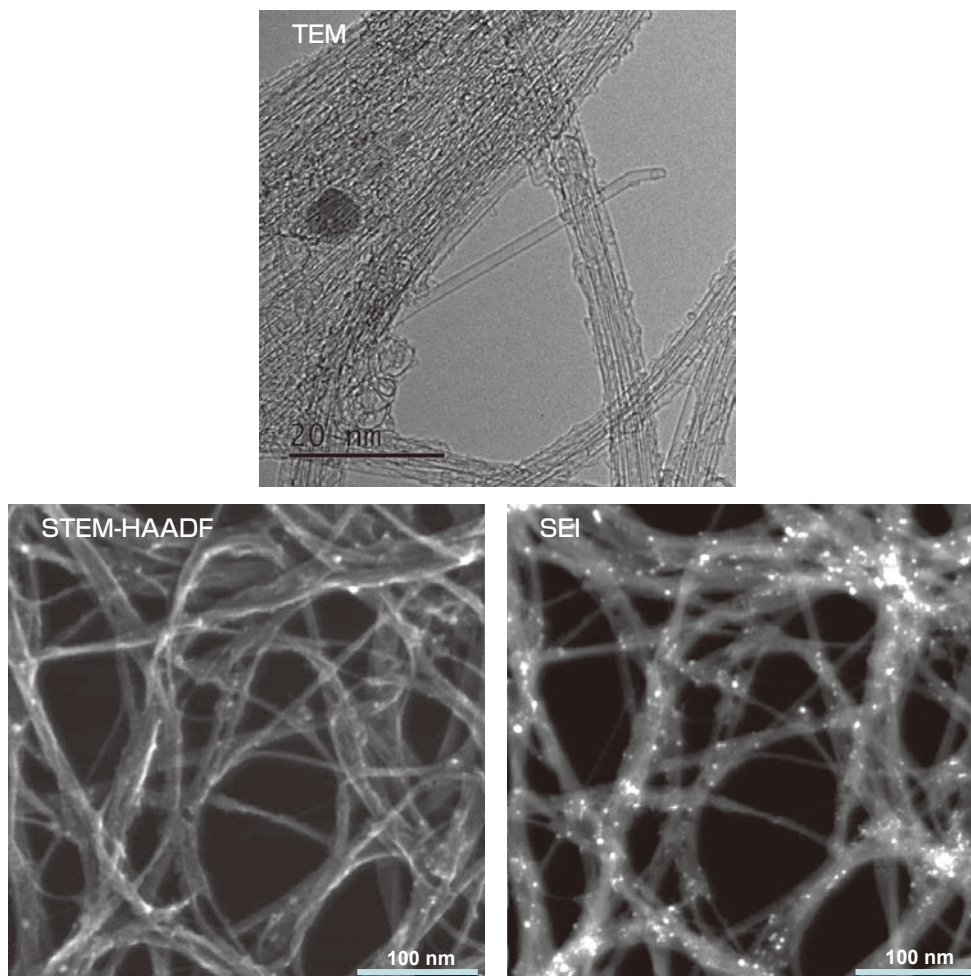
(1) Set a specimen holder at a designated position and click a switch to (2) open the isolation valve with the loading-plate catching the specimen holder and rotating the goniometer for (3) automatically inserting the specimen holder into the microscope column.

Fig. 10 High energy resolution obtained from the Improved Cold FEG.



Zero-loss spectrum obtained with the F2 microscope that incorporates the Improved Cold FEG. FWHM (full width at half maximum) of as narrow as 0.275 eV is achieved.

Fig. 11 Three kinds of images of single-wall carbon nanotube containing catalyst particles, obtained at a low accelerating voltage.



Even at an accelerating voltage of as low as 80 kV, high-quality TEM & STEM-HAADF images and SEI (secondary-electron image) of single-wall carbon nanotube can be observed. The TEM image provides high-resolution information, the STEM-HAADF image shows the Z (atomic-number) contrast, and the SEI reveals the surface information.

specimen holder rod axis, whereas SDD2 is placed along the holder axis. Moreover, the geometry of SDDs and the specimen holder is optimized to allow larger solid angle for each polepiece configuration (Fig. 12). This unique placement and geometry design enable F2 to be applicable to the change of detection efficiency according to the specimen tilt. With a combination of the Dual SDD system and the high-brightness electron gun, F2 is effectively utilized for both 3D-EDS tomography that is attracting interest as a powerful 3D analysis technique (Fig. 13) and high-speed EDS analysis of a specimen susceptible to electron-beam irradiation (Fig. 14).

Environmental Friendly

Reducing the management cost of the microscope must be progressed today. F2 is the first TEM to come with an ECO mode. The ECO mode system saves energy when the instrument is not used by keeping the microscope under good standby conditions. This mode suppresses energy consumption to approximately 1/5 of that compared to when the microscope is used. A scheduling function is also included in the ECO mode that allows the microscope to be recovered from ECO mode to ready-to-use states (for observation) at a designated time. For example, when the microscope is set to the ECO mode at night or holidays, the annual consumption power can be reduced by approximately 60%. (Note that the total consumption power over one year is obtained by assuming that the microscope is operated under the following conditions: The total operation

days are defined to be 240 days, whereas holidays to be 120 days. It is assumed that, in one operation day, 8 hours are used for operation and the rest 16 hours are operated in the ECO mode. In holidays, the ECO mode is applied to the microscope.)

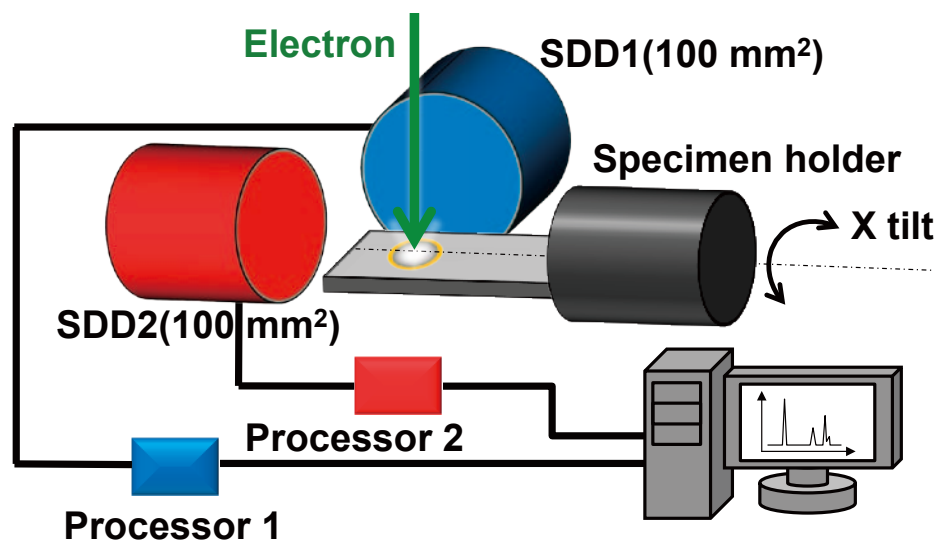
Summary

To meet today's needs for high-resolution analytical systems, we have developed a next-generation electron microscope JEM-F200 (F2) that achieves higher resolution and higher efficiency, along with further improved ease of use. This revolutionized microscope system incorporates a variety of new functions and therefore, the JEM-F200 will be expected to greatly contribute to a wide range of research needs, including materials analysis, macro-molecular analysis and cryo-electron microscopy. We intend to further strengthen the functions incorporated in F2 by feeding back requests from users in the future.

Acknowledgements

The author would like to acknowledge the support and assistance of Akira Yasuhara, Tomohisa Fukuda, Shuichi Yuasa, Mitsuhiro Terao, Natsuko Nakamura, Masashi Nishikawa, Yuji Yamazaki, Hisao Kihara, Keita Anjiki, Naoko Nagatake, Hidenori Nagatake, Taishi Sakai, Akihiro Saitow, Isamu Ishikawa, Toshikatsu Kaneyama, Yoshihiro Okura and the JEM-F200 project members at JEOL Ltd.

Fig. 12 Schematic view of Dual SDD system (above) and Table on solid angles for each polepiece configuration (below).

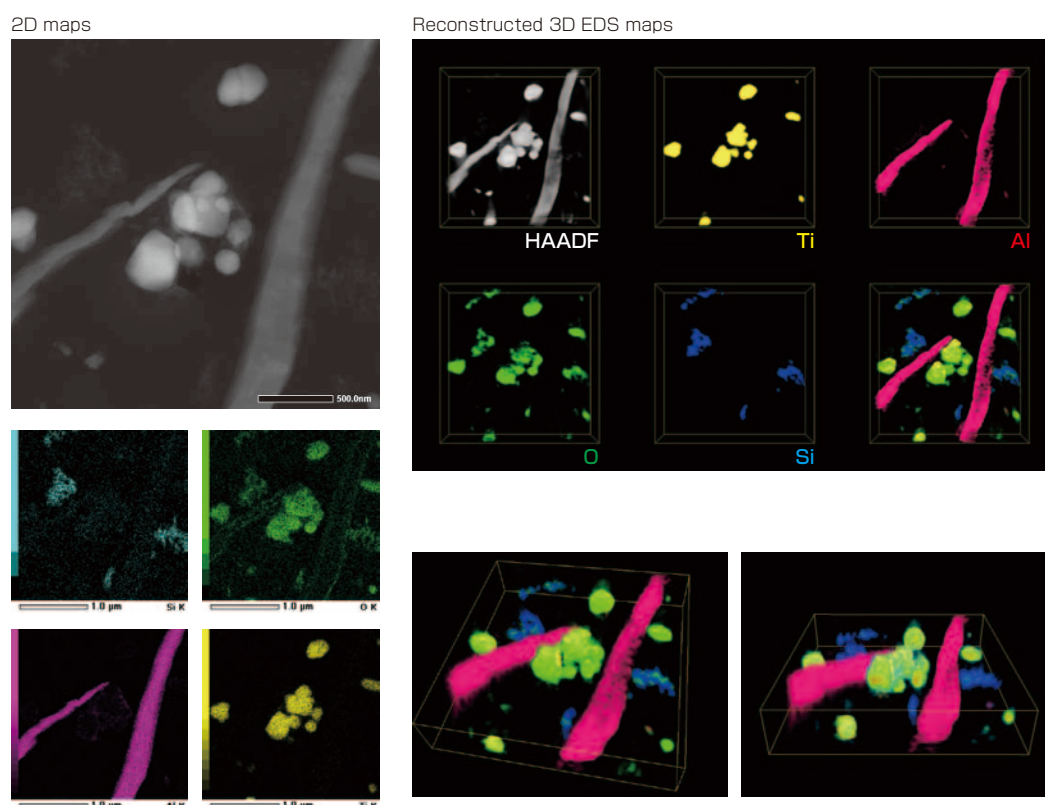


| | UHR | HR | CR |
|-------------------|--------------------------------|--------|-----------|
| Solid Angle | 1.2 sr | 1.7 sr | 0.44 sr * |
| Energy Resolution | ≤ 133 eV (Mn-K α) | | |

*:Only SDD1

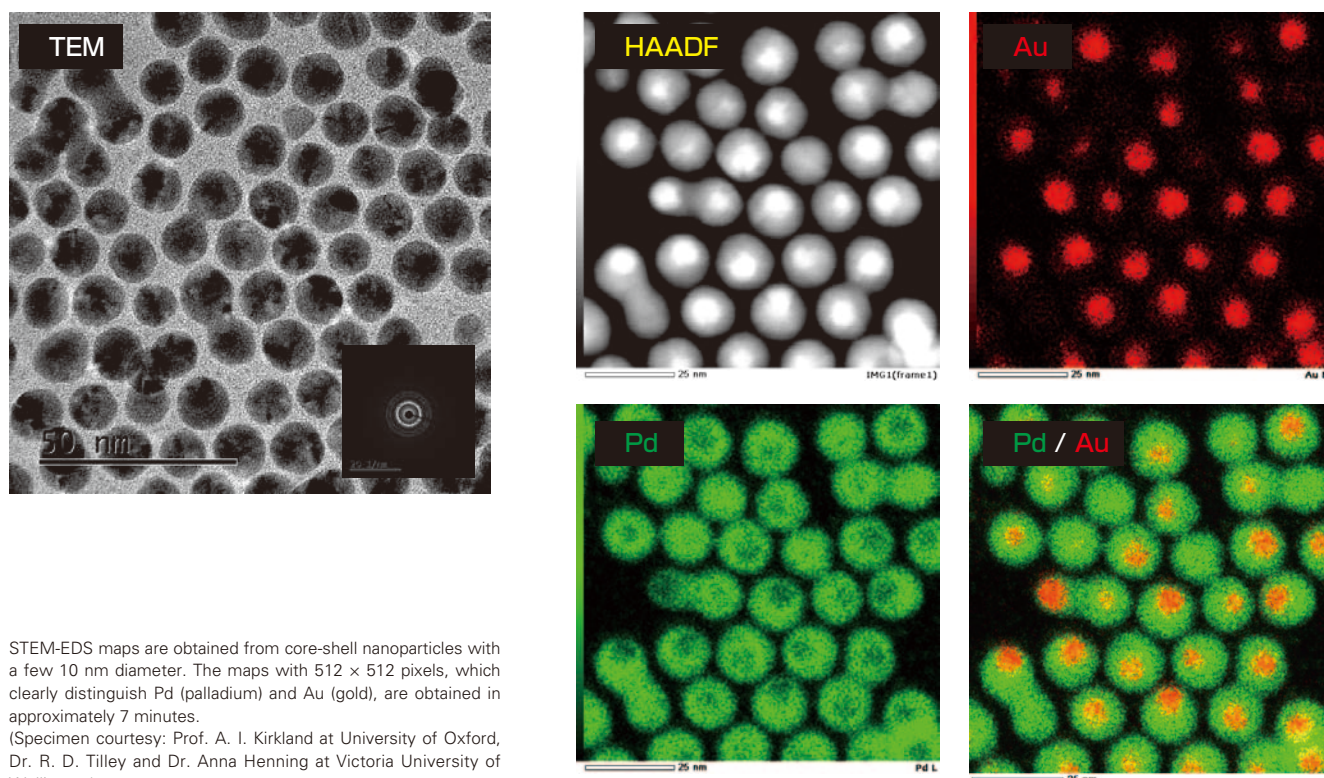
SDD1 is placed at 90 degrees with respect to the specimen holder rod axis, whereas SDD2 is placed along the holder axis. The geometry of SDDs and the specimen holder is optimized to allow larger solid angle for each polepiece configuration, as listed on the table below.

Fig. 13 Example of data acquisition by 3D-EDS tomography.



Reconstructed 3D-EDS maps of a coating film obtained by tomography are shown. 3D locations of Ti/Al/O/Si are clearly imaged at the nanometer scale. (Acquisition conditions: Accelerating voltage: 200 kV, EDS: JEOL-made 100 mm² SDD, Tilt range: ±60° (in 5° steps), Image acquisition time: 30 seconds per image, 3D reconstruction with 2715 nm × 2715 nm × 559 nm.)

Fig. 14 Example of high-speed STEM-EDS maps.



STEM-EDS maps are obtained from core-shell nanoparticles with a few 10 nm diameter. The maps with 512 × 512 pixels, which clearly distinguish Pd (palladium) and Au (gold), are obtained in approximately 7 minutes. (Specimen courtesy: Prof. A. I. Kirkland at University of Oxford, Dr. R. D. Tilley and Dr. Anna Henning at Victoria University of Wellington)

Three-Dimensional Reconstruction of Biological Tissues by Serial Block Face-SEM

Yuuki Yamaguchi¹, Tomohiro Haruta², Akira Mizoguchi³, Hideo Nishioka²

¹ SM Business Unit, JEOL Ltd.

² Application Management Department, JEOL Ltd.

³ Mie University Graduate School of Medicine.

Scanning Electron Microscopy (SEM) is used to observe biological tissues over a wide region with high resolution. Serial Block Face-SEM (SBF-SEM) is one of innovative techniques, which repeats cutting a block specimen embedded in resin with an ultra-microtome incorporated in a SEM specimen chamber and observing the specimen surface. By SBF-SEM, it is easy to observe three-dimensional structures of biological tissues composed of cells. In this method, specimen preparation and data analysis are also important as well as observation techniques. In this article, we review not only SBF-SEM and actual observation techniques, but also specimen preparation and data analysis. We also report the observation and analysis of the CA3-region in mouse hippocampus by SBF-SEM.

Introduction

To understand biological phenomena, it is necessary to understand biological materials down to: (1) molecular level, (2) organelle level, (3) cell level, (4) tissue level, and (5) one entire body level. For example, growth directions of plant cells depend on orientations of microtubules, whereas in vertebrates, ciliary motions in node regions determine right-left of their bodies. Conventionally, Optical Microscopy or X-ray CT has been mainly used to understand mesoscopic structures of biological tissues composed of cells. However, resolution of these methods is too poor to observe details of organelles. Thus resolution of Electron Microscopy has been required. Moreover, a wide field of view comparable to that of Optical Microscopy and three-dimensional observation of fine structures has been required. TEM Tomography is well known as a three-dimensional reconstruction method using the Transmission Electron Microscopy (TEM). This effective method provides high resolution that is possible to observe molecules, but its field of view is narrow ranging from sub-nanometers to sub-micrometers.

Recently, SEM has provided high resolution images at low accelerating voltages with high signal-to-noise ratio. Therefore, if biological tissues are stained with heavy metals and embedded in resin, backscattered electron images of the tissues are observed. An observation area of SEM is wider than that of TEM. Resolution of SEM is much higher than that of Optical Microscopy or X-ray CT. The three-dimensional reconstruction by SEM is called “Serial Section SEM (SSSEM)” combined with specimen slicing and surface observation. There are three

methods using SSSEM. The first is SBF-SEM. In this method, cutting and observing a block specimen are repeated in a SEM chamber. The specimen is cut by ultra-microtome incorporated in the SEM chamber. The second is Focused Ion Beam-SEM (FIB-SEM). In this method, cutting and observing a block specimen are repeated in a SEM chamber, too. But the specimen is cut by Gallium-ion beam incorporated in a SEM chamber. The third is Array Tomography. In this method, serial ultra-thin sections of a specimen are prepared with an ultra-microtome, and are observed with SEM. Among them, each method has advantages and disadvantages. In this article, we described three-dimensional observation of biological specimens by SBF-SEM.

Instruments and Methods

SBF-SEM

SBF-SEM is one of techniques which repeats cutting and observing a block specimen in a SEM chamber (Denk, Horstmann, 2004 [1]). Gatan Inc. has developed 3View®2XP utilizing this technique.

3View®2XP is a specimen stage equipped with an ultra-microtome and repeats cutting a block specimen in a SEM chamber (**Fig. 1**). The repeat of cutting and observing makes it possible to acquire serial two-dimensional images, and stacking of these images makes a three-dimensional image (**Fig. 2**). This procedure is called three-dimensional reconstruction.

The major feature of this innovative instrument is to reconstruct a three-dimensional image over a wide region with high resolution. A cutting region of a specimen by ultra-

microtome covers an area of $1.2 \times 1.2 \text{ mm}^2$ or less and depth of 0.6 mm or less. Cutting thickness, which corresponds to Z-resolution, is set to 15 to 200 nm. Cutting time at one cycle is as fast as about 15 seconds. Furthermore, since the specimen stage is vertically raised by cutting amount of a specimen, there is no focus shift and little XY-position shift. The series of those operations are performed automatically.

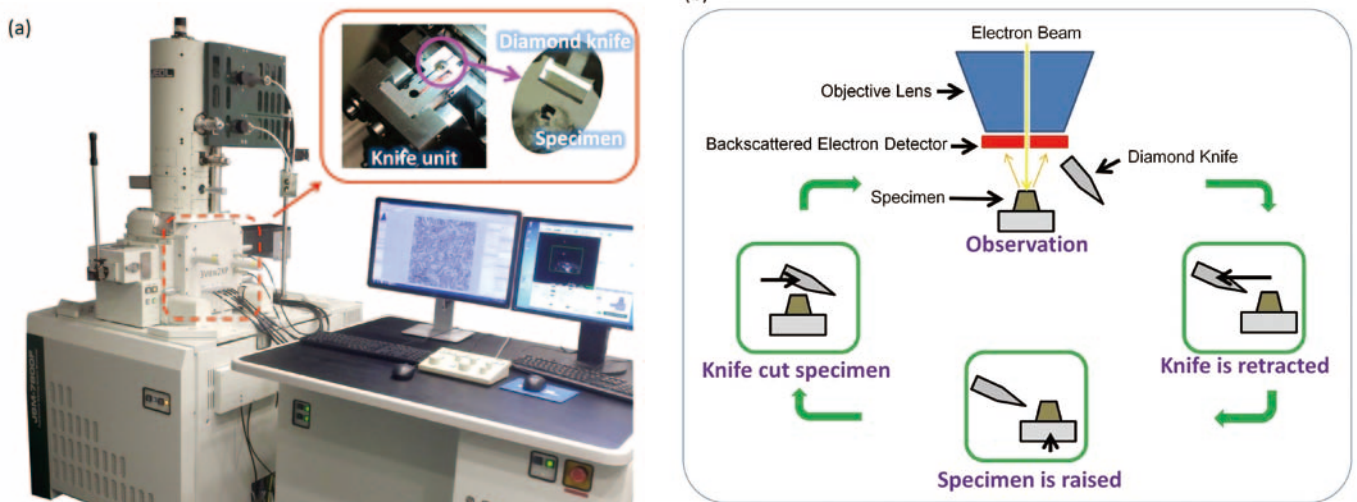
In FIB-SEM, it is possible to cut a specimen by a few nanometers, but its cutting area is narrower and its cutting speed is slower than that of SBF-SEM. In Array Tomography, a specimen is observed as serial ultra-thin sections put on conductive substrates (silicon wafer, etc.). Thus, XY-resolution is high, since signals from the deep region of a specimen at high accelerating voltages are not detected. But since it is manual to

put the ultra-sections on the substrates and to observe them with SEM, skills and time are required for this operation. In addition, since the ultra-thin sections are easily transformed and rotated, it is not easy to align images of the sections before stacking. The advantage of this method is to be able to observe repeatedly because the sections are preserved.

SEM observation

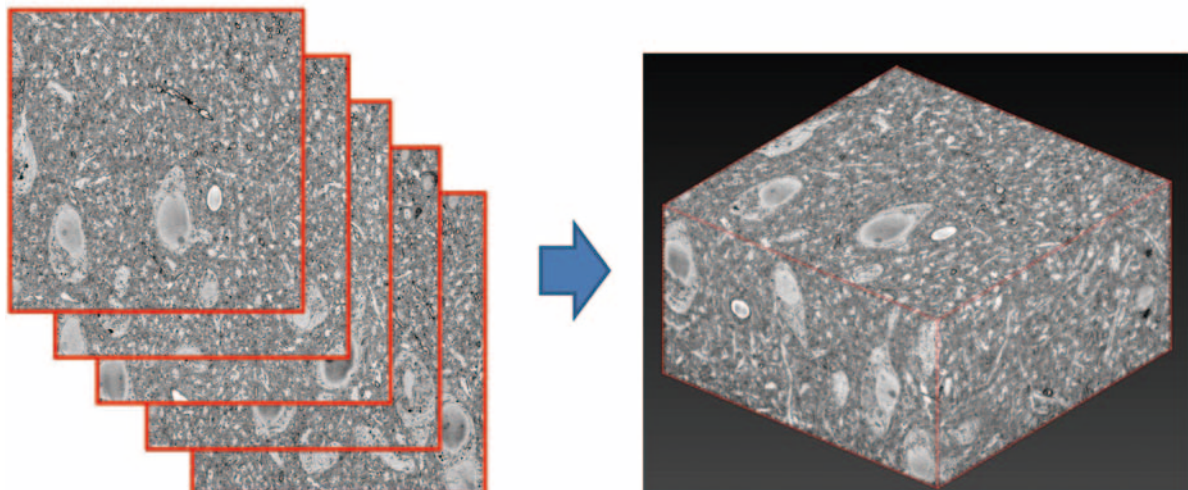
Field Emission SEM (FE-SEM), which enables to observe a specimen for a wide range of magnifications from low to high, is suitable to SBF-SEM (JSM-7800F, JEOL Ltd., Fig. 1(a)). In 2015, Fleck et al. reported the observation of biological tissues by using JSM-7100F (JEOL Ltd.) equipped with 3View[®]2XP [2]. For SBF-SEM, FE-SEM having the three features is needed,

Fig. 1 JSM-7800F with 3View[®]2XP.



(a) Over view of the system. An ultra-microtome is installed in the SEM chamber.
 (b) Workflow showing the repeat of cutting and observing a block specimen in 3View[®]2XP.

Fig. 2 Three-dimensional reconstruction method.



A three-dimensional image is reconstructed by stacking of two-dimensional images.

i.e. low accelerating voltage, large probe current and stabilities. Both of JSM-7100F and JSM-7800F have these features. The details are shown below.

(1) Low accelerating voltage

In SBF-SEM, a bulk specimen embedded in resin is observed. An electron beam at high accelerating voltages creates a smaller electron probe than that at low accelerating voltages. However, it causes charging and decrease of XY-resolution, since incident electrons deeply penetrate into a specimen and signals from the deep region of the specimen are detected. Taking account of these facts, it is better to use low accelerating voltages of 1 to 2 kV.

(2) Large probe current and fast-speed scan

In SBF-SEM, in order to acquire images over a wide region with high resolution, the images have to be acquired at relatively-low magnification with large pixels. In addition, for taking depth profile in the Z-direction, it is needed to acquire several hundreds or several thousands of images. Therefore, it is important to set conditions which enable to acquire a lot of images with high resolution and high signal-to-noise ratio in short measurement time. Taking images at fast scan speed reduces measurement time. But it is not easy to realize both sufficient resolution and high signal-to-noise ratio. To solve this problem, probe current must be increased. In the SBF-SEM, image observation at a scan speed of 1 $\mu\text{sec}/\text{pixel}$ is achieved as well as that at a scan speed of 5 $\mu\text{sec}/\text{pixel}$. In addition, when the probe current is increased with keeping this scan speed, it is possible to obtain higher-quality images with sufficient resolution and high signal-to-noise ratio (Fig. 3).

Using a scan speed of 5 $\mu\text{sec}/\text{pixel}$, we obtained 33 images with pixel size of 4096×4096 in one hour. When using a scan speed of 1 $\mu\text{sec}/\text{pixel}$, we obtained 88 images in one hour. Therefore measurement time becomes twice shorter than that at a slow-scan speed.

Here attention should be paid: appropriate conditions for probe current and scan speed have to be set, since increase of probe current occasionally causes damage to a specimen.

(3) Stability of high voltage, lenses and specimen stage

Occasionally, long measurement time is needed for SBF-SEM. In order to obtain all images with the same quality,

high stability of high voltage, lenses and specimen stage is required. In an experiment using JSM-7800F, we acquired 600 images with high pixels of $16k \times 16k$ using fast-speed scan (0.8 $\mu\text{sec}/\text{pixel}$). Although data acquisition took 40 hours, we could obtain all images with the same quality (Fig. 4).

Specimen preparation

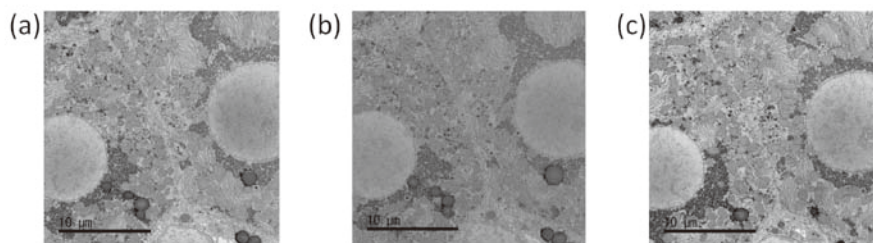
Biological specimens for SBF-SEM need special specimen preparation. It is named NCMIR (National Center for Microscopy and Imaging Research) method [3]. In SBF-SEM, backscattered electrons emitted from a bulk specimen are detected for image observation. However, it is difficult to obtain high contrast image by backscattered electrons using ordinary preparation with glutaraldehyde- OsO_4 , since it is unable to perform post-staining for bulk specimens. Since NCMIR method, in which pre-fixed biological specimens are stained with OsO_4 twice and further stained with uranyl acetate and lead aspartate, is applicable to bulk specimens, this method is effective for high contrast imaging.

Observation procedures

After cutting the specimen embedded in resin to proper size, the specimen is mounted on a specimen pin for 3View[®]2XP using conductive glue (CW2400, ITW Chemtronics). The resin does not have conductivity, but the tissue stained with heavy metals and conductive glue has conductivity. Therefore, if the specimen surface adhered on the pin is exposed, incident electrons pass through the specimen and flow to the pin, and thus charging of the specimen is prevented. After the adhesion, a few thin sections are prepared with an ultra-microtome and an observation area is confirmed with an optical microscope or an electron microscope. Regions around the observation area are trimmed with razors, and the observation area is exposed a glass knife. The final size of the specimen is $1.2 \times 1.2 \text{ mm}^2$ or less. In particular, if thin slice pitch is needed, trimming should be made as small as possible. Finally, metal-coating around the specimen by gold sputtering or silver paste is applied so that incident electrons pass through sides of the specimen and flow to the pin. Therefore charging of the specimen is prevented. (Fig. 5(a)).

After the specimen pin is set to 3View[®]2XP, the specimen is raised up to the cutting position according to following procedures.

Fig. 3 Dependence of image quality on probe current and scan speed.



| | | | |
|---------------|--|--|--|
| Probe current | 50 pA | 50 pA | 250 pA |
| Scan speed | 5 $\mu\text{sec}/\text{pixel}$ (85 sec/image) | 1 $\mu\text{sec}/\text{pixel}$ (18 sec/image) | 1 $\mu\text{sec}/\text{pixel}$ (18 sec/image) |

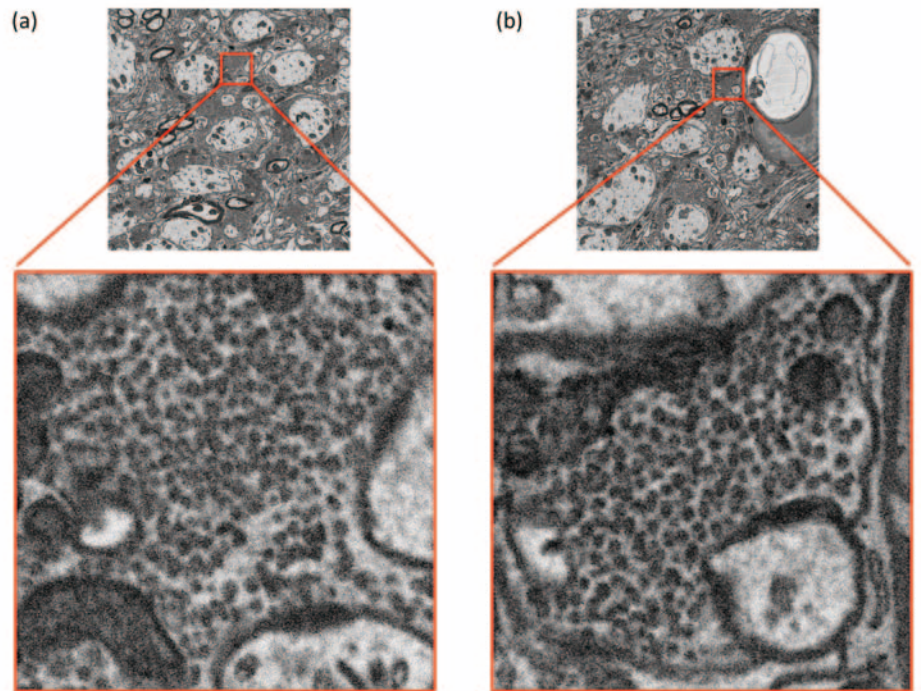
When probe current is constant, faster scan speed leads lower signal-to-noise ratio (see (a) and (b)). When probe current is sufficiently large, the signal-to-noise ratio does not degrade at fast scan speed (see (b) and (c)).

- (1) First, a stereo-microscope is set to the stage (Fig. 5(b)) in order to see magnified image of the specimen surface and the knife.
- (2) The specimen is manually brought close to the knife. Since the knife position is fixed, the specimen is raised up by turning a specimen-height adjustment screw (Fig. 5(c)).
- (3) The specimen automatically approaches the knife. Every

time of knife strokes, the specimen is raised up by 200 nm. During each repeating stroke, the specimen is raised up to the cutting position of the knife, and the specimen is cut and cutting dusts are accumulated on the knife (Fig. 5(d)).

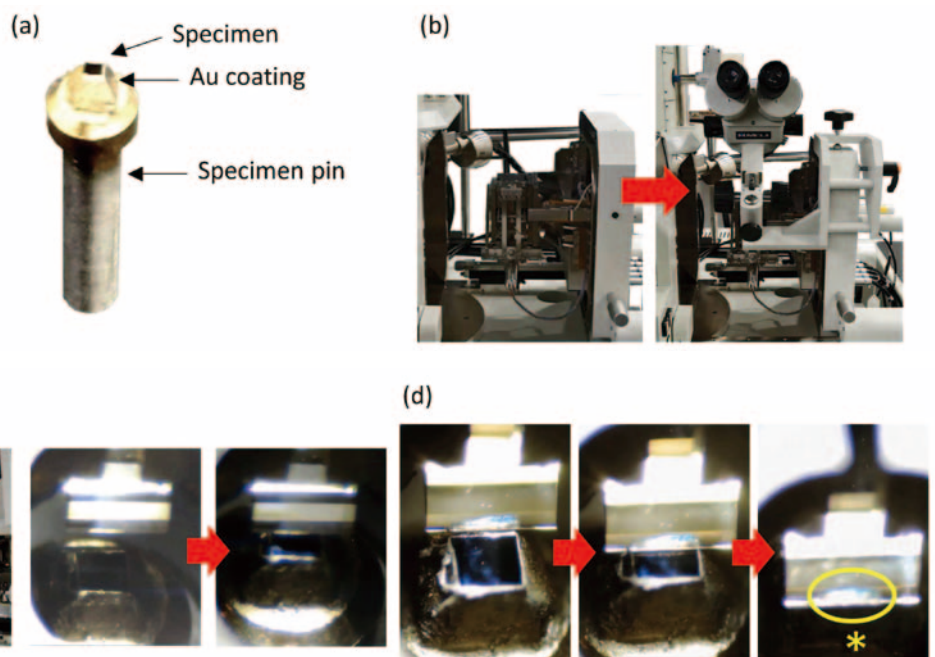
After raising the specimen, the SEM chamber is closed and evacuated. Before observation, observation conditions are set. Accelerating voltage, probe current and scan speed

Fig. 4 Stability of image quality after long measurement time.



Many synaptic vesicles (diameter: approximately 50 nm) are separately identified in SEM images. Image quality is good after long measurement time. (a) SEM image taken at the beginning of observation (b). Six hundredths SEM image taken after 40 hours continuous measurement.

Fig. 5 Setting a specimen to 3View[®]2XP and preparation of cutting.



- (a) A specimen mounted on a specimen pin. Au-coating around the specimen prevents charging.
- (b) A stereo-microscope to see magnified image of a knife and the specimen.
- (c) The specimen is manually raised up to approach close to the knife.
- (d) The specimen is raised up by stroking the knife many times. When the specimen is raised up to the cutting position of the knife, cutting dusts by knife are accumulated on the knife (*).

are set according to the descriptions in the section of “SEM observation”. Field of view is determined by magnification, and XY-resolution (pixel size) is determined by the number of pixels. Cutting thickness corresponds to Z-resolution, and depth in the Z-direction is determined by “cutting thickness” × “the number of images”. A backscattered electron detector is used for observation.

Three-dimensional reconstruction is performed with two-dimensional images according to the following procedures.

- (1) Alignment. There are positional shifts of images in the X and Y-directions. These shifts must be corrected, although these shifts are small. This is called “drift correction”.
- (2) Segmentation. Target objects in each image are painted by the same color (Fig. 6(a)).
- (3) Three-dimensional reconstruction. The segmented objects are reconstructed three-dimensionally by stacking the two-dimensional images (Fig. 6(b)). Slicing in each direction of X, Y and Z shows inside of the objects. In addition, rotation provides a view of the objects from several directions. Such motions of the objects are seen in a movie created by the software system.

Three-dimensional reconstruction of CA3-region of mouse hippocampus

In a brain of vertebrates, information processing such as memory and learning is carried out by transporting information based on communication between nerve cells. TEM images of a vertebrate brain visualize axons with myelin, dendrites extending from nerve cells and synapses connecting nerve cells. It is needed to reveal connections of nerve cells in a brain, in order to understand mechanisms of learning and memory. Connectome analysis has been started, which has the aim to reveal all connections among all nerve cells in a brain. Conventional TEM observes connections of nerve cells, however an observable area is very narrow and thin, and it is difficult to analyze three-dimensional connections of nerve cells.

CA3-region in hippocampus is related to learning and memory. In this study, we analyzed mouse CA3-region by JSM-7800F with 3View®2XP. The specimen was treated by NCMIR method, and two observation areas were imaged under the following conditions.

Field (1): Accelerating voltage: 2.0 kV, Magnification: × 750, Field of view: $78.3 \times 78.3 \mu\text{m}^2$, Number of pixels: 8192×8192 , Pixel size: 9.6 nm, Cutting thickness: 100 nm, Number of images: 400, Alignment: DigitalMicrograph (Gatan), Segmentation: Colorist (SIF), Three-dimensional reconstruction: Visualizer kai (SIF).

Field (2): Accelerating voltage: 2.0 kV, Magnification: ×1200, Field of view: $32.6 \times 32.6 \mu\text{m}^2$, Number of pixels: 16384×16384 , Pixel size: 2.0 nm, Cutting thickness: 50 nm, Number of images: 600, Alignment, Segmentation and three-dimensional reconstruction: Amira (FEI).

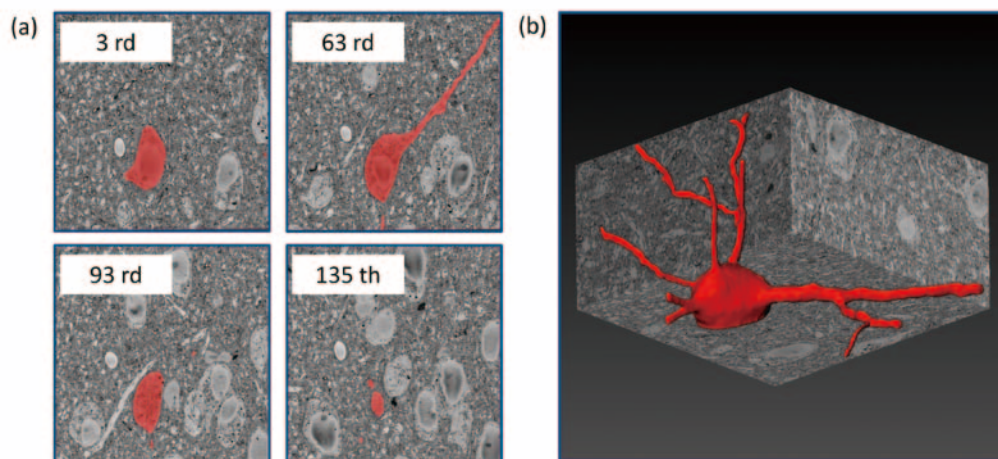
In the Field (1), a three-dimensional image of nerve cells with $74 \times 75 \times 40 \mu\text{m}^3$ was obtained. In this region, we segmented and reconstructed 27 nerve cells and dendrites entering into spaces between the surrounding cells in Fig. 7(a). Three typical cells were visualized (colored by orange, blue and green), each cell body is confined into this region. 8 dendrites, 6 dendrites and 7 dendrites are extended from the orange cell, blue cell and green cell, respectively. In addition, these dendrites are extended to the outside of this region while they branch off.

In the Field (2), a three-dimensional image of synapses with $30 \times 30 \times 30 \mu\text{m}^3$ was obtained. In this region, we segmented and reconstructed some synapses in Fig. 7(b). The image indicates that the red part of mossy fiber terminals (pre-synapses) covers the blue part of spines in CA3 pyramidal cell (post-synapses). In addition, the image shows sites of receptors-accumulated parts for neurotransmitters, post synaptic density (PSD) where indicated with green color.

Summary

SSSEM-based observation with high resolution over a wide region would greatly advance biology as well as materials science. In this article, we described SBF-SEM and actual observation methods. Moreover, we showed three-dimensional structures of nerve cells, dendrites and synapses in CA3-region of mouse hippocampus by SBF-SEM. In order to easily observe a wide region with high throughput, this innovative method requires not only SEM functions (high resolution imaging at low accelerating voltages, short measurement time with large probe current, high stability of image quality for long measurement

Fig. 6 Segmentation and a reconstructed image.



(a) Segmentation of a nerve cell for reconstruction. One nerve cell and dendrites are marked by red color.
 (b) One nerve cell is three-dimensionally reconstructed by stacking segmented images.

time, etc.) but also specimen preparation. In future, we would like to improve not only hardware, but also specimen preparation, reconstruction software and segmentation technique for SBF-SEM.

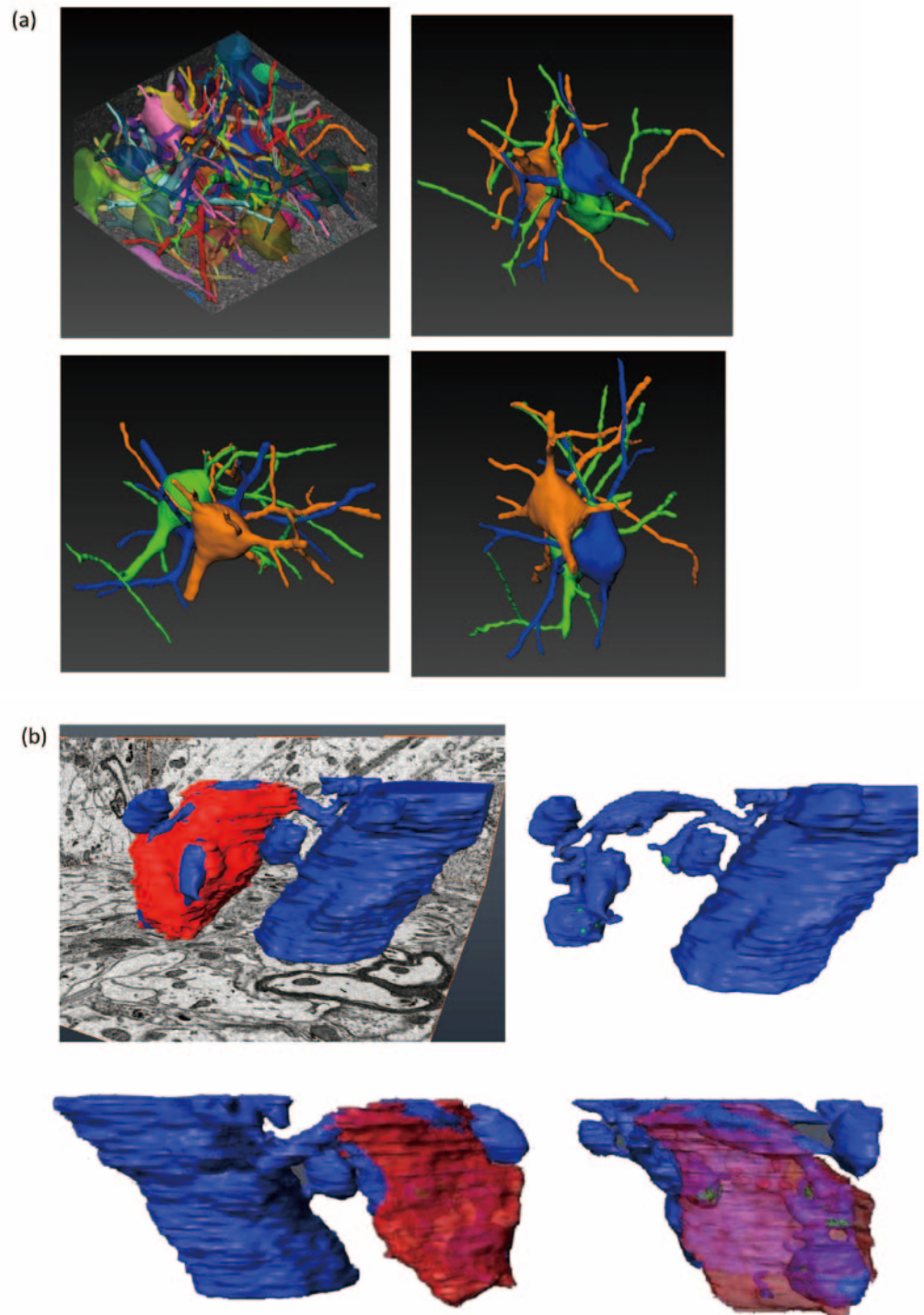
References

[1] Denk, W., and Horstmann, H. Serial block-face scanning electron microscopy to reconstruct three-dimensional tissue nanostructure. *PLoS biology* **2**, e329. (2004).

[2] R. A. Fleck, G. Vizcay, G. Neves, F. W. Grillo, J. Burrone, M. Green, A. Bullen. Serial Block Face Scanning Electron Microscopy Using the JEOL JSM-7100F with Gatan 3View 2XP at King’s College London-UK. *JEOL News*, **50**, 38-45 (2015).

[3] Deerinck, T. J., Bushong, E., Thor, A. & Ellisman, M.H. NCMIR methods for 3D EM: A new protocol for preparation of biological specimens for serial block-face SEM. *Microscopy*, **6-8**. (2010).

Fig. 7 Three-dimensionally reconstructed images of CA3-region in mouse hippocampus.



Depth Profile Measurement with JPS-9030

Masahide Shima

SA Business Unit, JEOL Ltd.

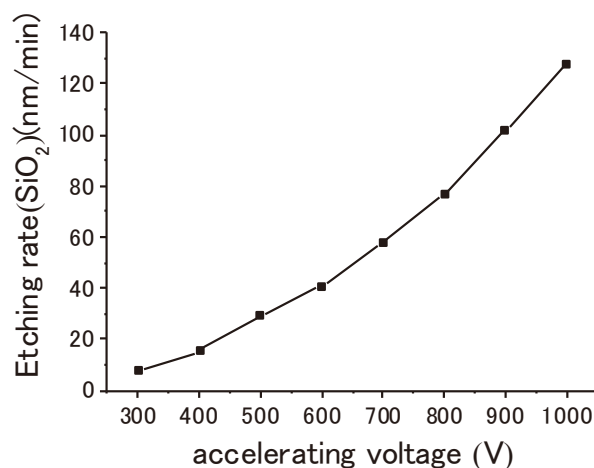
JPS-9030 (Fig. 1) is the X-ray Photoelectron spectrometer designed for high speed depth profile analysis with a Kaufman type ion source mounted on an isolated chamber. This configuration can prevent its electron optics system in an analysis chamber from any sputtered residues causing the sensitivity degradation. The ion source provides a wide etching rate from 6 nm/min to 120 nm/min measured with a SiO₂ layer on a Si wafer (Fig. 2).

JPS-9030 has also two kinds of the top-surface sensitive analysis methods limited to less than a few nm in depth: ARXPS and TRXPS. The spectrometer has multipurpose functions for in-depth and top surface analysis, as well as can provide multipurpose analyses approaching to the high-end XPS with easy operation and long net-running time with little maintenance.

Fig. 1 Appearance of JPS-9030.



Fig. 2 Etching rate of Kaufman type ion source.



Introduction

X-ray Photoelectron Spectroscopy (XPS) is a most widely used method for surface and interface analysis. Depth profile measurement is one of the important functions of XPS. XPS analysis gives us not only elemental information on the film but also quantification and even chemical state information on the

film and its interface. For good performance for depth profile analysis, JPS-9030 employed the Kaufman type ion source and attaches it on an isolated chamber from the measurement chamber. These features make it easy to analyze a very thick sample with high speed and to maintenance of equipment. Recently, GCIB (Gas Cluster Ion Beam) are applied to surface analysis methods like XPS and TOF-SIMS. GCIB prevents

organic samples from damage. ARXPS (Angle Resolved X-ray Photoelectron Spectroscopy) is a non-destructive measurement method compared to depth profile measurement with ion etching. The measurement depth of ARXPS depends on the takeoff angle of electron and the electron analyzer. It is possible to tilt the sample over 80 degrees without decreasing the intensity of photoelectron, because the input lens of JPS-9030 has a long-enough focal length. The features of TRXPS (Total Reflection X-ray Photoelectron Spectroscopy) are surface sensitivity and low background. TRXPS needs special geometry for irradiating X-ray with a very low angle to the specimen. Thus, JPS-9030 is designed for realizing the geometry. These features make it possible to analyze trace elements on the top surface of the specimen. JPS-9030 is a multipurpose XPS system, which needs many kinds of options such as a treatment chamber, a heating system and an ultraviolet light source.

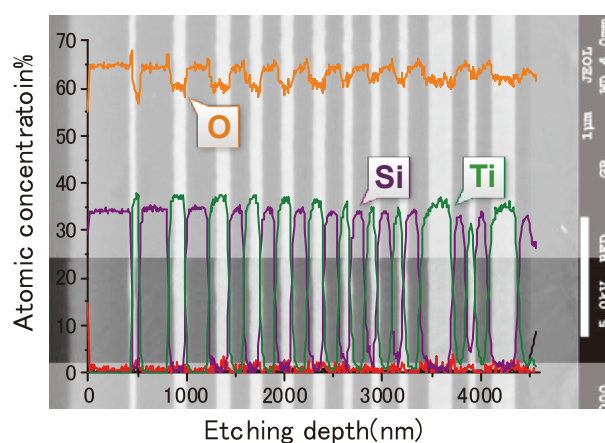
High-speed, high-quality depth analysis with Kaufman type ion source

An optical thin film is generally consisted of a multi-layered structure for antireflection, optical filter or heat insulation. Its performance is strongly influenced by the qualities of each layer: thickness, composition and chemical state. Depth profile analysis of XPS is one of the conventional methods to analyze them in the industrial area. It often takes too long time to measure it with an ion source of low etching rate because its total thickness is over one micrometer. JPS-9030 is a new released XPS instrument designed for multi-purpose depth profile even for such a thicker film because of the Kaufman type ion source.

Depth profile for an optical thin film for antireflection was measured with JPS-9030 using non-monochromatic MgK α , a pass energy of 20 eV under Ar ion accelerating voltage of 1 keV, whose etching rate of 120 nm/min which is estimated with SiO₂ (100 nm)/Si sample. The film has a multi layer structure of twelve cycles of a SiO₂/TiO₂ layer, whose total thickness was about 4 μ m. This optical thin film included a defect which absorbs light passing through the film. **Figure 3** showed a depth

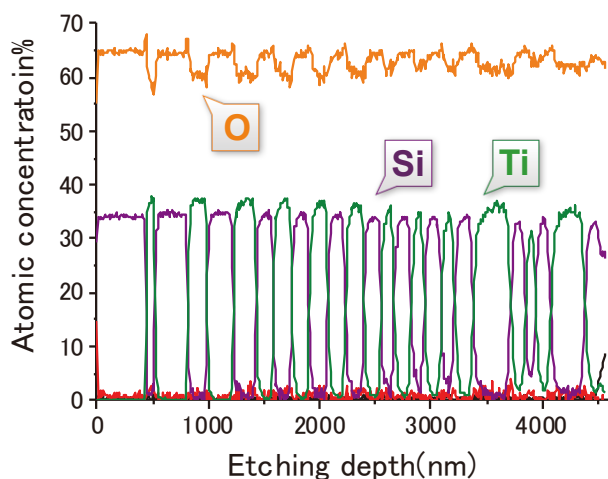
profile result of atomic concentrations: silicon, titanium and oxygen. The data of Fig. 3 also showed that the chemical state of each layers are SiO₂ and TiO₂ and the thickness of each layer were different. It was found from Fig. 3 that this depth profile data had a quite good depth resolution even up to 4 μ m depth from the top surface. In **Fig. 4**, the back scattered electron image (BEI) taken with a SEM and the depth profile measurement result of XPS were overlaid. As a result, these data had a good coincidence with each other (this is because the etching rates of SiO₂ and TiO₂ have similar value). But it is difficult to find the defect in this optical thin film only from these data of atomic concentration and thickness. To find the information on the defect, we focused on the chemical state of silicon. **Figure 5** indicated the Si2p peak at a point inside the film. We

Fig. 4 Overlaid image of depth profile and BEI.



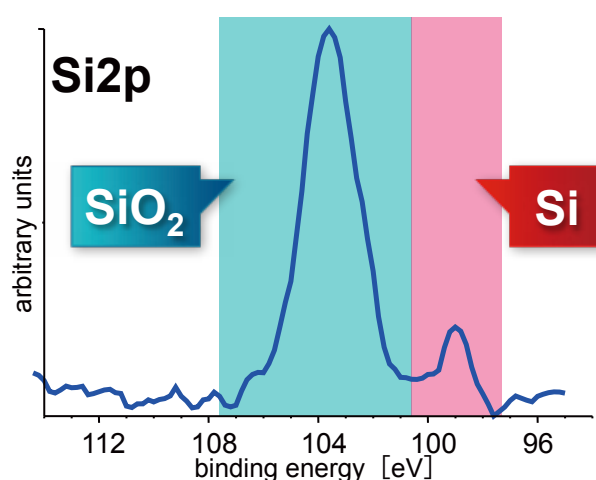
X-ray: Non-monochromatic MgK α / Pass energy : 20 eV
Ion gun accelerating voltage: 1000 V (Etching rate : 120 nm/min as SiO₂)

Fig. 3 XPS depth profile data of optical thin film.



X-ray: Non-monochromatic MgK α / Pass energy: 20 eV
Ion gun accelerating voltage: 1000 V (Etching rate: 120 nm/min as SiO₂)

Fig. 5 Si2p spectrum inside of the film.



found that Si2p peak had 2 peaks at around 99 eV and 104 eV, which indicates that elemental silicon and silicon dioxide exist respectively. **Figure 6** showed that another depth profile data of Si2p was reconstructed with these 2 components. This figure showed that the component of elemental Si was located at the interface between the SiO₂ layer and TiO₂ layer. From these data and analysis result, it was concluded that the defect in the

optical thin film was attributed to the existence of elemental Si located at the interface between the SiO₂ and TiO₂ layer. The XPS system of JPS-9030 with Kaufman type ion source makes it possible to measure depth profile data with good depth resolution and keeping chemical state.

Depth profile analysis with GCIB

Previously, depth profile analysis for organic materials was very difficult because of the sample damage. The cluster ion source causes less damage to organic materials in contrast to monatomic ion. Recently, the cluster ion source (Cluster ion beam system is an option for JPS-9030) can be equipped to the surface analysis instrument such as XPS [1]. **Figure 7** is an example of sample damage caused by monatomic ion using PET (Poly Ethylene Terephthalate) film. These spectra showed that monatomic ion irradiation caused the decreasing of carbonyl and carboxyl functional groups. After the monatomic ion irradiation, the structure of this PET film changed to two layer structure (amorphous carbon/PET). For confirming the effectiveness of GCIB, the sample of amorphous carbon/PET was used. **Figure 8** was the depth profile result of amorphous/PET sample taken with the gas cluster ion source whose condition is that accelerating voltage is 10 kV and cluster size is 1000. This data showed that the gas cluster ion source could remove amorphous layer without damage to the PET substrate. **Figure 9** showed the C1s spectrum of the sample before and after irradiating of gas cluster ion using JPS-9030 in the condition of monochromated AlK α and Pass energy of 10 eV. These data indicated that the GCIB was an effective tool for analyzing organic material with low damage ion etching. JPS-9030 has expandability to attach and control GCIB depth profile measurement with own software.

Fig. 6 Depth profile of Si and SiO₂.

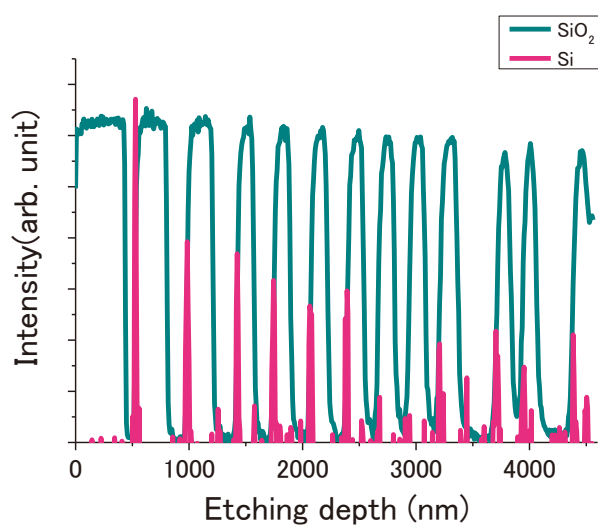
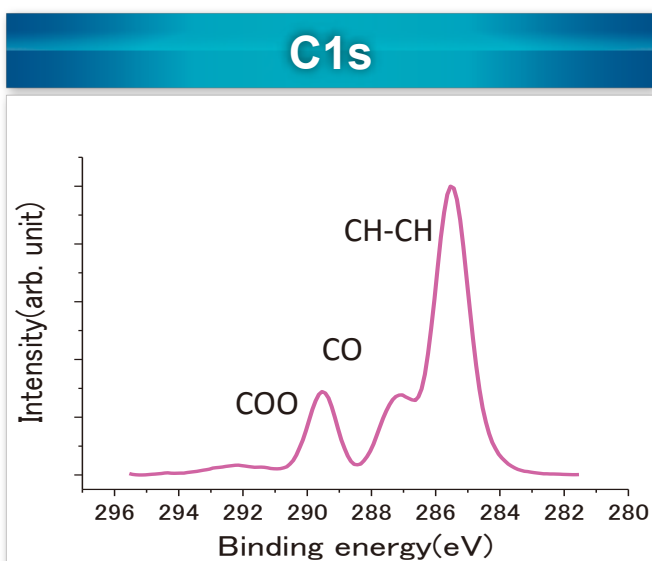
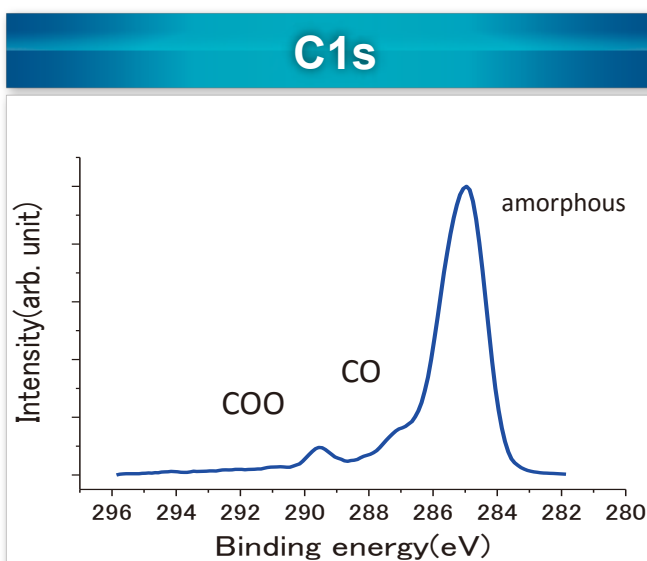


Fig. 7 XPS spectra of PET before and after ion exposure.



Before argon ion exposure



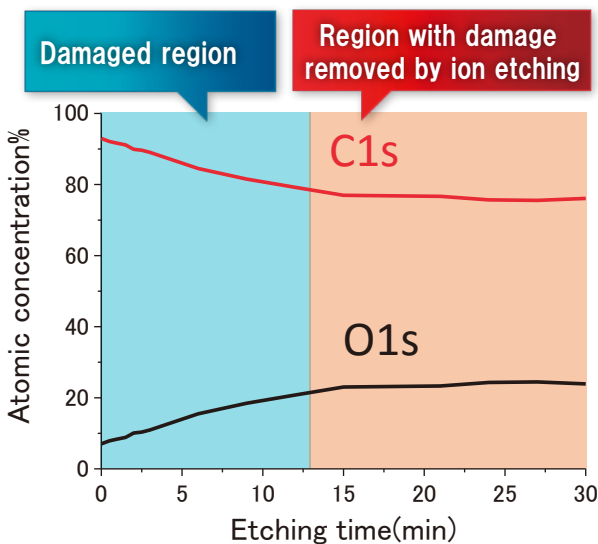
After argon ion exposure

Ultra surface sensitive analysis (Angle Resolved XPS)

ARXPS is a very common and simple analysis method in XPS [2]. As is usually claimed the analysis depth of XPS is about 6 nm, but it is possible to control its analysis depth using the ARXPS method. ARXPS measurement gave us useful information on chemical state of shallow area with non destructive way. For ARXPS measurement, takeoff angle (the angle between sample and analyzer) is an important parameter. Usually the peak intensity of photoelectron decreases at low takeoff angle, but in the case of JPS-9030, the measurement

area increases with tilting the specimen like Fig. 10 because of the long focal depth of an input lens of JPS-9030. As a result, the intensity does not decrease even in high tilting angle of 10 degrees. About 1 nm Si native oxide on Si wafer was measured with ARXPS method at takeoff angle of 90, 30 and 10 degrees as shown in Fig. 11. Two peaks which are elemental Si and oxide Si were observed. For comparing the intensity of elemental Si and silicon dioxide, the peak intensity was normalized at the peak of elemental Si. The peak intensity of silicon dioxide was very small with the takeoff angle of 90 degrees. Whereas in the Si2p spectrum at takeoff angle of 30° (red) and 10° (blue), the peak intensity of silicon dioxide became very high. These spectra show the surface sensitivity of ARXPS measurement with JPS-9030.

Fig. 8 Profile of damaged PET film with G CIB etching.



Ultra surface sensitive analysis (Total Reflection XPS)

TRXPS is also a surface sensitive analysis method [2]. The important parameter of ARXPS is the angle between sample surface and input lens axis. But in the case of TRXPS measurement, the important parameter is the angle between sample surface and irradiated X-ray. When the X-ray is irradiated to the sample at a small glancing angle below 1° (in the case of the characteristic X-ray of AlKα line), the irradiated X-ray is totally reflected at the sample surface. With this condition, XPS spectrum has very low background which generally originated from inelastic scattering electron and very surface sensitivity because electron in the deeper area is not excited. These features make it possible to analyze the trace element on the top surface of the specimen. The configuration of JPS-9030 was designed for realizing TRXPS measurement. Figure 12 was an example of TRXPS measurement. The sample was a hard disk whose surface structure is consisted of lubricant layer (composed of carbon, oxygen, fluorine)/ protective layer (composed of carbon)/ magnetic layer (composed of Co, Pt). The blue spectrum in Fig. 12 was the result of normal XPS measurement, and the red spectrum is the result of TRXPS measurement. The red spectrum was shifted to higher binding

Fig. 9 XPS spectra of PET before and after ion exposure.

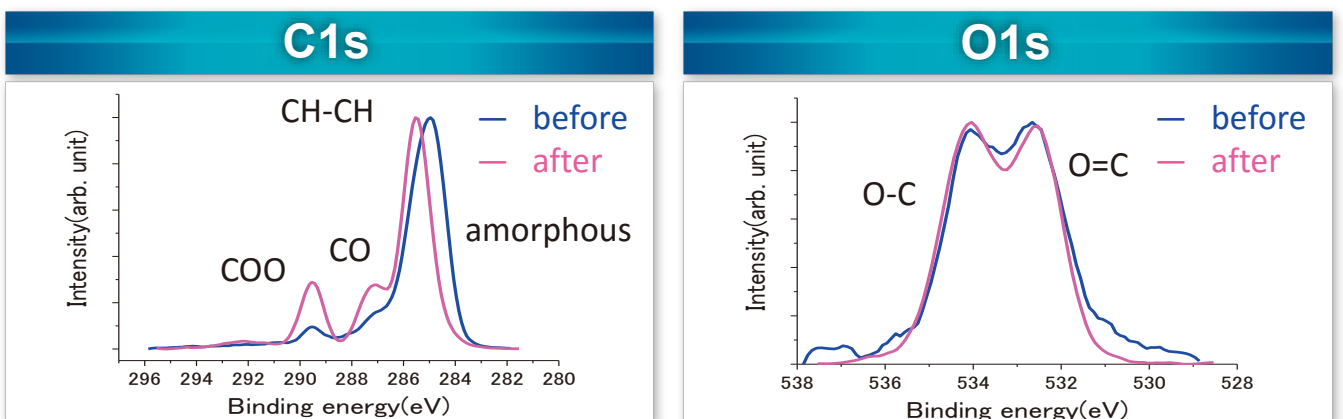


Fig. 10 Schematic diagram of ARXPS with JPS-9030.

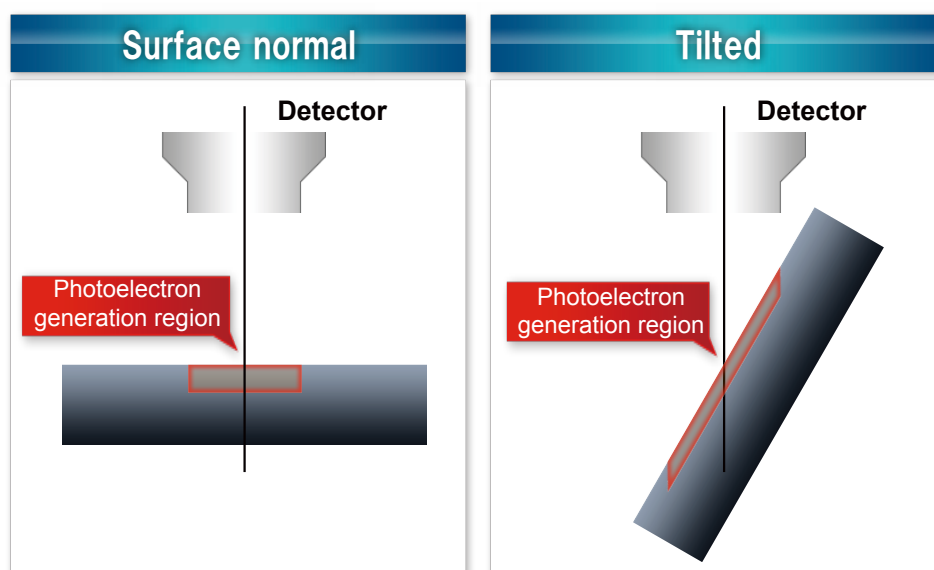
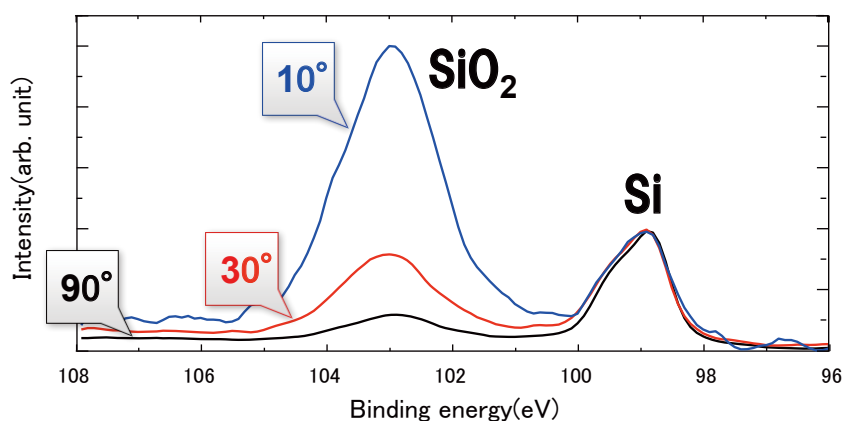


Fig. 11 Results of ARXPS of Si native oxide on Si wafer.



energy side to make these spectra more visible. We could easily find the difference between these spectra; the background of the TRXPS spectrum was lower than that of the normal XPS spectrum. The calculation of the peak to background ratio at F1s peak gave the value of 4.5 for the normal spectrum, and 30 for the TRXPS spectrum. The peaks of Co and Pt were decreased in the TRXPS spectrum. These results indicated that the TRXPS was a surface sensitive method with lower background in the spectrum.

Wealth of Options (Fig. 13)

XPS needs many kinds of options to achieve fruitful data from specimen. JPS-9030 was designed to attach many options such as a specimen treatment chamber, a transfer vessel, an infrared heater and an ultra violet light source. The treatment chamber and the infrared heater are used for gas reaction

and heating in the chamber, and it is possible to transfer the reacted sample from the treatment chamber to the measurement chamber without air exposure. The transfer vessel is used for also transferring the sample from a glove box (or something) to the measurement chamber without air exposure. For example, the transfer vessel is used for analysis of the lithium ion battery sample. The ultraviolet light source is used for analyzing the electronic structure of valence band, work function of the sample with high energy resolution. Such options give fruitful information about specimen.

Conclusion

X-ray Photoelectron Spectroscopy is a common and traditional analysis method. But it is very useful to analyze the qualification, quantification and chemical state of surface and interface of the specimen. JPS-9030 was the specially designed

Fig. 12 Result of TRXPS measurement of hard disk.

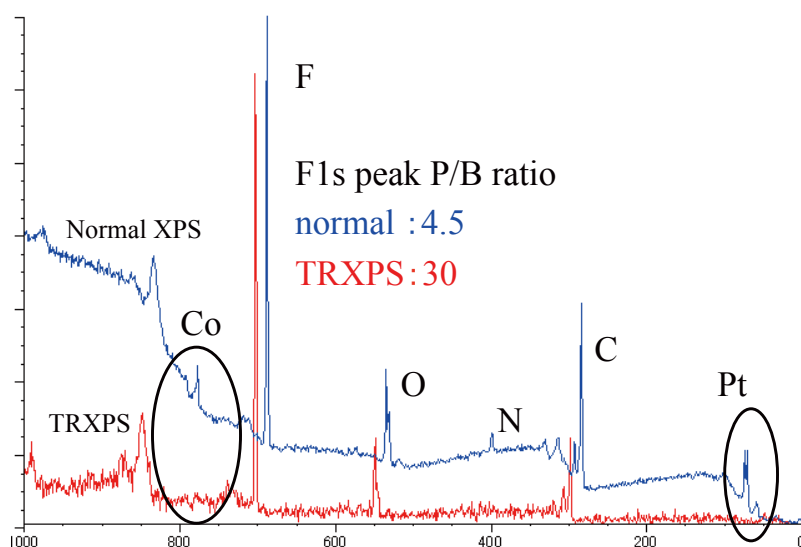
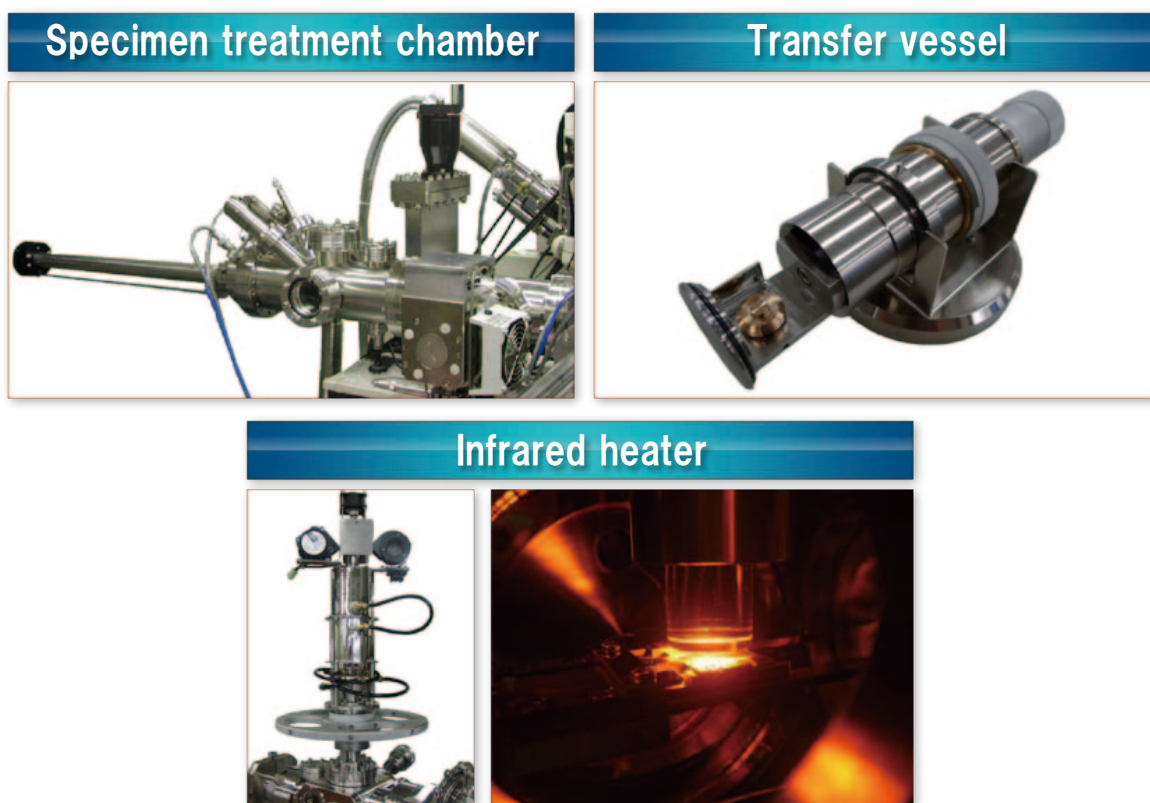


Fig. 13 Options attached to JPS-9030.



for depth profile analysis of the deeper area in inorganic and organic materials, and also for chemical analysis of the very shallow area with ARXPS or TRXPS measurement. You can choose the many options to expand the potential of XPS analysis. We hope all of you get the good data with our JPS-9030.

References

- [1] M. Nakagiri, N. Toyoda and I. Yamada, MRS Proceedings Vol. 1288, 2011.
- [2] D. Briggs, & J.T. Grant, (Eds.) (2003) SURFACE ANALYSIS by Auger and X-ray Photoelectron Spectroscopy. IMpublications and SurfaceSpectra Limited.

Certain products in this brochure are controlled under the "Foreign Exchange and Foreign Trade Law" of Japan in compliance with international security export control, JEOL Ltd. must provide the Japanese Government with "End-user's Statement of Assurance" and "End-use Certificate" in order to obtain the export license needed for export from Japan. If the product to be exported is in this category, the end user will be asked to fill in these certificate forms.

ARGENTINA
COASIN S.A.C.IyF.
Virrey del Píno 4071,
C1430CAM-Buenos Aires
Argentina
Tel. 54-11-4552-3185
Tel. 54-11-4555-3321

AUSTRALIA & NEW ZEALAND
JEOL(AUSTRALASIA) Pty.Ltd.
Suite 1, L2 18 Aquatic Drive
- Frenchs Forest NSW 2086
Australia
Tel. 61-2-9451-3855
Fax. 61-2-9451-3822

AUSTRIA
JEOL (GERMANY) GmbH
Gute Aenger 30
85356 Freising, Germany
Tel. 49-8161-9845-0
Fax. 49-8161-9845-100

BANGLADESH
A.O. CHOWDHURY SCIENCE & SYNERGY PVT. LTD.
87, Suhrawardy Avenue, Floor 2
Baridhara, Dhaka1212
Bangladesh
Tel. 8802-9862272, 8953450, 8953501
Fax. 8802-9854428

BELGIUM
JEOL (EUROPE) B.V.
Planet II, Gebouw B
Louvenssesteenweg 542,
B-1830 Zaveritem
Belgium
Tel. 32-2-720-0560
Fax. 32-2-720-6134

BRAZIL
JEOL Brasil Instrumentos Cientificos Ltda.
Av. Jabaguará, 2958 5º andar conjunto 52 ;
02046-600 Sao Paulo, SP
Brazil
Tel. 55-11-5070 4000
Fax. 55-11-5070 4110

CANADA
JEOL CANADA, INC.
3275 Tera Pk, Local #8
St-Hubert, QC J3Y-8Y6, Canada
Tel. 1-450-676-8776
Fax. 1-450-676-6994

CHILE
ARQUIMED INNOVATION
Arturo Prat 828,
Santiago, Chile
Tel. 56-2-634-6266
Fax. 56-2-634-4633

CHINA
JEOL(BEIJING) CO., LTD.
Zhongkeziyuan Building South Tower 2F,
Zhongguancun Nanshanje Street No. 6,
Haidian District, Beijing, P.R.China
Tel. 86-10-6804-6321
Fax. 86-10-6804-6324

JEOL (BEIJING) CO., LTD., SHANGHAI BRANCH
Room 1505/1506, Nol 300Xl Kang Road,
Jing an Dist., Shanghai, 200040, China
Tel. 86-21-6248-4638/4637/4537/4404
Fax. 86-21-6248-4075

JEOL (BEIJING) CO., LTD., GUANGZHOU BRANCH
M1601, World Trade Center Building,
8371-375, Huan Shi Road East, Guangzhou,
Guangdong Prov., 510095, P.R.China
Tel. 86-20-8778-7848
Fax. 86-20-8778-4268

JEOL (BEIJING) CO., LTD., WUHAN BRANCH
Room A2118, Zhongshang Plaza Office Bldg.,
No. 7 Zhongnan Road, Wuhan,
Hubei, 430071, P.R.China
Tel. 86-27-8713-2567
Fax. 86-27-8713-2567

JEOL LTD. (BEIJING) CO., LTD., CHENGDU BRANCH
1807A Zongfu Building,
NO.35 Zhongfu Road, Chengdu, Sichuan, 610016
P.R. China
Tel. 86-28-86622554
Fax. 86-28-86622564

EGYPT
JEOL SERVICE BUREAU
3rd Fl. Nile Center Bldg., Nawal Street,
Dokki, (Cairo), Egypt
Tel. 20-2-3335-7220
Fax. 20-2-3338-4168

FRANCE
JEOL (EUROPE) SAS
Espace Claude Monet, 1 Allée de Giverny
78230 Croissy-sur-Seine, France
Tel. 33-1-3015-3737
Fax. 33-1-3015-3747

GERMANY
JEOL (GERMANY) GmbH
Gute Aenger 30
85356 Freising, Germany
Tel. 49-8161-9845-0
Fax. 49-8161-9845-100

GREAT BRITAIN & IRELAND
JEOL (U.K.) LTD.
JEOL House, Silver Court, Watchmead,
Welwyn Garden City, Herts AL7 1LT, U.K.
Tel. 44-1707-377117
Fax. 44-1707-373254

GREECE
N. ASTERIDIS S.A.
55-58 S. Tikhoup Str. P.O. Box 26140
GR-10022, Athens, Greece
Tel. 30-1-823-5383
Fax. 30-1-823-9567

HONG KONG
FARMING LTD.
Unit No. 1009, 10/F., Prosperity
603 King's Road, North Point, Hong Kong
Tel. 852-2915-7250
Fax. 852-2581-4635

INDIA
JEOL INDIA Pvt. Ltd.
Elegance Tower, Level 2, 212B
Old Mathura Road, Jasola Business District Centre,
Near Apollo Hospital Jasola,
New Delhi 110 026, India
Tel. 91-11-6472-2578
Fax. 91-11-4060-1235

JEOL India Pvt. Ltd., Mumbai Branch
Regus Mumbai
Levels Ground & 1, Trade Centre Bandra Kuria Complex 1108,
Bandra (E) Mumbai, 400051, India
Tel. : +91-22-40700700

INDONESIA
PT. TEKNO LABINDO Perita Perkasa
Komplek Gading Bukit Indah Blok I/11
Jl. Bukit Gading Raya Kelapa Gading Permai,
Jakarta 14240, Indonesia
Tel. 62-21-45847057/58
Fax. 62-21-45842729

ITALY
JEOL (ITALIA) S.p.A.
Palazzo Paoletti - Milano 3 City,
Via Luribio il Moro, 6/A
20080 Basiglio(MI) Italy
Tel. 39-02-9041431
Fax. 39-02-90414343

KOREA
JEOL KOREA LTD.
Dongwoe Bldg 7F, 1443, Yangjae Daero,
Gangdong-Gu, Seoul, 134-814, Korea
Tel. 82-2-511-5501
Tel. 82-2-511-2635

KUWAIT
Ashraf & CO. Ltd.
P.O.Box 3555 Safat 13036, Kuwait
Tel. 965-1805151
Fax. 965-24335373

MALAYSIA
JEOL(MALAYSIA) SDN.BHD.
508, Block A, Level 5,
Kellana Business Center,
97, Jalan SS 7/2, Kelana Jaya,
47301 Petaling Jaya, Selangor, Malaysia
Tel. 60-3-74927722
Fax. 60-3-74927723

MEXICO
JEOL DE MEXICO S.A. DE C.V.
Arkansas 11 Piso 2
Colonia Napolos
Delegación Benito Juárez, C.P. 03810
Mexico D.F., Mexico
Tel. 52-5-55-211-4511
Tel. 52-5-55-211-0720

Middle East
JEOL GULF FZE
P.O. Box No. 371107
Dubai Airport Free Trade Zone East Wing 5EA No. 404,
Dubai, UAE
Tel. 971-4-609-1497
Fax. 971-4-609-1498

PAKISTAN (Karachi)
ANALYTICAL MEASURING SYSTEM (PVT) LTD.(AMS LTD.)
14-C Main Sehar Commercial Avenue Lane 4,
Khayaban-e-Sehar,
D.H.A.VII, Karachi-75500, Pakistan
Tel. 92-21-35345581/35340747
Fax. 92-21-35345582

PANAMA
PROMED S.A.
Parque Industrial Costa del Este
Urbanización Costa del Este
Apartado 0818-01755, Panama, Panama
Tel. 507-303-3100
Fax. 507-303-3115

PHILIPPINES
PHILAB INDUSTRIES INC.
7487 Bagtikan Street, SAV Makati,
1203 Metro, Manila Philippines
Tel. 63-2-896-8269
Fax. 63-2-897-7732

PORTUGAL
Izasa Portugal Lda.
R. do Proletariado, 1
2790-138 CARNAXIDE, Portugal
Tel. 351-21-424-73-00
Fax. 351-21-418-60-20

RUSSIA
JEOL (RUS) LLC.
Krasnoprolitarskaya Street. 16,
Bld. 2, 127473, Moscow,
Russian Federation
Tel. 7-495-748-7791/7792
Fax. 7-495-748-7793

SAUDI ARABIA
ABDULREHMAN ALGOSAIBI G.T.C. (Riyadh)
Algosabi Building-Old Airport Road
P.O. Box 215, Riyadh 11411, Saudi Arabia
Tel. 966-1-477-7932

SCANDINAVIA
SWEDEN
JEOL (Skandinaviska)AB
Hammarbacken 6A, Box 716, 191 27 Sollentuna
Sweden
Tel. 46-8-28-2800
Fax. 46-8-29-1647

SINGAPORE
JEOL ASIA PTE.LTD.
2 Corporation Road
#01-12 Corporation Place
Singapore 618494
Tel. 65-6565-9989
Fax. 65-6566-7552

SOUTH AFRICA
AD Scientific (Pty) Ltd.
370 Angus Crescent,
Northlands Business Park, 29 Newmarket Road
Northridge, Randburg, Republic of South Africa
Tel. 27-11-462-1953
Fax. 27-11-462-1466

SPAIN
IZASA S.A.
Argoneses, 18, 28100 Alcobendas,
(Polígono Industrial), Madrid, Spain
Tel. 34-91-663-0500
Fax. 34-91-663-0545

SWITZERLAND
JEOL (GERMANY) GmbH
Gute Aenger 30
85356 Freising, Germany
Tel. 49-8165-77346
Fax. 49-8165-77512

TAIWAN
JIE DONG CO., LTD.
7F, 112, Chung Hsiao East Road,
Section 1, Taipei, Taiwan 10023
Republic of China
Tel. 886-2-2395-2978
Fax. 886-2-2322-4665

For NMR & Mass Spectrometer Products
Widestron Technologies Corp.
No.8-2, No.77, Sec.2, Zhonghua E Rd.,
East Dist., Tainan City 701, Taiwan(R.O.C.)
Tel. 886-6-289-1943
Fax. 886-6-289-1743

(For Mass Spectrometer Products)
Tech Mass Technical Co., Ltd.
5F, No.11, Wuqun 2nd Rd., Wugu Dist.,
New Taipei City 248, Taiwan (R.O.C.)
Tel. 886-2-8930-1773
Fax. 886-2-8930-2559

For Semiconductor Products:
JEOL TAIWAN SEMICONDUCTORS LTD.
11F-1, No. 346, PeiDa Road, Hsin-Chu City 300,
Taiwan, Republic of China
Tel. 886-3-523-8490
Fax. 886-3-523-6503

THAILAND
BEOTHAI BANGKOK EQUIPMENT & CHEMICAL CO., Ltd.
300 Phrayothin Rd. Phrayathai, Bangkok 10400,
Thailand
Tel. 66-2-615-2929
Fax. 66-2-615-2350/2351

JEOL ASEAN TECHNICAL CENTER (JATC)
MTEC building room 533
114 Moo9, Thailand Science Park
Pachayothin Rd., Klong 1, Klong Luang,
Pathumthani 12120
THAILAND
Tel. 66-2-564-7738
Fax. 66-2-564-7739

THE NETHERLANDS
JEOL (EUROPE) B.V.
Lirweg 4, NL-2153 PH Nieuw-Vennep,
The Netherlands
Tel. 31-252-623500
Fax. 31-252-623501

TURKEY
Tekser A.S.
Kartal Cad. No: 55/3 Inonu Wah.,
Atasehr 34755, Istanbul, Turkey
Tel. 90-216-5736470
Fax. 90-216-5736475

USA
JEOL USA, INC.
111 Osborn Road, Peabody, MA 01960, U.S.A.
Tel. 1-978-535-5900
Fax. 1-978-536-2205/2206

JEOL USA, INC. WEST OFFICE
5653 Stoneridge Drive Suite #110
Pleasanton, CA 94588, U.S.A.
Tel. 1-925-737-1740
Fax. 1-925-737-1749

VENEZUELA
GOMSA Service and Supply C.A.
Urbanización Montalban III
- Residencias Don Andres - Piso 7 - Apartamento 74
Avenida 3, entre calles 7 y 6
Montalban, Caracas, Venezuela
Tel. 58-212-443-4342
Fax. 58-212-443-4342

Vietnam
TECHNICAL MATERIALS AND RESOURCES
IMPORT-EXPORT JOINT STOCK COMPANY(REXCO)
Hanoi Branch
No.13 Lot.12 Trung Yen, Trung Hoa Street,
Cau Gay Dist, Hanoi, Vietnam
Tel. 84-43-562-0516
Fax. 84-43-853-2518